Fabrication of Arrays of Plasmonic nanostructures for Biosensor Applications

By

Sami Alalawi

Department of Chemistry

University of Sheffield

A Thesis Submitted to the University of Sheffield for the Degree of
Doctor of Philosophy

February 2023

Acknowledgment

I would like to acknowledge Prof. Graham J Leggett for his supervision, great help and critical review of several perspectives of this research and advice throughout the time it took me to complete my research. I am also very grateful to have met wonderful people who were always with me during the study years in Sheffield and available to assist me. Also, I strongly express my earnest appreciation to Dr. Anna Lishchuk for her guidance and suggestions throughout the course of study and reading of my thesis. I would like to thank the University of Sheffield and everybody in chemistry department. I would like to thank GJL group members past and present especially Dr. Brice Darroch, Dr. Max Chambers, Dr. Martin Munz, Mr Charlie Smith, and Dr. Debbie Hammond for their assistance during the early part of my PhD research. It would be impossible to proceed any further without the mention of some individuals whom I met through serendipitous circumstances and who made my years as a postgraduate student unforgettable; they are Mr Ibrahim Alatawi, Mr Nasiru Usman, Mr Abdullah Sari, Miss Evelin Csanyi, Mrs Jabreh Alkorbi, Miss Bayan Samman, Dr, Benjamin Bower, Mrs Munirah Alfarhan, Mrs Sharifah Alharthi, Dr Bakaet Alqurashy, and my closer friends. Without their love, support and prayers this work would not be accomplished. I offer my deepest gratitude to my wife, and my sons (Ahmed and Khaled). This gratitude also extends to my brothers and sisters for their unlimited support during my PhD. Special thanks also goes to Taibah University for its financial support throughout the period of my PhD study.

Finally, I dedicate my thesis to my family and especially to my parents for being inspiring and patient and motivating me to write and supporting me.

Contents of Table

List of Figures

List of Table

Abbreviations

pKa	Acid dissociation constant
Ψ	Amplitude
Ab	Antibody
Ag	Antigen
APTES	3-Aminopropyltriethoxysilane
ATRP	Atom transfer radial polymerization
AFM	Atomic force microscope
EW	An evanescent wave
BE	Binding energy
Bipy	2, 2'Bipyridine
θ	Angle
BSA	Bovine serum albumin
BEC	Bose-Einstein condensation
BIBB	2-Bromoisobutyryl bromide
BIBB-APTES	2-Bromo-2-methyl-N-(3-triethoxysilyl-propyl)-propionamide
Cd	Cadmium
Cr	Chromium
CFU	Colony-forming unit
CA	Contact angle
CRP	Controlled/living radical polymerization
DCM	Dichloromethane
DMF	Dimethyl formamide
DMSO	Dimethyl sulfoxide
DMPP	Dimethylphenylphosphine
$\omega(k)$	Dispersion relation
ε_m	Dielectric function
DMT	Dragon-Muller-Toporov
EM	Electromagnetic
EBL	Electron beam lithography
EPR	Electron paramagnetic resonance
eV	Electronvolt
ε_0	Electric permittivity
e	Elementary charge
EW	Evanescent wave
EUV	Extreme ultraviolet
FTIR	Fourier transform infrared spectroscopy
FF	Frictional force
FFM	Friction force microscopy
FWHM	Full width at half maximum
GPC	Gel Permeation Chromatography
Au	Gold
AuNP	Gold nanoparticles
He	Helium

HPLC	High performance liquid chromatography
Ig	Immunoglobins
IgG	Immunoglobulin G
IL	Interferometric lithography
IPA	Isopropyl alcohol
pI	Isoelectric point
KE	Kinetic energies
LOD	limit of detection
LSPR	Localized Surface Plasmon Resonance
ROP	Living ring-opening polymerization
m	Mass
MA	Methacrylate
MEA	Mercaptoethylamine
μCP	Micro-contact printing
M	Molar
MIPs	Molecularly imprinted polymer nanoparticles
MCCs	Monolayer of colloidal crystals
ng	Nanogram
nm	Nanometer
nM	Nano Molar
NSL	Nanosphere lithography
NIR	Near-infrared
NMP	Nitroxide-mediated polymerization
FN	Normal force
NMR	Nuclear magnetic resonance
ODT	1-Octadecanethiol
$\varepsilon(\omega)$	Permittivity is often treated as a complex function of the (angular) frequency ω
Δ	Phase
PBS	Phosphate buffered saline
ω_p	Plasma frequency of the conduction electrons of a metal
pM	Picomolar
PAA	Poly (acrylic acid)
PCBMA	Poly (carboxybetaine methacrylate)
PCysMA	Poly (cysteine methacrylate)
PE	Polyelectrolyte
PEG	Polyethylene glycol
(PEG silanes)	Poly (ethylene glycol)-terminated silanes
PMMA	Polymethyl methacrylate
PMPC	Poly (2-methacryloyloxyethyl phosphorylcholine)
(PDMA)	Poly(2-(dimethylamino)ethyl methacrylate)
PDEAEMA	Poly (N, N (diethylamino)ethyl methacrylate
PNIPAAM	Poly(N-isopropylacrylamide)
PSerMA	Poly (serine methacrylate)

PS	Polystyrene
PSBMA	Poly (sulfobetaine methacrylate)
$\varepsilon(\omega)$	Predominantly
Rg	Radius of gyration of a polymer
RIU	Refractive index unit
RAFT	Reversible addition-fragmentation chain transfer
RMS	Root Mean Square
RMSE	Root mean square error
SEM	Scanning electron microscope
SAMs	Self-assembled monolayers
SET-LRP	Single electron transfer living radical polymerization
SiNW-based FETs	Silicon nanowire field-effect transistors
SE	Spectroscopic ellipsometry
SEF	Surface-enhanced fluorescence
SERS	Surface-enhanced Raman scattering
SI-ATRP	Surface-initiated atom transfer radical polymerization
SI-PIMP	Surface-initiated photoiniferter-mediated polymerization
SPs	Surface Plasmons
SPP	Surface Plasmon Propagation
SPR	Surface Plasmon Resonance
(tpy)	Terpyridine
3D	Three dimensions
M_t^n	Transition metal
TM	Transverse-magnetic
DETA	Tridentate diethylenetriamine
2D	Two dimensions
UCST	Upper critical solution temperature
UHV	Ultra-high vacuum
UV	Ultraviolet
λ	Wavelength
k	Wave vector
H	Wet thickness of surface-anchored polymer
XPS	X-ray photoelectron spectroscopy

Abstract

Using interferometric lithography (IL) in a double exposure process a library of different arrays of gold nanostructures was formed. Self-assembled monolayer resists were patterned by exposure to an interferogram formed using a Lloyd's mirror interferometer, in which a sample and a mirror are placed at an angle θ relative to each other, and etched using mercaptoethylamine in ethanol. Patterning using a single exposure yielded gold nanowires with pitches in the range 110 nm – 270 nm and lengths of up to 1 cm. The pitch of these lines was controlled by changing the angle between the sample and the mirror in the interferometer. Using a double exposure process in which the sample is rotated between exposures, it was possible to fabricate arrays with a variety of different geometries. After annealing, extinction spectra were significantly changed and exhibited strong plasmon bands. It was found that the energy of the localized surface plasmon resonance (LSPR) was controlled by changing the pitch in the interferometer, the etch time, and the geometry of the arrays. The LSPR peak was typically in the range 500 nm to 750 nm. The extinction spectra of samples fabricated using small values of θ yielded strong plasmon bands, the gold nanostructure arrays functioned as label-free LSPR sensors. After the immobilisation of streptavidin and IgG on the gold nanostructure arrays, a red shift was observed in the position of the LSPR. The adsorption kinetics of streptavidin on biotinylated gold surfaces were characterised by spectroscopic ellipsometry, and the measured shifts in the position of the plasmon band following binding of streptavidin to biotinylated gold nanostructure arrays was found to be closely correlated with the adsorption kinetic data obtained using spectroscopic ellipsometry. After attachment of synthetic maquette light-harvesting proteins to gold nanostructures, the surface plasmon resonances were found to split. This splitting in the spectra was attributed to strong coupling between the localised

surface plasmon resonances and excitons in the proteins. Gold nanostructure arrays can be reused many times following cleaning in cold piranha solution, thus facilitating the convenient acquisition of repeat measurements under identical conditions.

Cysteine methacrylate (CysMA) was synthesised via the thia-Michael addition of cysteine to a commercially available acrylate precursor. Poly cysteine methacrylate (PCysMA) brushes were grown from gold nanostructure arrays that had been functionalised by adsorption of a brominated thiol using atom transfer radical polymerisation with the bromine acting as an initiator. The thickness of the brush layer was controlled by controlling the polymerisation time, while the kinetics of brush growth were measured using spectroscopic ellipsometry and AFM. PCysMA brushes exhibited pH-responsive behaviour: at neutral pH, the polymer is zwitterionic, while at pH <2 and >12, the polymer acquired a net charge, leading to increased repulsion between surface-grafted chains and an increase in swelling away from the substrate. Using both spectroscopic ellipsometry and UV-vis spectroscopy, shifts in the plasmon band were observed as a function of the swelling state of the polymer. AFM was used to measure the growth of PCysMA from gold nanostructure arrays. It was found that the increased free volume impacts brush morphology by boosting the brush thickness.

1. Introduction

1.1 Plasmonics

Plasmonics is a rapidly growing field of nanoscience that focuses on investigating the phenomena caused by the extraordinary, nanoscale optical responses in metals.[1] At a metal surface, the conduction electrons oscillate about mean positions at a characteristic frequency known as the plasma frequency.[2] Resonant coupling of these mechanical displacements to electromagnetic radiation leads to the formation of surface plasmon polaritons, quasi-particles in which the properties of light and matter are mixed.[3] These are able to propagate on the surface for tens to hundreds of micrometers, after which they typically fade away due to the absorption that takes place in the metal and the scattering that occurs via the dielectric medium. The surface electrons associated with metal nanostructures can also couple to electromagnetic radiation, leading to the formation of confined optical modes, known as localised surface plasmon resonance (LSPR).[4]

The field of plasmonics has therefore developed at the interface of photonics, electronics, and nanotechnology to become a promising field of science and technology.[4,5] The popularity of plasmonic nanostructures has increased significantly in recent years as such materials produce extreme from of light concentration and manipulation, making them extremely beneficial for optical physics and devices.[6,7]

The dielectric constant of the material and the medium used, as well as the geometrical size of the nanostructures concerned, determine the relevant plasmon resonance frequency.[8,9] Plasmonic structures, thus displaying sensitivity to the optical constants of the selected medium.[10,11] In surface plasmon resonance, the sensitivity of surface plasmon polaritons to changes in the refractive index at the surface is used to measure the binding of analytes at the surface of plasmonic.[12,13] Polaritons are hybrid particles made up of a photon strongly coupled to an electric dipole. SPR biosensors are capable of detecting even minute changes in the refractive index when biomolecules interact with immobilized receptors on the surface of the optical transducer while the optical transducer converts light into electrical charge.[14] Plasmonic nanoparticle applications have gained widespread attention over in the last couple of years[15] due to their substantial absorption and broad scattering cross-sections, which lead to very large extinctions, making these particles are well suited for use as reporters in a variety of types of sensor. For instance, lateral flow immunoassays (LFIA) can be used with any protein, hapten, nucleic acid, or amplicon to detect both small and big molecules.[16] Rapid qualitative tests can also be performed using a visual marker, such as gold, carbon, or coloured latex nanoparticles, and such tests can then be improved by employing a reader to transform data into a fully quantitative readout.[15,17,18]

1.2 Applications of plasmonics

Plasmonics as a category first emerged in the 1950s when surface plasmon polaritons were initially discovered.[19,20] Nanoplasmonic materials have since attracted interest across a wide range of applications, in fields including ranging across chemistry, physics, medicine, biology, and engineering.

The properties of plasmonic structures can be controlled by regulating their structural features such as nanoparticle size and crystal morphology.[21] Their production of a range of spectral responses to biological, mechanical, and chemical control stimuli then allow them to be employed to create a variety of plasmonic sensors. Plasmonic biosensing techniques use metal nanostructures, such as Au, with biomolecules attached to the surfaces of the plasmonic nanostructures directly or through other linkers, as shown in the schematic diagram in Figure 1.1. Electrons on a bare Au nanostructure surface resonate at a certain at λ_{LSPR} prior to binding,[22] with the value of λ_{LSPR}

changes depending on the nanostructures' shape, size, composition, and surrounding environment. When biomolecules bind to nanostructures, the local refractive index changes, leading to a change in the energy of the plasmon band in the optical spectrum as shown in Figure 1.1. The high extinction coefficients of metal nanoparticles mean that these shifts in the plasmon band are measurable; they can therefore be used as the basis for the design of sensors.

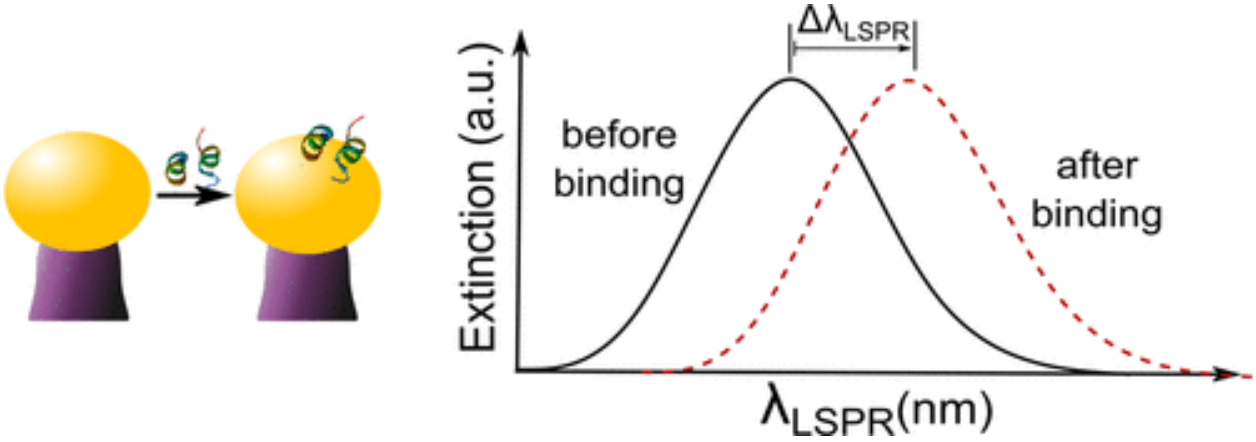

Figure 1.1. Schematic of (a) Au nanostructures before and after biomolecules are binding and (b) spectrum before and after biomolecules binding.[22]

1.2.1 Solar cells

Plasmonic particles have large extinction coefficients, and plasmonic nanoparticles can scatter light back into photovoltaic structures.[23] Researchers have therefore made significant attempts to exploit these properties in order to improve the efficiency of solar cells by enabling them to absorb more light, and the numerous resulting semiconductors and solar cell designs have indeed shown improvements in photocurrent generation. Through the use of plasmonic devices, light can be captured, and its energy transferred to incredibly thin semiconductor layers, creating free charge carriers that can stimulate a flow of current. When a plasmon resonance is activated, energy is transferred via the robust electromagnetic field that surrounds a nanoparticle. The plasmon energy can then be transmitted to surrounding semiconductor material through this near-field and excited charge carriers there.[24]

1.2.2 Biomedical applications

In addition to being photostable and thus applicable to bio-nanoprobes, plasmonic nanoparticles can also scatter light strongly.[25] This means that they are easy to identify using dark-field illumination and similar sensing methods, making them effective for use in various in-vitro biological settings as shown in Figure 1.2.

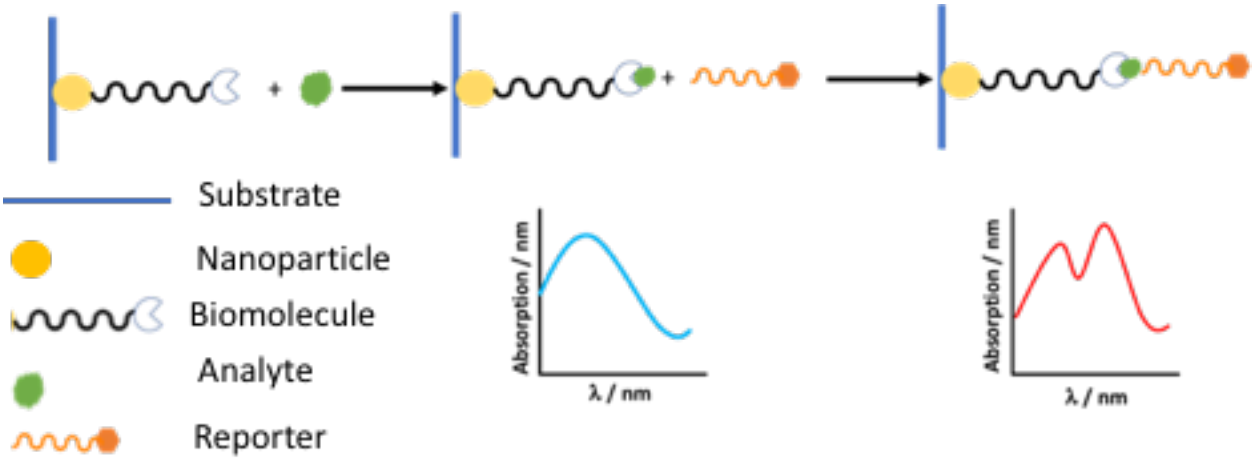

Figure 1.2 Schematic diagram of a nanoparticle functionalised with a probe biomolecule.

Nanoparticles can also be used to examine interactions between other nanoparticles and cells. In order to identify biomolecules and proteins that can be used to treat specific diseases, gold and silver nanoparticles are thus used as plasmonic biosensors.[26] For example, a nanoparticle is functionalised with a probe biomolecule, such as an antibody or oligonucleotide, the binds the analyte can be used as an antigen. In a second step, a reporter (a polyclonal antibody or oligonucleotide) is functionalised with a fluorophore (exciton) and is bound to the analyte.

The unique optical, electrical, and thermal properties of gold and silver nanoparticles make them ideal for use in molecular diagnostics and antimicrobial coatings.[27]

Metallic nanoparticles and nanoshells are more commonly employed in optical biosensing.[28] Each localised surface plasmon has a resonance frequency that is highly sensitive to the dielectric constant of its surrounding medium. Thus, any changes to the dielectric constant of this medium create movement in the surface plasmon resonance frequency, even if only a single molecule attaches to the metallic nanoparticle. Modern-day optical methods can then be employed to measure this resonance frequency. As an example of biomedical applications, plasmonic nanoparticles are now used in microscopy and cancer treatment.

1.2.2.1 Microscopy

Plasmonic nanoparticles are commonly employed in electron microscopy (such as, transmitter electron microscopes, scanning electron microscopes, and fluorescent microscopes) to label functional components of cells and other biological structures. In recent studies, attempts have been made to use 40 nm gold nanoparticles to specifically bind to epidermal growth factor receptors (EGFRs), in order to determine the density of those receptors on a cell,[29] as the shift in resonance frequency of the plasmonic nanoparticles can be used to provide quantitative data about EGFR density.[30]

1.2.2.2 Cancer treatment

Gold nanorods that have been functionalised with epidermal growth factor can be employed in some targeted radiation treatments.[31,32]

Overall, there is a wealth of applications illustrating that the optical properties of plasmonic systems that make them ideal for use in a wide range of areas, including biosensors,[1,2,3,4,5] and optical devices,[6,7,8,9] and photovoltaic devices.[10,11,12]

1.3 Motivation for this PhD

The development of fast, effective, cost-effective methods for the fabrication of arrays of nanostructures with well-defined properties is desirable due to the importance of chip-based diagnostics to multiple medical and other applications. All such applications further necessitate the formation of arrays of metal nanoparticles supported on solid substrates.

Electron beam lithography is the most precise method for the fabrication of nanostructures on solid supports; however, it is slow and depends on the availability of expensive infrastructure and highly trained personnel.[33] Thus, electron beam lithography has not become established as a manufacturing tool. A number of low-cost routes to the fabrication of gold nanostructure arrays exist, such as colloidal lithography that are fast and cheap. However, while these are able to produce certain types of nanostructures effectively, they lack flexibility and they do not offer significant control over nanoparticle array morphology. For example, in colloidal lithography, gold is evaporated through the interstitial spaces in self-assembled arrays of colloidal particles, yet the dimensions and geometry of the resulting array are limited by the availability of polymer colloids and the natural packing arrangements (e.g. hexagonal) in self-assembled films.[34]

The goal of this PhD research is thus to explore a different approach to the fabrication of solid-supported metal nanostructures, based on interferometric lithography, that combines very high resolution with a broad range of programmability. The range of accessible morphologies and the resolution and plasmonic properties of these structures is thus investigated. An important subsidiary goal of this project is being to explore these sensitivities of nanoarrays to biomolecules, how they can bind molecules to develop strong coupling modes, and their analytical utility, with the ultimate goal begin to make a simple chip-based assay that can be used with easy to find equipment.

1.4 Hypothesis

The aim of this thesis is to determine whether it is possible to fabricate Au nanostructures with a wide range of sizes, pitches and geometries using IL, as inexpensive and rapid creation method, while also providing a high level of control and achieving high resolution. IL, as well as being rapid, is capable of being used to fabricate arrays over large areas. It ca also produce a range of nanostructures with well controlled properties such as size and shape. The array morphology, and hence the resulting plasmonic properties, of such nanostructures is thus, in principle, programmable. The main goal of this work is thus to discover how to control the array morphology to enable control of the plasmon energy from the visible to the IR region, and to test the properties of these arrays and their potential application in biological sensing.

1.5 Outline of the research programme

The main aims of the project are:

(i) to develop and validate a nanofabrication process based on IL.

(ii) to test the analytical performance of nanostructures formed by IL.

(iii) to determine whether plasmonic nanoarrays can be used to monitor the pH-dependent swelling of polymer brushes.

1. Gold films were deposited onto Cr-primed substrates. Nanostructure arrays were then formed using IL, with the parameters that control the lithographic process (AFM, XPS, SE, and contact angle) varied systematically. The effect on nanoparticle morphology was then characterised by using AFM, and the effect on the spectroscopic properties of the films measured by using AFM.
2. To test the analytical utility of the nanostructure arrays, a variety of approaches were used, including the measurement of extinction spectra in a variety of media to determine the refractive index sensitivity of the arrays, and the attachment of streptavidin, a protein widely used in bioassays. The possibility of achieving strong plasmon-exciton coupling was be studied using light harvesting complex 2 from the purple bacterium Rhodobacter sphaeroides.
3. Films of a pH-sensitive polymer, poly (cysteine methacrylate) were grown from gold nanostructure arrays by atom transfer radical polymerisation, and the resulting polymer functionalised nanostructures characterised by using AFM and UV-vis spectroscopy. PCysMA is known to undergo pH-dependent conformational changes, swelling substantially in basic and alkaline conditions. The pH of the medium was thus varied, to determine whether arrays of polymer-functionalised nanostructures might be useful in pH sensing applications.

2. Literature review

2.1 Plasmons

A plasmon is a quantum of plasma oscillation. Just as light consists of photons, or mechanical vibrations consist of phonons, a plasma oscillation consists of plasmons, the collective oscillations of the free electron gas.[35] The application of an external electric field to fixed ions in a metal causes the movement of electrons with negative charge relative to the cores with positive charge. Based on this dislocation, the electrons experience fluctuation at the plasma frequency when the electric field is removed, and this fluctuation is quantised by the plasmon. Surface plasmons (SPs) then occur at the interfaces between materials for where the real part of its relative permittivity is positive (e.g. air, glass, other dielectrics), and those where the real part of the permittivity is negative at the given frequency of light (typically a metal or heavily doped semiconductor) at a given frequency of light. At visible wavelengths, interfaces that support surface plasmons are often formed by metals like silver or gold when these are in contact with dielectrics such as air or silicon dioxide. Surface plasmons are not only formed on flat surfaces; they can occur on the surfaces of other structures, including particles, rectangular strips, grooves, and cylinders.[36,37] Resonant coupling of light to plasmon modes occurs where the incident radiation has a frequency matching that of the plasmon oscillation. As the energies of the plasmon modes correspond to the visible region of the electromagnetic spectrum, metal nanoparticles often display pronounced coloration under such circumstances. When the plasmon mode is restricted to a nanoparticle surface, it is called a localised plasmon surface resonance (LSPR). Plasmonics is the name given to the investigation of such interactions between light and matter, which has become the basis of numerous optical applications.[38,39]

2.2 Fundamentals of Plasmonics

The interactions between metals and electromagnetic fields are classically described using Maxwell's equations.[40,35] However, a plasmon is simply a quantum of plasma oscillation, and its quantum character cannot be neglected, despite the fact that the classical description often suffices. Various essential optical properties of the metal can thus be understood by applying plasma theory, in which the free electrons of a metal are considered to behave as an electron liquid, with a bulk number density *n* moving against a fixed background of positive ion cores. The "volume plasmons" oscillate in response to any external electromagnetic field in a motion is damped by the collisions of electrons, which occur with a characteristic frequency γ. According to the Drude model,[8] the frequency dependent permittivity of metal thus:

$$\boldsymbol{\varepsilon(\omega) = 1 - \frac{\omega_p^2}{\omega^2 + iY\omega}} \qquad \mathbf{2.1}$$

where $\omega_p = \sqrt{\frac{ne^2}{\varepsilon_o m}}$ is the plasma frequency of the free electron, with elementary charge *e* and mass *m*, and ε_0 is the electric permittivity of vacuum. All the basic of optical phenomena can be framed by the understanding that $\varepsilon(\omega)$ is the frequency dependent permittivity. This dielectric function $\varepsilon(\omega)$, known as the Drude model,[41] thus describes the dispersive properties of metal. For large frequencies close to ω_p, $\varepsilon(\omega)$

$$\boldsymbol{\varepsilon(\omega) \approx 1 - \frac{\omega_p^2}{\omega^2}} \qquad \mathbf{2.2}$$

which gives the dielectric function of the undamped free electron.

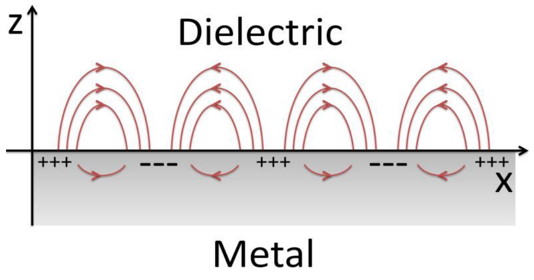

Figure 2.1 The Schematic representation of an electron density wave propagating along a metal-dielectric interface. The charge density oscillations and associated electromagnetic fields are known as surface plasmon-polariton waves.[42]

Surface plasmons (SPs) are coherent delocalised electron oscillations that exist at the interface between any two materials that cause the real part of the dielectric function to changes signs across the interface; an example would be a metal-dielectric interface, such as a metal sheet in the air. SPs have lower energy than bulk or volume plasmons, and the charge motion in a surface plasmon thus always creates electromagnetic fields outside as well as inside the metal. The total excitation, including both the charge motion and associated electromagnetic field, may be a surface plasmon polariton, where there is a planar interface, or a localised surface plasmon, in a closed surface of a small particle. The dispersion relationship of SPs is thus an essential theoretical extension of the bulk plasmon calculations. The oscillation frequency, ω, is related to its wave vector k by a dispersion relation $\omega(k)$. Figure 2.1 illustrates a semi-infinite bulk metal surface with the dielectric function $\varepsilon_m = \varepsilon_{m'} + \varepsilon_{m''}$, set next to a dielectric ε_d such as air or vacuum.[43,44] Thus

$$\frac{k_{z1}}{\varepsilon_m} + \frac{k_{z2}}{\varepsilon_d} = 0 \qquad \textbf{2.3}$$

$$k_{sp}^2 + k_{z1}^2 = \varepsilon_m\left(\frac{\omega}{c}\right)^2 \qquad \textbf{2.4}$$

$$k_{sp}^2 + k_{x2}^2 = \varepsilon_d\left(\frac{\omega}{c}\right)^2 \qquad \textbf{2.5}$$

where $k_{z1}$and k_{z2} are the components of the wave vector perpendicular to the interface in the metal and dielectric while k_{sp} is the wave vector of SP, and c is the velocity of light in vacuum. The dispersion relationship of SP can be derived from these equations[44] as

$$k_{sp} = \frac{\omega}{c}\sqrt{\left(\frac{\varepsilon_m\varepsilon_d}{\varepsilon_m+\varepsilon_d}\right)^3} \qquad \textbf{2.6}$$

The real part of ksp is thus

$$\boldsymbol{k'_{sp}} = \frac{\omega}{c}\sqrt{\left(\frac{\varepsilon'_m \varepsilon_d}{\varepsilon'_m + \varepsilon_d}\right)^3} \qquad \mathbf{2.7}$$

To obtain a real $k_{sp'}$, that requires $\varepsilon_m' < 0$ and $|\varepsilon_{m'}| > \varepsilon_d$, and these constraints are satisfied in metals such as Au and Ag. The imaginary part of k_{sp} is

$$\boldsymbol{k''_{sp}} = \frac{\omega}{c}\sqrt{\left(\frac{\varepsilon''_m \varepsilon_d}{\varepsilon''_m + \varepsilon_d}\right)^3 \frac{\varepsilon''_m}{2(\varepsilon'_m)^2}} \qquad \mathbf{2.8}$$

which controls the internal absorption and damping. Where equation (2-2) of the free electron dielectric function is applied to (2-6), the characteristic SP frequency when $k_{sp} \to \infty$ is

$$\boldsymbol{\omega_{sp}} = \frac{\omega_p}{\sqrt{1+\varepsilon_d}} \qquad \mathbf{2.9}$$

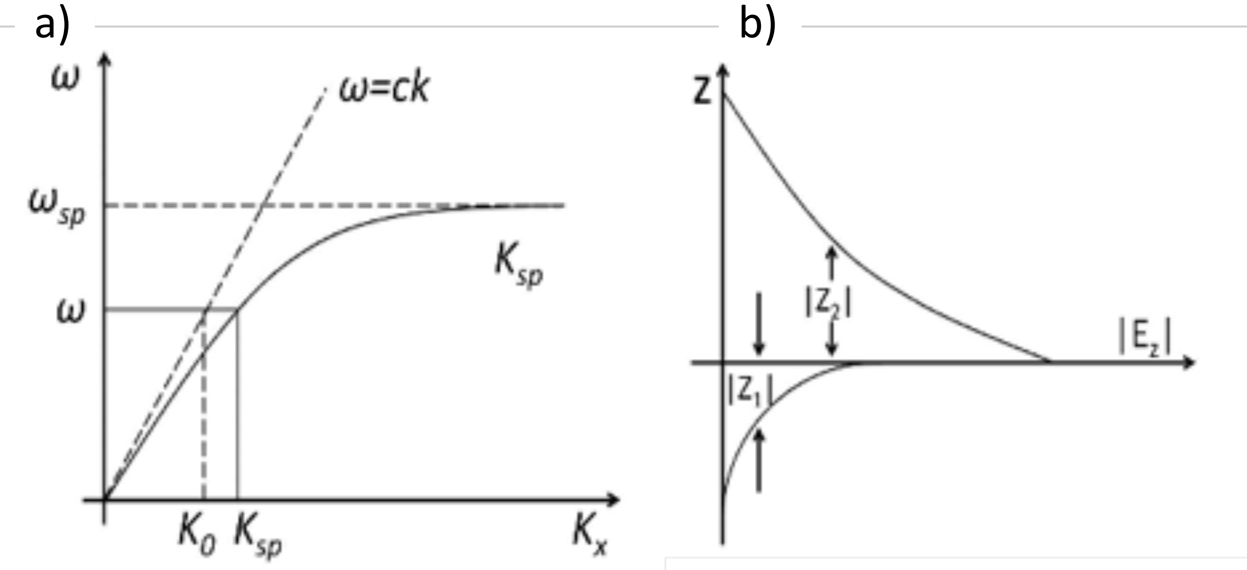

Figure 2.2(A) The dispersion curve of SP, always lying to the right of the light line, with surface plasmon frequency $\boldsymbol{\omega sp}$. 1.2(B) Field distribution in the z direction perpendicular to the interface, implying an evanescent wave.[45]

Figure 2.2a shows that the dispersion curve (k_{sp}) is located to the right of the light line, which illustrates that SPs have a longer wave vector than light waves of the same energy; thus, SPs cannot be excited by free propagating light due to the wave vector gap. Momentum-matching techniques such as grating coupling or a prism are thus required to compensate for the missing momentum to create excitation and SP oscillation. At the surface, these charge oscillations temporarily trap an electromagnetic field, which then decays rapidly into the space perpendicular to the interface (z direction), with a maximum at the interface, as is characteristic for surface waves. This reveals the evanescent nature of SPs, as well as their sensitivity to the dielectric environment at the surface.[46]

The penetration depth is a measure of how deep the electromagnetic field can penetrate into a material. As discussed above, the field intensity of the SPs reduces rapidly normal to the surface as $e^{-k_i|z|}$, as shown in Figure 2.2b. Penetration is thus defined as the depth at which the field intensity falls to $1/e$ (about 37%) of its original value at the interface.[47] In this context,

$$|\boldsymbol{Z_i}| = \frac{1}{k_{zi}} \qquad \mathbf{2.10}$$

For a metal with ε_m,

$$\boldsymbol{Z_1} = -\frac{c}{\omega}\sqrt{\frac{|\varepsilon'_m+\varepsilon_d|}{\varepsilon'^2_m}} \qquad \mathbf{2.11}$$

For a dielectric with ε_d

$$\boldsymbol{Z_2} = \frac{c}{\omega}\sqrt{\frac{|\varepsilon'_m+\varepsilon_d|}{\varepsilon'^2_d}} \qquad \mathbf{2.12}$$

The persistent field distribution in the z direction persistent by penetration depth is of critical importance to plasmonic sensor performance

2.2.1 Experimental investigation of plasmon modes

The momentum of the incident light beam must be matched to that of the plasmon or polarization parallel to the plane of incidence. This is achieved by passing the light through a prism to increase its wavenumber and momentum, yielding resonance at a given wavelength and angle. Plasmons cannot be excited by s-polarised light as electronic and magnetic surface plasmons obey the dispersion relation rule. Thus, surface plasmon resonance occurs only with p-polarized light. Surface plasmons are usually divided into two types: Surface Plasmon Polaritons (SPPs), and the

Localised Surface Plasmons resonance (LSPRs). Physically, there are no differences between the SPPs and LSPRs, with the difference occurring primarily due to their boundary condition. Plasmon modes can thus be characterised by their propagation length and propagation constant. The plasmon decays with the square of the electric field, while the propagation length, defined as the distance over which the SPP intensity decays by a factor of 1/*e*, is $1/2k_x$".

2.2.1.1 Surface plasmon resonance (SPR)

Surface Plasmon Resonance (SPR) is an analytical method that uses light to analyse the contents of a sample for a desired molecule; the quantity of this molecule (as shown in Figure 2.3).[48] In the chip shown, the total internal reflection of the incident light beam leads to the creation of an evanescent wave in the glass plate that can couple to a surface plasmon propagating at the metal-dielectric interface where the metal film is not too thick. The absorption of a portion of incident light causes the reflected light to become less intense based on the reflection angle, with the angle associated with the lowest reflected light intensity being known as the resonance angle or SPR angle.[49] The latter displays sensitivity to the refractive index of the fluid closest to the gold side, and surface binding events cause it to undergo alterations, allowing analytes to be detected in a label-free manner. The real-time modification of the SPR can be depicted by plotting the SPR angles in relation to time in a graph referred to as a sensogram. The resulting sensogram is informative not only about the proportion of analytes bound to the surface, but also about their kinetics. This is important, as the association/dissociation rate and general interaction robustness can be derived from the kinetic data.

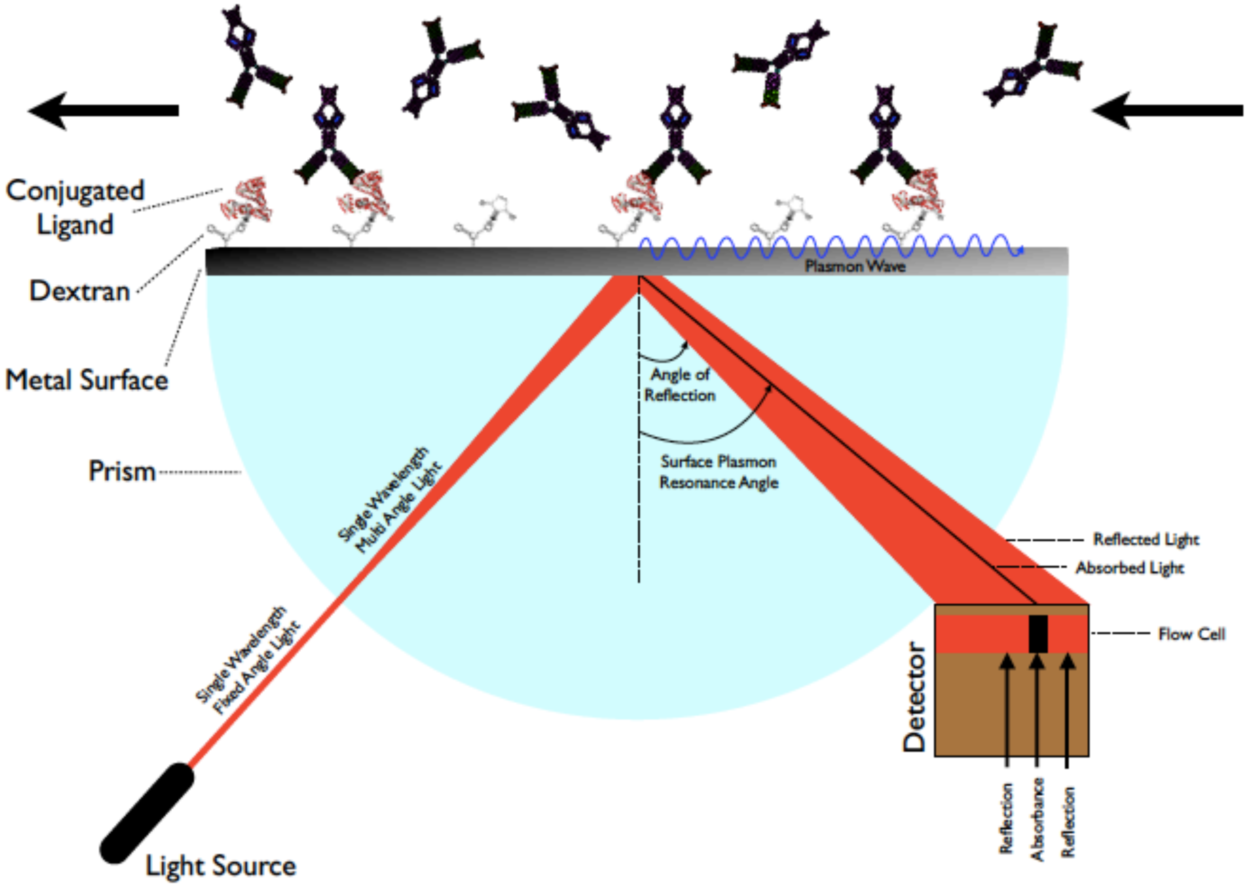

Figure 2.3 Schematic diagram of SPR setup in Kretschmann configuration consisting of an optical part (light source, prism and detector), sensor chip and a liquid handling system (fluidics). SPR metal surface: This figure shows the configuration of an SPR chip. The metal chip (silver or gold) is prepared with a dextran surface which can bind the NH_2 end of protein to conjugate them to the metal surface. At the bottom a single wavelength laser beam enters a prism which results in many light angles striking the metal surface, all of them are reflected except for the angle in which the metal will absorb and turn its energy into a plasmon wave onto its outer surface, at this angle no light is reflected and thus appears with very little intensity on the detector. Since the plasmon wave propagates on the outer side of the metal, any interaction with the conjugated protein will change the resonance angle.[50]

Incident light diffraction into the metal-dielectric interface plane can be induced by intermittent metal surface corrugation, which causes light to couple with SPs in a resonant manner. Figure 2.4a shows in simplified form how SPs are excited through grating coupling.

Prism coupling or Kretschmann configuration-based coupling is the most basic existing method of achieving this (Figure 2.4b). It involves SP excitation at the metal-dielectric interface at a certain incidence angle, which causes the light reflectance to dip abruptly. As in grating coupling, in prism coupling, the propagating SPs at the metal-dielectric interface react to dielectric environment modifications, causing identifiable alterations in the reflected light at a certain angle during the process of adsorption on the surface of the metal, which causes the effective refractive index of the surface to shift.

Waveguide-based coupling (Figure2.4 (c)) involves the injection of light into the wave-guiding layer, followed by its propagation via total internal reflection. SPR then occurs at the metal-dielectric interface due to the evanescent field produced close to the waveguide boundary.

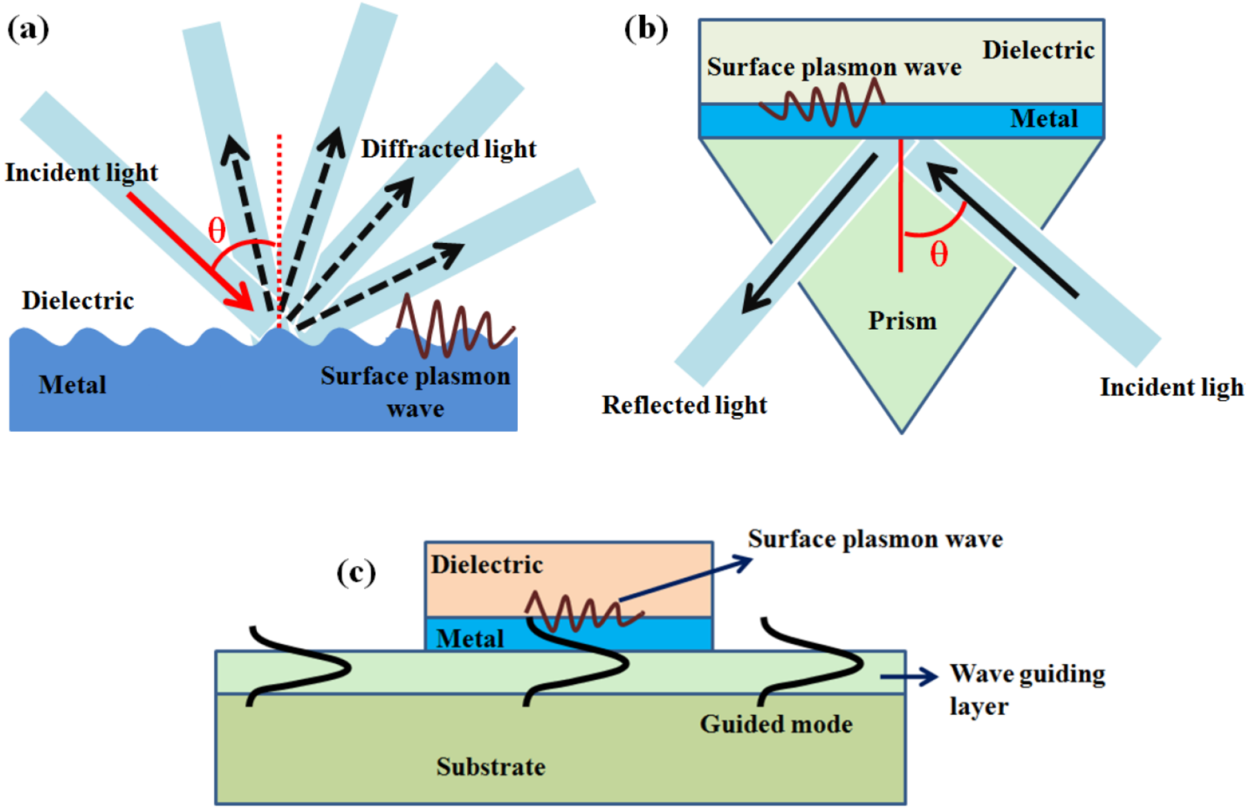

Figure 2.4 Schematic diagram showing mechanisms by which incident light can couple with surface plasmons (SP) to generate SPR.[25] (a) Grating coupling; (b) prism coupling (Kretschmann configuration); and (c)waveguide coupling.[51]

SPs are closely restricted to the surface of the metal, and their propagation occurs in both the x- and y-directions along the interface between the metal and dielectric materials over spans of tens to hundreds of microns. SPs also undergo evanescent decay in the z-direction, with 1/e decay lengths of 200 nm. This is indicative of the binding of SPs to the surface of the interface between the metal and dielectric materials. SPs have multiple uses in terms of chemical and biological sensing due to their high sensitivity to alterations in the local dielectric medium near the metal surface, and the fact that SP excitation can only occur after any momentum incompatibility between the incident light and SPs is resolved.

2.2.1.2 Localised Surface Plasmon Resonance

Early Roman experiments with glass-making revealed that the incorporation of small amounts of gold into glass produced a characteristic ruby coloration. More than a thousand years later, Faraday studied the abnormal optical features displayed by gold colloid solutions, providing an explanation for the creation of this ruby glass.[52] During the glass-making process, gold colloids are formed, leading to strong absorptions now attributed to localised surface plasmon resonances. Compared to the incident wavelength, the metallic NPs encapsulated in ruby coloured glass are significantly smaller (~5 to 60 nm). As a result of the interaction between light and these subwavelength NPs, a plasmon emerges that displays local fluctuation around the NPs at a frequency known as the localised surface plasmon resonance (LSPR).[53,54]

The Mie theory is a crucial resource for comprehending how particles scatter light.[55,56] Since its creation in 1908 by Gustav Mie, it has been used to investigate a variety of physical processes, from the interaction of light with biological systems to the scattering of light by atoms and molecules. Mie drew on Faraday’s work and proposed an analytical solution to Maxwell’s equations that defined the extinction spectra associated with round NPs of random dimensions.[57,58]

Mie theory can thus reasonably accurately predict spectra of plasmonic nanoparticles under certain condition. The light-SP interplay was then identified in 1970 as the reason for the emergent in glass encapsulating metallic NPs.[59]

Mie scattering is the elastic scattering of light by particles with a diameter equal to or greater than the incident light's wavelength. The square of the particle diameter thus determines the Mie signal, and the mathematical relationship between the diameter of the particles (d) and the Mie signal (S) is described by the Mie scattering theory.[60] The formula for the Mie signal is given by:

$$S = f(\lambda, d)$$

where S is the Mie signal, λ is the wavelength of the incident light, d is the diameter of the particles, and f (λ,d) is a function that depend on the both the wavelength and particle size. The Mie signal is proportional to the square of the particle's diameter. Due to the nature of the dielectric-metal interface between the medium and the particles, plasmonic nanoparticles can couple with electromagnetic radiation of wavelengths much larger than the particle; however, in contrast to pure metals, where there is a maximum limit on the size of wavelength that can be effectively coupled based on material size.[42,61] Based on their shapes and relative placements, plasmonic nanoparticles also display interesting scattering, absorbance, and coupling characteristics. This causes enhanced light scattering and absorption at specific wavelengths, resulting in phenomena such as localized surface plasmon resonance (LSPR) and surface-enhanced Raman scattering (SERS). Furthermore, at their surfaces, plasmonic particles display substantial electromagnetic field enhancements, resulting in highly localised and intense scattering effects. Due to these distinctive characteristics, they have become the subject of research in a variety of fields, including spectroscopy, imaging signal enhancement, and cancer therapy,[62,63] offering excellent options for the design of mechano-optical instrumentation due to their high sensitivity.

The coupling of light to metallic particles significantly smaller than the incident wavelength gives rise to an oscillating dipole, a surface plasmon polariton. As the polariton is confined to the surface of a nanoparticle. (Figure 2.5), this phenomenon is referred to as localised surface plasmon resonance (LSPR). In addition to absorption, the interaction between the light and sub-wavelength particles also gives rise to significant scattering. The interplay between light and metallic NPs is shown in Figure 2.5.

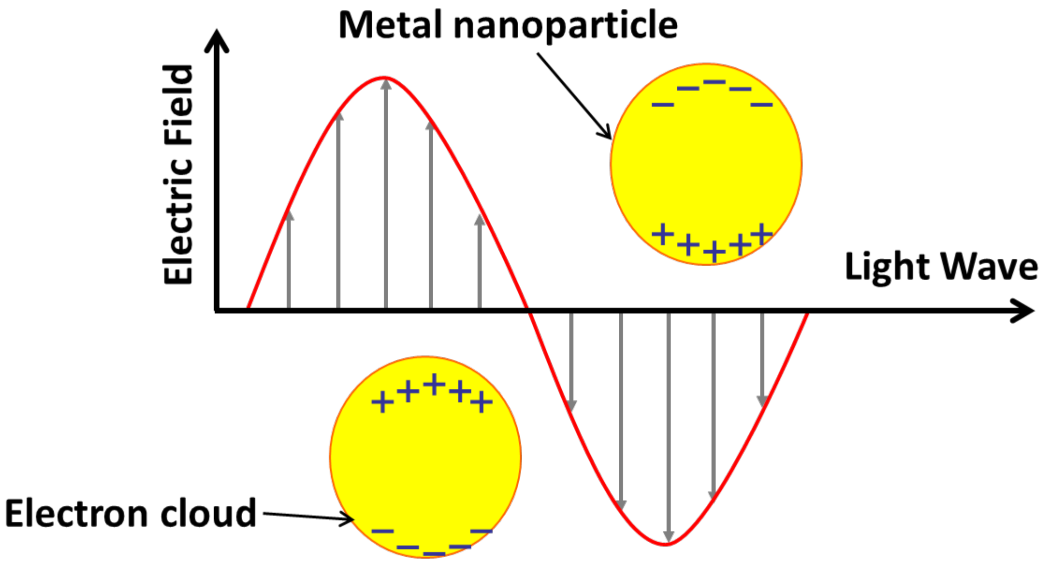

Figure 2.5 Schematic diagram of a plasmon oscillation for a metallic sphere showing the displacement of the electron cloud, positive charge and the fixed atomic nuclei.

Light irradiation of a small round metallic NP determines coherent oscillation of the conduction electrons under the effect of the oscillating electric field. In the context of electron cloud displacement in relation to the atom nuclei, a restoring force is produced by the Coulomb force between the nuclei and electrons that causes the electron cloud to oscillate collectively with respect to the immobile nuclear array of LSP. The implications of the LSP are both major enhancements and rapid declines with distance in the electric fields close to the surface of the NPs, and the achievement of a maximum based on the optical extinction of the NPs at the plasmon resonant frequency LSPR, which occurs at visible wavelengths in the case of noble metal NPs. The plasmon energy is determined by the shape and dimensions of the metal nanoparticle and the refractive index of the medium, which also influence the performance of the plasmonic nanostructures, including their refractive index sensitivity, in sensing applications.[58]

Plasmonic nanoparticles have a unique property known as "plasmon resonance," that refers to the way in which they can absorb and scatter light at specific wavelengths. This feature makes them valuable for many optical, photonic, and nanotechnology applications. They can enhance optical signals by enhancing light intensity at specific wavelengths,[64] which can improve the performance of lasers, microscopes, and other optical tools.[65,66] Plasmonic nanoparticles can also produce highly sensitive sensors that detect light intensity or wavelength changes[67] that can be used for medical diagnostics or environmental monitoring. The effects of gold nanoparticles on signal enhancement include increased surface mass as a result of increased surface area, larger changes in refractive index due to the mass of the particles, and electromagnetic field coupling between the plasmonic properties of the particles (LSPR) and the propagating plasmons.[68] Lyon et al.[69] and Hutter et al.[70] published the first reports on the impact of Au NPs on SPR signal, and it has since been demonstrated that the width and efficiency of the SPR are affected by such additions, based on comparing experimental SPR data for gold substrates with and without 25 to 30 nm diameter particles connected to the substrate metal via a sandwiched monolayer of 1,6-hexanedithiol.

Despite the fact that SPR has been utilised for the biomolecular detection of tumour biomarkers previously, it presents some experimental challenges that may be resolved by incorporating nano-hole arrays into metallic films. This configuration demonstrates superior optical transmission, and it is thus now utilised for monitoring biointeractions on the plasmonic metal surfaces.[71,72] This biosensor type demonstrates excellent sensitivity and linearity. For the detection of the human epidermal growth factor receptor 2 (HER2) antigen, the surface can be coated with AB1 (biotinylated antibody) via its interaction with streptavidin molecules that have previously been immobilized. The HER2 antigen is then immobilised, and the AB2 antigen introduced to the surface. Using a secondary antibody, characteristic of the sandwich detection mode, increases the sensor's sensitivity, and as molecules become immobilised on the surface, the refractive index increases at the metal-dielectric interface, resulting in a redshift.[73]

One of the basic facts regarding plasmonic nanoparticles is that they can concentrate light into very small areas.[6,74] This phenomenon is referred to as a plasmonic hotspots, and it can be used to make optical fields with very high intensity, which can be used for sensing, imaging, and photothermal therapy, among other things. Plasmonic hotspots can also be employed to improve the performance of solar cells by concentrating sunlight onto the surface of the cell. Plasmonic nanoparticles can also transform light energy into thermal energy via an ability is known as "plasmon-induced heating", which has been employed in various applications, such as photothermal therapy for cancer treatment and photothermal ablation for tissue excision.[75] Plasmon-induced heating has also been utilised to move small objects precisely with optical tweezers.[76] Optical tweezers utilise several effects, including trapping forces, trap stiffness, and the interference effects in spherical particles, as well as those between particle size and relative refractive index.[77] Optical tweezers use a beam of laser light, focused through a microscope objective lens, to trap, move, and apply calibrated forces to microscopic refractive objects.[78] Optical tweezers act as multifunctional tools in a myriad of applications. including micromanipulation, nanofabrication, and biological studies of DNA, cells, offering access to biological micrometers.[79]

In addition to these characteristics, plasmonic nanoparticles can be utilised for surface-enhanced Raman spectroscopy (SERS),[80] a technology that uses plasmonic hotspots to amplify the Raman scattering signal from molecules adsorbed on a nanoparticle's surface. This method has been implemented in numerous disciplines, including chemical analysis, biosensing, and medication delivery.[81]

In addition to their use in optics and photonics, plasmonic nanoparticles have many potential applications in nanotechnology. For example, they can be utilised to make nanoscale circuits or devices that interact uniquely with light.[82] Plasmonic nanoparticles can also be utilised to produce tiny antennas capable of transmitting data over short distances without wires or cables.[83] Finally, plasmonic nanoparticles have been investigated as a potential method for delivering medications directly into cells without causing cellular damage.[84,85]

Plasmonic nanoparticles are an innovative new technology with numerous potential applications in various disciplines. The ways they are made, make them particularly effective at amplifying optical signals, allowing the creation of nanoscale sensors and devices and permitting accurate imaging for photothermal treatment and drug delivery. As research into this technology continues, additional applications will also not doubt develop.

2.2.1.3 Weak Plasmon-Exciton coupling

A key stage of the SERS development process occurred in 1974, when Fleischmann provided the first evidence of SP-organic molecular interaction on rough silver films by means of Raman signal enhancement.[86] At the micro level, scattering enhancement can be undertaken using SP to broaden the light field.[87] Molecular fluorescence can also be improved using SP to generate weak-coupling effects. There are two distinct variations of this, which are classified by their ability to improve levels of either emission,[87] or absorption.[88] Contemporary steady-state spectroscopy is defined by SP-coupled emission enhancement (SPCE). Weak coupling is identified through the lack of EM disturbance in exciton-plasmon interactions; it can thus only occur during exciton dipole coupling in the SP's electromagnetic field.[89] This was thoroughly examined by Drexhage's investigation into planar region surface emission dipoles, with particular consideration given to the rates of excitation decay observed.[90,91,92]

2.2.1.4 Strong Plasmon Exciton coupling

Plexcitons are novel quasi-particles that exist in a hybrid matter-light state which possess definite properties not exhibited by their progenitors. They are formed through strong exciton-plasmon coupling, defined as occurring when the rate of exchange of energy between the plasmon and the exciton is faster than the decay rate of either state.[93] This resonator (photon and exciton) properties in this interaction can be characterised using a variety of techniques, all of which provide novel perspectives with clear opportunities for real world implementation.[94] One further consideration is Bose-Einstein condensation (BEC), which may arise from the light-exciton relationship, which is known to create polarons.[95] Polarons are quasiparticles that form readily in polarizable materials due to the coupling of excess electrons or holes with ionic vibrations. BEC is a state of matter that forms when a gas with bosons at low densities is cooled to a temperature very close to absolute zero. Quantum information processing can only be undertaken where there is an identifiable level of coherent oscillation,[96] and the mediation of chemical reactions, in terms of both rate and initiation threshold, can thus be achieved by using strong-coupling effects to adjust a fluorophore's electromagnetic response.[97] Other applications of this effect, based on the considerable interactions between quantum bits and applied microwave emissions, include single photon switches and detectors and routers.[98,99] It is also typical to describe light-matter interplay in a microcavity as exciton-plasmon coupling.[100] The periodic nature of the light-matter energy transfer ensures that resonance of both the microcavity and matter is observable in the associated reflection and transmission spectra.

Rabi splitting, also known as anticrossing dispersion, is also observed in the strong coupling regime,[94] and this is perhaps best comprehended through its associated oscillations. The Rabi frequency is defined as the rate at which a bi-level population fluctuates in a material under laser illumination. The pulse duration must be set such that it exceeds both the excited particle lifetime, and the material relaxation time. It is also widely held that the combination of both linear and non-linear responses that arises due to electron excitation in a medium as a result of light-matter interaction is the fundamental source of many larger scale physical systems.

Periodical Rabi oscillations are defined as occurring when two-state quantum systems are subjected to energy transitions via an oscillatory driven field. Light-harvesting (LH) pigment-protein complexes that absorb light and then transport excitation energy to the reaction centre initiate photosynthesis.[101] Adding plasmonic particles to LH complexes is thus a viable way to improve and gain control over light harvesting.[102] In organic photovoltaics, plasmons couple with the light-harvesting complex II (LHCII) to improve optical performance.[103] Due to its extremely effective energy conversion, LHCII offers excellent capacity for solar energy harvesting. For instance, surface plasmon resonances on gold nanostructure arrays split effectively when light harvesting complexes 1 and 2 (LH1 and LH2) drawn from purple bacteria are included: strong coupling between the localised surface plasmon resonances and excitons in the light-harvesting complexes is thought to be the cause of this splitting. [104]

2.3 Uses of sensing

Recently, attention in the field of plasmonic has moved towards technological applications ranging from information technology devices to biological sensors.[105,106,107] Research in this field has facilitated significant enhancement of the understanding of interactions between photons and SP at the nanometer scale. SP modal properties have been studied in bulk objects fabricated by e-beam lithography or by colloidal chemistry; however, recently, there has been more interest in the use of three-dimensional (3D) nanostructured metallic objects structured at the nanometer scale due to the ability to sculpt their optical properties in 3D.[108] Au, Ag, and Cu are the metals most extensively used to support SP waves in the UV-visible and NIR range, and they offer a wide range of advantages for applications such as chemical sensors, including facile surface chemistry for the immobilisation of molecular recognition components;[109] simple integration with microfluidics, leading to minimal device footprints; and high sensitivity.[110] Chemically reducing these bound ions makes it easy to make metal NPs, while immobilising biomolecules on biosensing surfaces is a significant step in making biosensors.[109] As plasmonics becomes a mature field, this capacity, coupled with the availability of durable samples capable of multiple reuses, may be assumed to be becoming increasingly important.[111]

Various sensing applications can be derived from the morphological customisation and enhancement of refractive index (RI) sensitivity. In particular, metal NPs can be employed to achieve surface alterations and generate a selective layer. SPR were first used in 1982 for the purpose of gas detection[112] before being subsequently applied to biosensing instruments to measure antibody adsorption.[113] Furthermore, as they demonstrate high confinement, SPs may be relevant for various applications where a diffraction limit must be overcome, including plasmonic lens-based subwavelength focussing[114] and subwavelength lithography.[115,116]

2.3.1 Biosensing applications of plasmonic materials

In contrast to SPR sensors, localised surface plasmon resonance (LSPR) sensors, which occur "as a result of the confinement of a surface plasmon in a nanoparticle", demonstrate greater compactness, portability, and cost-effectiveness owing to the underlying nanotechnology. LSPR sensors intended for biosensing are label-free, in a similar manner to SPR sensors. The LSPR method has the critical implication for analysis that it can minimise the quantity of required analyte due to its capability in terms of single particle sensing. Unfortunately, the signals emitted by particle sensors are commonly not strong enough for immediate use, leading them to require amplification in most cases.

A number of selective interactions (e.g. enzyme, biotin-avidin, antibody-antigen, aptamer-protein, DNA-based) underpin the LSPR sensor selectivity to bioanalytes. LSPR sensors are usually produced by immobilising one of the pairs on an NP surface, with LSPR spectra undergoing transformations during the binding of this to the other pair, thus allowing the particular bioreagent involved to be identified.

2.3.2 Biosensor Detection in COVID-19

Instead of using antibodies to detect COVID-19, researchers at Newcastle University created a quick test that uses molecularly imprinted polymer nanoparticles.[117] The first step was to affix a peptide from the SARS-CoV-2 spike protein to a sturdy support. In order to create nanoparticles with a unique binding site for the coronavirus spike protein, they added nanoparticle building pieces and polymerised these around the peptide. They then separated the nanoparticles that bonded to the peptide most firmly and adhered them to an electrode with a screen-printed pattern. They first demonstrated the ability of the molecularly imprinted polymer nanoparticles (nanoMIPs) to bind SARS-CoV-2, and then connected an electrode to a small 3D-printed device to track any changes in thermal resistance during binding.[117] Samples that had previously tested positive for Covid-19 by RT-PCR showed a change in heat resistance, according to these researchers, and the test took only 15 minutes. The preliminary findings also suggested that it was 6,000 times more sensitive than a commercial quick antigen test for detecting SARS-CoV-2.

2.3.3 Binding method based on biotin-avidin interaction

Based on its robust conjunction and specificity, as well as being widely available on the market, a binding method based on the interaction between biotin and avidin is often employed in the context of LSPR biosensing. With a molecular weight of about 50 kDa, avidin is a large protein molecule that is commonly known as tetrameric glycoprotein due to its four particular binding sites for biotin.[118] Biotin and avidin display remarkable affinity, with a dissociation constant (k_d) of around 10^{14} M^{-1}. This allows sensors to be fabricated with an LOD level within a range of just a couple of femtomolars. Furthermore, the small size of biotin molecules also makes the fabrication process much easier as they can be easily immobilised onto the sensor substrates. Adaptation of the interaction between biotin and avidin is based on the four binding sites available,[119] which can be useful in sandwich-type assays. These can be developed by using a pair of receptors to bind to different sites of the same target to improve sensing capacity. Moreover, there is evidence of various LODs ranging from pico molar to micro molar level, that can be generated using the same interaction. Several factors can explain this potential massive difference, including sensor setup discrepancies, the nature of the employed metals, morphological factors, and the experiment setting.

One study of silver nanotriangles fabrication using Nanosphere lithography (NSL),[120] saw this low-cost technique used to fabricate large-area periodic nanostructures based on the tunability of nanostructure size, period, and material, and this indicated an LOD better than pM, equivalent to less than 100 streptavidin molecules for each NP with silver nanotriangles, based on NSL.[121] A different study observed that streptavidin could be identified in the range between 16 nM and 8μM in a biosensor fabricated by coating a glass substrate with a nanostructured silver film of minimal thickness.[122] Barbillon et al. applied EBL to produce a biosensor of high sensitivity consisting of gold nanocylinders with diameters of 100 nm and distance between particles of 200 nm in glass substrates.[123] The sensor was reported to be capable of reducing the LOD to 1.25×10^{-18} moles for streptavidin, corresponding to 75 molecules for each NP.[124] In a subsequent study, the authors developed gold nanodisks on a glass substrate based on EBL, which showed a lower the limit of detection for streptavidin, reduced to 7 pM.

It was also suggested that an efficient biosensor with low serum LOD (19 nM) and LOD of 94 pM in phosphate buffer solution (PBS) could be achieved by using AuNRs on a glass slide.[125] The superiority of nanoshells as compared to solid spherical equivalents was thus exploited to develop a biosensor capable of identifying streptavidin in blood samples, with 3 μg/mL LOD and 3-50 μg/mL dynamic range. The LSPR of gold nanoshells can be controlled in the near-infrared (NIR) region of the spectrum, where the optical transmission through tissue and whole blood is optimal. Gold nanoshells can thus be used as effective signal transduction in whole blood.[126] Such studies highlight the existing preference for the biotin-avidin interaction as a method for developing LSPR biosensors.

2.3.4 Measurement of antibody-antigen interaction

The interaction between antibody and antigen is also a popular biosensing method, demonstrating high selectivity, potent binding affinity, and straightforward production. Commonly referred to as immunoglobulins (Ig), antibodies are sizable Y-shaped glycoproteins, products of the immune system that are designed to detect and eradicate foreign agents.[127] The selectivity of the antibody-antigen interaction derives from the fact that the tips of the Y shape are binding sites for specific antigens that work in a manner akin to a lock and key mechanism. This interaction is the highly suitable for developing sensors with a detection limit in the nM-pM range. Ka is the equilibrium constant for such reactions, and this can be calculated from the ratio of the molar concentration of bound Ag-Ab complex to the molar concentrations of unbound antigen and antibody at equilibrium as follows for the association constant K_a (see below, Ab=antibody, Ag=antigen):[128]

$$Ab + Ag \rightleftarrows Ab\!:Ag$$

$$\boldsymbol{K_a} = \frac{[\mathbf{Ab}\!:\mathbf{Ag}]}{[\mathbf{Ab}][\mathbf{Ag}]} \qquad \mathbf{2.13}$$

An antibody / antigen biosensor configuration typically involves antibody immobilisation on a metallic nanomaterial surface. As the antibody and target antigen interact, LSPR spectra undergo modifications owing to the binding-induced alteration in the surrounding refractive index.

The antibody-antigen interaction has been the focus of extensive research, and the technique has a wide range of applications owing its capability of biological antibody production in reaction to the majority of antigens. In particular, the technique has garnered interest with regard to pathogen identification due to the straightforward nature of the sensing mechanism. The antibody-antigen interaction has thus already served as the basis for detecting Salmonella,[129] Alzheimer's disease biomarkers[130] hepatitis B virus,[131] and influenza virus.[132] Assessment of the sensing capability of various systems has also been performed based on human, goat, or rabbit antibodies.[133,128,134] This type of sensing system may have an LOD of just a couple of the colony forming units (CFU)/mL.[135]

2.3.5 Sensors for pH

Sensors to detect pH with a specific sensing range can be developed by integrating plasmonic NPs in materials with pH sensitivity. One study employed block co-polymer PMAA-bPNIPAM to prepare AuNPs, producing a pH sensor that functioned within the 5 to 8 pH range.[136] A dithiobenzoate chain was used in the copolymer preparation, which facilitated binding to the AuNP surface. The optical characteristics of the system were observed to be a function of pH as the binding event was influenced by pH. Unfortunately, this system is significantly affected by temperature and the resulting aggregation of particles was permanent. In another study, plasmonic crystal was used to develop a pH sensor. The plasmonic crystal represented a gold-coated nanowell array produced via gold film thermal evaporation on a pre-established substrate, with the latter being subsequently covered in a thin hydrogel film to yield a pH sensing layer. This enabled the detection of pH within the 1.44 to 7.86 range, with 0.1 pH unit accuracy.[137] What made this technique most effective, however, was the reversibility of the sensing mechanism. Jiang et al. also developed a gold nanocrescent system with a poly-HEMA hydrogel coating that yielded a pH sensor of high sensitivity, with 0.045 pH unit accuracy in the sensing range 4.5-6.4 pH.[138] Furthermore, even after this was kept in storage for 30 days, the sensor demonstrated both stability and repeatability.

2.3.6 Plasmonic nano-antennas

The previous section discussed the close interaction between metal NPs and light, demonstrating that, through incident light absorption and concentration in a sub-diffraction limited volume, NPs display receiving antenna behaviour. Furthermore, NPs can also display emitting antenna behaviour by effectively coupling out stored energy. Based on these properties, NPs could be employed to enhance and manipulate the interplay between light and emitters, offering advantages across a range of domains, including surface-enhanced fluorescence (SEF)[139] surface-enhanced Raman scattering (SERS)[140] plasmonic solar cells,[141] nanomedicine,[6] and sensing.[142] The applications of greatest current interest are thus introduced in the next section.[143,144,145]

Nano-antennas are capable of exceptional enhancement and confinement of electric fields. This is of significance in a number of areas, including surface-enhanced fluorescence, surface-enhanced Raman scattering spectroscopy, plasmonic solar cells, and nanomedicine

In a recent study, Li et al.[146] proposed a noteworthy SERS application that involved the use of gold NPs with silica or alumina shell of minimal thickness to amplify the Raman signal in a novel spectroscopy method referred to as shell-isolated NP-enhanced Raman spectroscopy. In this context, the surface intended for probing was be coated with NPs as a monolayer, with NP aggregation and direct interaction with the examined material prevented by an ultrathin layer that covering the metal NPs. The electric field is thus robustly enhanced, and Raman spectra of high quality are generated owing to the minimal gap of about 2 nm separating the NPs.

A dynamic sensor demonstrating label-free, real-time detection was developed by Fernandez-Cuesta et al.[147] This sensor was capable of sequential identification and counting of each molecule and particle within the original medium, regardless of concentration. The underlying principle was the integration of a 35-nm gap plasmonic bowtie antenna with a 30x30-nm^2 nanochannel, the latter supplying an analyte directly to the hot spot through the antenna gap. The authors observed changes in dark field resonance in the process of filling with a liquid lacking fluorescence, thus demonstrating the mechanism of antenna probing into zeptoliter volumes within the nanochannel.

Furthermore, single quantum dots were consecutively identified and counted at extremely high concentration of up to 25 mg mL^{-1}. In contrast to the diffraction limited spot, the observation volume was diminished five orders of magnitude by light nano-focusing, thus surpassing the limit of diffraction.

2.4 Comparative analysis of SPR and LSPR

Label-free and real-time kinetic data for binding processes can be derived from both SPR and LSPR spectroscopy. In 1990, Biacore International AB introduced the first SPR biosensor to the market[148], and since then, the usage of SPR biosensors has expanded considerably. Conversely, the market availability of LSPR biosensors remains limited, as LSPR research is not yet as extensive as SPR research. Biotin-streptavidin binding has been employed for the comparison of SPR and LSPR, revealing that the bulk refractive index sensitivity of SPR sensors is significantly higher than that of LSPR sensors (3300 vs 178 nm/RIU).[149] It has also been established that LSPR possesses an extremely small actual sensing volume due to its EM field decay being 40 to 50 times shorter than that of SPR. However, where measurement of short-range refractive index alterations caused by a biomolecular adsorption layer in biological applications is required, the two methods operate quite similarly.[119,150] The LSPR sensing surface has a gold-coated area that is a fourth of the area of the SPR sensing surface; however, an LSPR has higher sensitivity (ng/cm^2).

LSPR is thus more advantageous than SPR. For instance, LSPR sensors can detect minute quantities of adsorbents owing to their small NP dimensions and the possibility of integration with microfluidics. A thick polymer capture layer or matrix is typically necessary in the case of SPR and this must be suffused with analyte as a prerequisite for the emission of a signal that can be detected. Furthermore, LSPR sensors possess miniaturisation capability as, unlike SPR, LSPR has a more straightforward setup, allowing coupling to take place without a prism. In terms of costs, a commercial SPR system is around £ 150,000, whereas an LSPR system assembled at home is cheaper than £20,000.[7] Additional innovations are likely to make LSPR even more cost-effective however, and one strategy for significantly cutting costs is to employ an LED alongside a basic photodetector instead of using a white-light spectrometer.

2.5 Micro and Nano-patterning techniques

Plasmonic devices and materials enable light routing and manipulation at nano-scale. Plasmonic structures can thus be adapted for specific technological applications by optimising the distinctive optical characteristics of metallic nanostructures. The potential integration of plasmonic, electronic, and traditional dielectric photonic devices on the same chip allows the exploitation and combination of the benefits of each technology, thereby generating incredible synergy. The unique surface specific characteristics and diversity of possible applications of plasmonic nanostructures devices have thus made them a source of huge interest in a wide range of technologies. Plasmonic nanostructures can be created via several cutting-edge lithographic methods, including colloid lithography, electron beam lithography, and photolithography, all of which are described in this chapter. To facilitate integration into chip-based devices, there is, however, further demand for advancements in fabrication methodologies, with a particular clamour for fast, inexpensive routes for the production of structures that cover large areas yet remain programmable. An important goal in this field is thus to produce innovative optical components and systems with sizes comparable to the smallest modern integrated circuits, which could eventually be incorporated with the requisite electronics on the same chip. These components might thus be integrated into electronic chips to facilitate plasmonic data production, transportation, and identification.

In the following sections, the production of plasmonic devices is thus discussed. The two approaches most widely used in the literature, electron beam lithography (EBL) and colloidal lithography, are thus examined first. EBL offers the highest degree of precision, and it has been used to produce arrays of nanostructures with precisely engineered morphologies such as bow tie structures that display field enhancements at specific locations. However, the use of EBL requires very expensive apparatus and highly skilled operators. An alternative approach is the use of colloidal lithography, in which nanostructures are synthesised in solution and subsequently transferred to a solid phase. However, colloidal lithography offers comparatively little flexibility in terms of the design of arrays of nanostructures.

In this work, an alternative approach is thus also explored, based on IL, which promises to be much cheaper to implement than EBL while offering, in principle, more flexibility and a higher degree of programmability in terms of nanostructure fabrication than colloidal lithography. Moreover, it does not require a cleanroom and it is scalable being based on IL techniques designed to process one-foot wafers in semiconductor fabrication lines. It is thus hypothesised that IL is a method that can combine the flexibility and control of EBL with and some of the ease of implementation of colloidal lithography.

2.5.1 Colloidal lithography

Colloid lithography exploits the self-organising properties of thin films of colloidal nanoparticles, which tend to form close-packed hexagonal assemblies as they dry.[151] It is thus also a cost-effective, easily managed method with a strong output and no excessive or complicated equipment requirements.[34] Colloidal lithography is also a straightforward and effective strategy for surface patterning. The process requires upstream preparation, colloid alteration, and downstream nanostructure self-assembly. Metal is evaporated onto a film of nanoparticles, which acts as a resist. Metal predominantly deposits on top of colloidal particles, passing through the film at triangular interstices in the hexagonal array. Thus, when the particles are removed subsequently, a nanostructured of metal remains where interstices were present in the self-assembled film. The sizes of these features range from a few micrometers to tens of nanometers with high levels of controllability. Spin-coating, drop coating, or evaporation can be used to enable the sphere layers to self-construct on a substrate surface.[152]

Over recent decades, the colloidal science field has made significant advancements. The synthesis of intensely monodispersed colloidal spheres such as polystyrene (PS), polymethyl methacrylate (PMMA), and silica with narrow size distributions and effective phase stability has been achieved via suspension,[153] emulsion, dispersion polymerisation, and Stöber methods.[154,155] Accurate modulation of colloidal spheres' diameters is also possible, with result ranging from a few micrometers to tens of nanometers, giving results similar or superior to traditional lithographic approaches. In suitable environs, these colloidal spheres can also self-construct 2D and 3D colloidal crystals. Fisher and Zingsheim first introduced the lithographic approach employing a self-constructed PS monolayer as a mask to produce a Pt pattern in 1981.[34,156] Subsequently, Deckman et al. accomplished scaling of the mask to a considerable area to facilitate patterning.[157] From that point on, 2D colloidal crystals garnered significant interest due to them being effectively employed as adaptable templates or masks in surface patterning. Colloidal or nanosphere lithography refers to any production processes, whether end to end or partial, that encompass the self-construction of a monolayer of colloidal crystals (MCCs), while maintaining control of their morphology, and functionalised decoration.[158]

Clearly, the main drawback of these methods is that the particle shape and particle array geometry are rigid, even where the particle size can vary. In order to better address these limits, several adjustments have been made to NSL. In relation to the deposition vector, for example, the size and shape of the hole can be changed by modifying the angle of deposition.

Nanohole-based biosensors are among the most promising biosensor platforms in the coming generation due to their size selectivity and position-dependent sensing features.[159] Figure 2.6 (a-c) illustrates SEM images of various Au nanohole arrays. From the SEM pictures, the average diameters of the nanoholes in the three arrays were 156 ±9 nm, 210 ±14 nm, and 238 ±9 nm, which were created by 156, 200, and 230 nm colloid masks, respectively. The smallest hole size possible was thus around half the original sphere diameter. The film thickness for the larger holes proved difficult to manage, however, due to shadowing by neighbouring mask colloids during film deposition. The film deposition rate for larger holes was significantly lower than that of a plane film without structure. The average film thickness of these three samples was kept to around 25 nm by changing the thickness for each colloid size. Figures 2.6(d) to 2.6(f) show the measured optical transmission spectra of the samples shown in the SEM pictures (Figure 2.6(a) to 2.6(c), respectively). The transmission dip wavelengths were 561, 569, and 631 nm, with transmission peaks at 695, 692, and 840 nm for the 156, 210, and 238 nm holes, respectively. The effective periodicity was constant at 277 nm for all samples that corresponding to the original colloid mask packing.

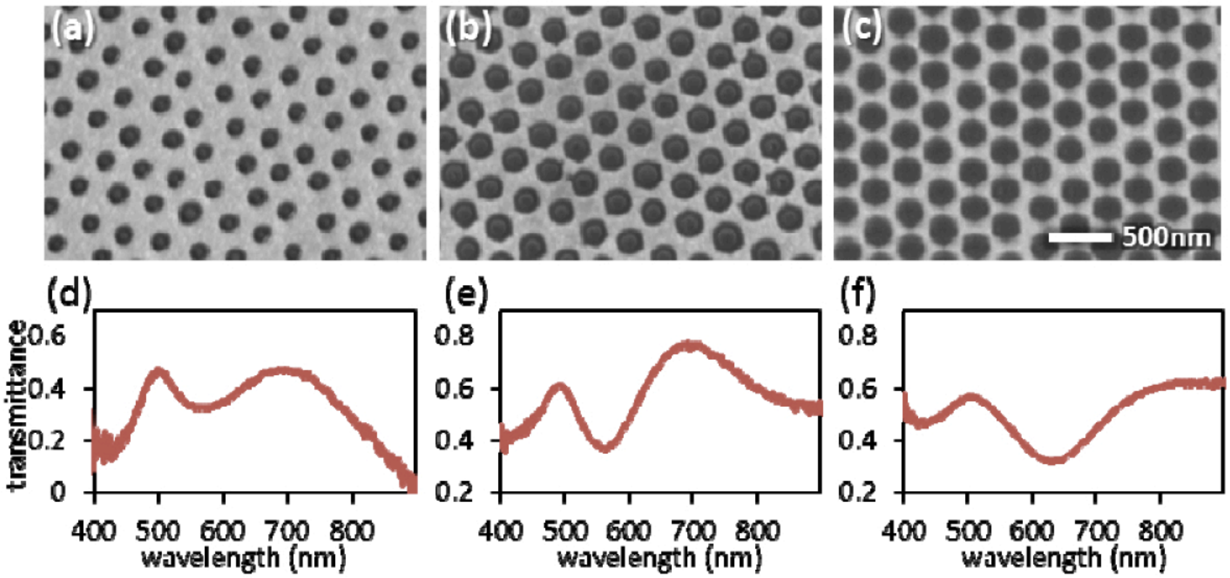

Figure 2.6 SEM images of Au nanohole arrays with a diameters of (a) 156 nm, (b) 210nm, and (c) 238 nm, and (d-f) respectively corresponding optical transmission spectra.[159]

2.5.2 **Electron Beam Lithography**

EBL is a method by which a pattern is formed based on exposing a radiation sensitive resist to electrons. After development, the resist pattern is transferred to the substrate by means of etching or lift-off processes.[160,161] EBL is one of the primary direct-write techniques for the high-resolution fabrication of nanostructures. The sensitive layer of the e-beam resist is deposited on a substrate by spin-coating; it is then exposed to a focused beam of electrons to generate a chemical change in both positive and negative resists. Electron beam exposure causes polymer chain scission in positive resists, decreasing the polymer chain length; therefore, the exposed area in the resist is thus more easily dissolved in the developer than the unexposed resist. After electron beam exposure of negative resists of polymer chains in the exposed areas become cross-linked and, making it more difficult to dissolve the resist using the developer. The exposed areas in the resists are therefore dissolved in positive resists and remain in negative resists.[162,163] The developed pattern can then be employed for pattern transfer processes such as lift-off or etching as seen in Figure 2.7.[164]

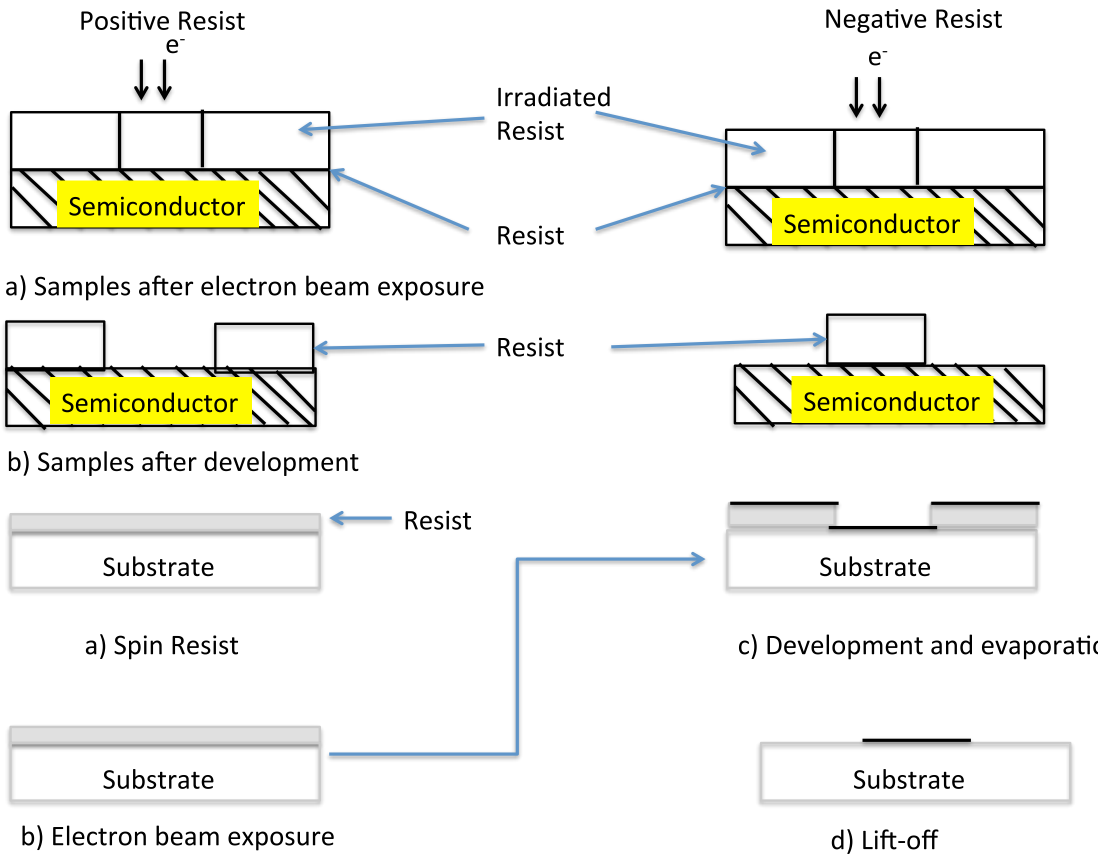

Figure 2.7 Schematic diagram of the process of EBL technique. A substrate by spin-coating and exposed using a focused beam of electrons to generate a chemical change in both positive and negative resists

As previously indicated, in addition to size and spacing, the resonances of plasmonic particles also depend on their form and assembly. Electron-beam lithography thus provides a variety of shapes and configurations, as seen in Figure 2.8.[165]

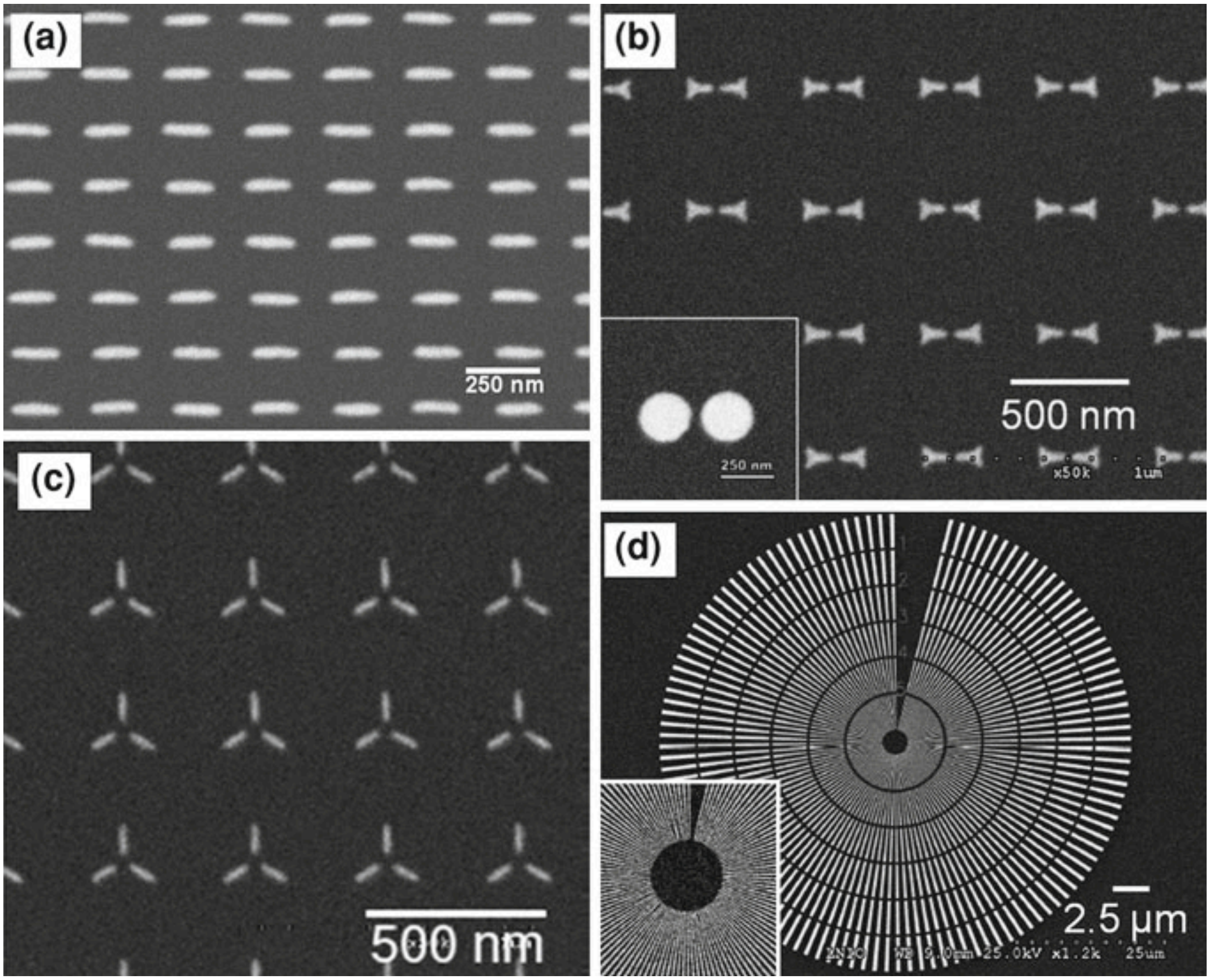

Figure 2.8 SEM images of plasmonic structures shape control fabricated by EBL: (a) ellipsoid, (b) dimers (spheres and bow-ties), (c) trimers, and (d) multiscale concentric structures.[165]

2.5.3 **Interferometric Lithography**

In conventional mask-based lithography, passing the light through a binary mask produces the intensity modulation.[166,167] In IL, optical intensity modulation is produced by causing two or more beams to interfere with each other. Interference is the superposition of electromagnetic waves in the same region of space and time, and IL as an enabling technology helps meet the increasing desire for smaller feature sizes in optical lithography.[168,169] Modern integrated circuits possess very regular layouts with an underlying grid patterns that describes the smallest feature size in each circuit. IL can support this by fabricating both periodic and quasi-periodic patterns that are spatially coherent over wide areas.[170] IL has also improved in the last decade, offering the advantages of simple optics, large working distances, fast processing, low cost, and high resolution.[171,172,173,174]

IL support a wide range of applications that including nanoscale epitaxial crystal growth, nanofluidic and nanobiological applications, nanomagnetics, and nanophotonics. To meet the demands of these applications. IL has been improved and extended over time through the use of multiple beams, multiple exposures and the integration IL with other lithography techniques. [168]

2.5.3.1 Two-Beam IL

In 1970, two-beam interference lithography was first used to generate one-dimensional gratings for use as optical couplers.[175] Two-beam interference lithography is also currently used to fabricate dense line or space nanostructures in the study of the chemistry and to support the performance of extreme-ultraviolet photoresists.[176] Two-beam interference can produce a 2D pattern through multiple exposures.[177,178,179] In practical terms, two beams interference is highly convenient in facilitating the use of a range of geometries to obtain a wide range of lattices with changeable unit sizes and large contrast.

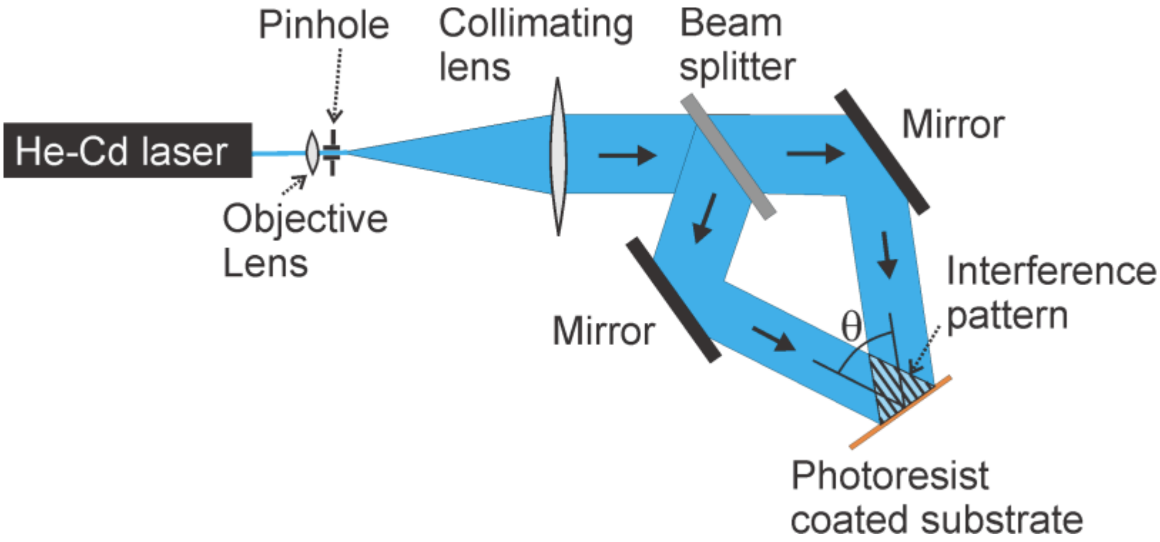

Figure 2.9 Schematic diagram of the basic principles of a Mach-Zehnder interferometer used for the recording of the periodic interference pattern on a photoresist-coated sample.[180]

The two-beam Mach-Zehnder interferometer used to record the interference pattern on a positive photoresist is depicted in figure 2.9. A beam from the 325 nm or 442 nm line of a He-Cd laser is transmitted through a pinhole and collimated. The beams are then split to create two-beam interference and may be achieved when two coherent optical plane waves with the same polarization are symmetrically incident on a sample at an angles of 2θ, as shown in Figure 2.9.[181] The period of the recorded interference pattern is given by the wavelength of the laser light used for the exposure, λ_{EXP} and the angle θ between the beams:

$$\mathbf{n = \lambda_{EXP}/ 2\sin\theta} \qquad \mathbf{2.14}$$

Figure 2.10 shows a Lloyd's mirror (Fresnel mirror) two-beam interferometer in which a flat mirror is fixed perpendicular (or at a set angle) to the sample stage. Half of a beam is pointed directly onto the sample surface on the stage, whereas another half of the beam is pointed onto the mirror, from which it is reflected onto the sample surface where it interfered with the other half of the beam to fabricate a sinusoidal pattern of intensity. This setup can produce quite successful patterns if it is used with a high transverse coherence laser beam such as single-mode TEM Ar-ion laser, as shown in figure 2.10.[168,182]

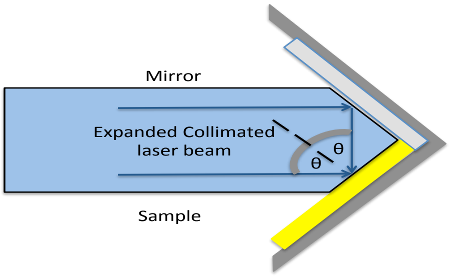

Figure 2.10 Schematic diagram of the two-beam interference apparatus for Interferometric Lithography.

The Lloyd's mirror interferometer is a simple two-beam IL setup that has been applied to fabricate a high-resolution nanostructure with half-pitches as small as 19 nm using extreme ultra-violet (EUV) on polymethyl methacrylate (PMMA) and several photoresist film.[183,184] The large number of transverse modes in excimer lasers means that they are not easily used for IL, leading to the use of gas lasers such as frequency doubled argon ion lasers may be used instead. These have higher transverse coherence and the beam quality may be further improved via the use of a spatial filter. However, some problems have been solved by building an interferometer setup where the beam is divided in half and folding it onto itself to control contrast. There persists the requirement of a vital longitudinal coherence, as the distances between the beam splitter and the sample are different for the two beams.

2.5.3.2 Immersion lithography

In 1884, the immersion technique was first explained by Carl Zeiss to raise the resolving power of the optical microscope. According to Rayleigh the resolution of an optical system is given by

$$R=\frac{0.61\,\lambda}{n\,sin\,\alpha} \qquad \textbf{2.15}$$

where λ is the wavelength and $n\ sin\ \alpha$ is the *numerical aperture* of the lens.

By working in a fluid with $n > 1$ it is possible to increase the numerical aperture and thus improve the resolution.[185,186] In the last two decades, increasing lenses have thus been increasingly used in the fabrication of integrated circuits. Several technical concerns delayed 57 nm lithography, thought since then development of 193 immersion lithography has proceeded at speed. This relies upon the replacement of the usual air gap between the last lens element and the photoresist surface with a liquid medium with a given refractive index. The resolution is then improved by a factor similar to the refractive index of the liquid. Immersion lithography tools employ highly purified water to access feature sizes below 37 nm. In term of the liquid used, a larger refractive index enables a higher resolution to be achieved.[187] Immersion lithography's evolution has led to the use of immersion fluids, topcoats, and novel photoresist components in order to better manage fluid-resist interactions and to reduce any possible lens contamination. Immersion lithography materials have thus evolved to support the use of pattern gratings with a 22-nm half pitch. This ultrahigh resolution was can be achieved by employing 157-nm light, a sapphire coupling prism with a refractive index of 2.09, and a 30-nm-thick immersion fluid with an index of 1.82.[188] Immersion IL has been used to fabricate nanostructures simply by utilising a Lloyd's mirror interferometer, which consists of a triangular prism with one metal-coated side that acts as a mirror. Using a laser with a wavelength of 244 nm and water as the immersion liquid has been used for pattern lines with a width of 45 nm.[189]

2.5.3.3 Multiple-Exposure IL

In 1993 Saleem and Brueck introduced multiple exposures interferometric lithography, facilitating an important extension to two-dimensional nanostructures.[190] Multiple exposure techniques are used to build high density gated field emitter arrays.[191,192] as well as large arrays of single domain Co dots to enable high density data storage.[193] Significantly, pairwise exposures have enabled maintenance of the effectively unlimited depth-of-field while still facilitating complex structures. Mixing and matching with conventional optical lithography affords additional flexibility, such as the fabrication of interdigitated structures suitable for high-speed photodetectors and conductive particle sensors.[194] Multiple-exposure IL applying Lloyd's mirror interferometer connected to a UV laser at 244 nm has also been employed to pattern SAMs of alkanethiolates on Au[177] and alkylphosphonate on titanium oxide[195] surfaces over large areas.[196]

A square array of posts can be created by first creating one exposure with a periodicity in the *x*-direction and then adding a second exposure with a periodicity along the *y*-direction. An experimental realisation of this approach using a negative SU-8 photoresist is shown in Figure 2.11.[197]

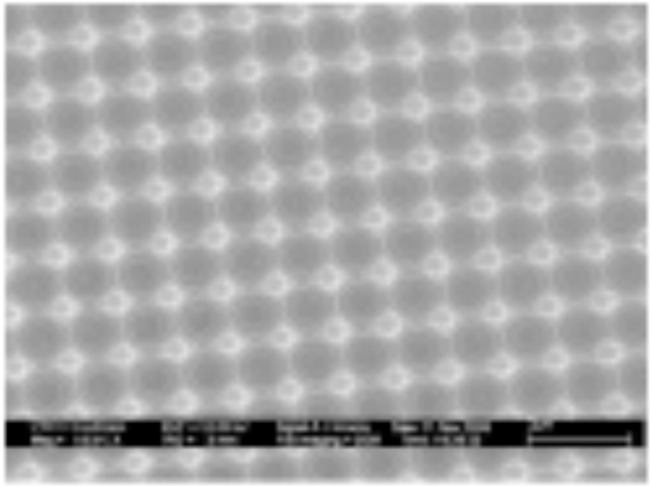

Figure 2.11 A SEM image of a pattern formed by double exposure in a negative SU-8 resist.[197]

For the majority of visible light wavelengths, aluminium is superior to other metals, including gold, silver, and copper, in relation to the distance it enables plasmons to travel. Paradoxically, the semiconductor industry recently stopped using aluminium for wiring, opting instead for copper as a more effective electrical conductor. However, some alloys exceed both aluminium and copper in terms of their plasmonic characteristics.

Moreover, chip manufacturers must continuously endeavour to safeguard their electronic chips from overheating, and whilst it is likely that plasmonic components will generate heat, the extent of the impact of this on device performance is currently hard to quantify. Even if plasmonics offer comparable levels of heat to electronics, it is likely that they will offer greater data capacity at the similar heat levels.[198]

Rapid progress is being made in the development of plasmonic components as they move from separate, inert constructs towards becoming incorporated, functional devices.[199] In terms of contemporary computational networks, these components could transform a range of bandwidth, speed, size, cost, and power needs, thereby facilitating more efficient and effectual solutions to the increasingly multifaceted issues being encountered.

The activity of plasmon waves on metals is comparable to that of light waves in glass, which means that multiplexing can be employed. Moreover, further developments in plasmon sources, detectors, wires, and splitters are all possible.[200,201] Generally, many applications rely on loss control, though the expense entailed in nanofabrication approaches is also a significant factor.

2.6 Self-assembled monolayers

The field of self-assembled monolayers (SAMs) has seen an enormous increase in synthetic sophistication and depth of characterisation in the last two decades.[202,203] Monolayer films can be made by using two different process. The first is the Langmuir–Blodgett technique, which involves the transfer of a film, pre-assembled at an air-water interface, to a solid substrate. The second, self-assembly, occurs naturally on immersion of a substrate into a solution containing a suitable amphiphile.[203] This latter approach, based on the existence of SAMs, has rapidly established itself as the method of choice in many situations, particularly for organosulfur compounds on noble metals. The fabrication and synthesis of SAMs are very well established in this area, supported by extensive characterisation using a combination of microscopy, spectroscopy, and physical-organic studies.

SAMs have been used widely to control the properties of plasmonic nanostructures, particularly to facilitate binding to an analyte. SAMs have also been used to increase resistance in the fabrication of metal nanostructures. Metallic (Au, Cu, Ag, Pd, Pt, and Hg) and semiconducting (Si, GaAs, ITO, etc.) surfaces can both be functionalised by the adsorption of organic molecules (both aliphatic and aromatic).[204] To form a SAM, a strong specific interaction between the head group of the adsorbate and the solid surface; then, by varying the properties of the tail group, it is possible to control the properties of the surface.

These SAM-modified surfaces are incredibly helpful for examining basic phenomena like adhesion, corrosion, distance-dependent electron transfer and single-electron transfer mechanism. These kinds of surfaces also make it possible to see molecular processes on artificially created nanostructures, such as Coulomb's staircase.[205] The high degree of order and compact packing of the adsorbates on metallic surfaces in SAMs are crucial for real-world uses such as patterning, semiconductor passivation, chemical sensing, and control of surface characteristics like wettability and friction.[206]

2.6.1 Concept of SAMs

Self-Assembled Monolayers (SAMs) are ordered assemblies of molecules or ligands produced by the adsorption of a surfactant from a solution or gas phase onto a solid surface.[199] The molecules that form SAMs on solid surfaces have chemical functional groups, or head-groups, that exhibit a strong affinity for that surface. Typically, the headgroups have such a high affinity for the surface that they displace adventitious organic materials;[207,208] while the tail groups are oriented towards the outside of the layer, and a spacer chain that links each head and the tail group. Figure 2.12 shows the process of preparation for SAMs.

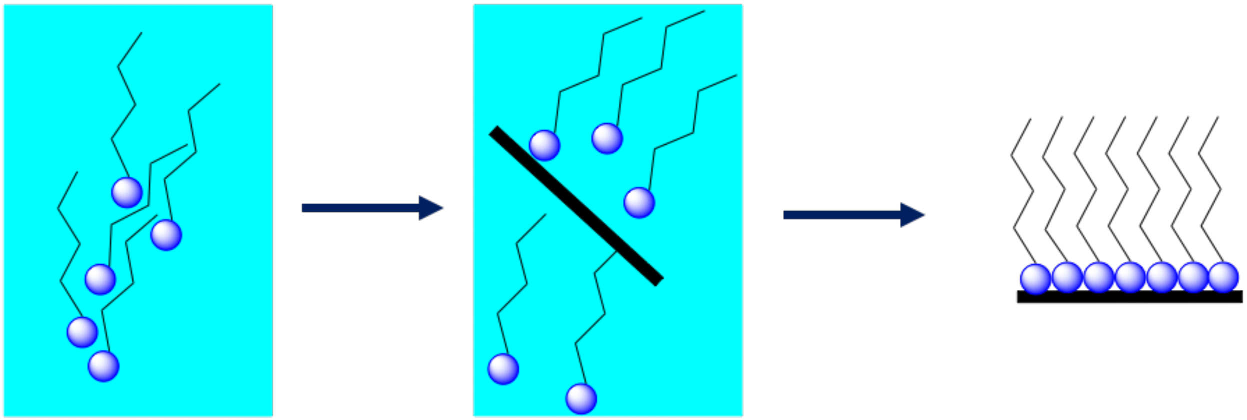

Figure 2.12 The process of preparation of self-assembled monolayers, which are formed by simply immersing a substrate into a solution of the surface-active material and allowing SAMs to form on the substrate.

2.6.1.1 SAMs of Alkanethiolates on Gold

A variety of different methods for the preparation of SAMs have been reported in the literature.[202,209,210,211] There are a broad range of adsorbates that exhibit a similar ability to couple to precious metals or metal oxides, forming close-packed, ordered films.[212,207] However, the most widely investigated class of SAMs is derived from the adsorption of thiol (-SH) molecules on noble metals and semiconductor surfaces. The properties and behavior of the SAM are affected by the way in which the headgroup interacts with the substrate, the nature of the tail group, and the length of the alkyl chain. As it is also possible to modify the tail group chemically, this offers greater flexibility. The thiol headgroup forms a strong interaction with noble metals leading to a well-defined organic surface with controllable chemical functionalities exhibited at the outer surface.[213,214] Figure 2.13 shows a schematic diagram of a SAM of organic molecules. SAMs are formed spontaneously by the adsorption of surfactants onto suitable substrates to yield close-packed, well-ordered assemblies. Gold substrates may consist of either nano- or micro-particulates in solution, and commonly they are made by thermally evaporating a thin adhesion layer of Cr, followed by Au onto a planar substrate.[215,216] Alkanethiols then bind to the Au substrate and are reduced to alkanethiolates.

$$\mathrm{RSH + Au\ (0) \rightarrow RS{-}Au(I) + {}^{1}\!/_{2}\ H_2}$$

Disulfides will also adsorb onto gold to form monolayers of alkylthiolates, via S-S bond cleavage.[217]

$$\mathrm{2Au + RS - SR \rightarrow 2Au - SR}$$

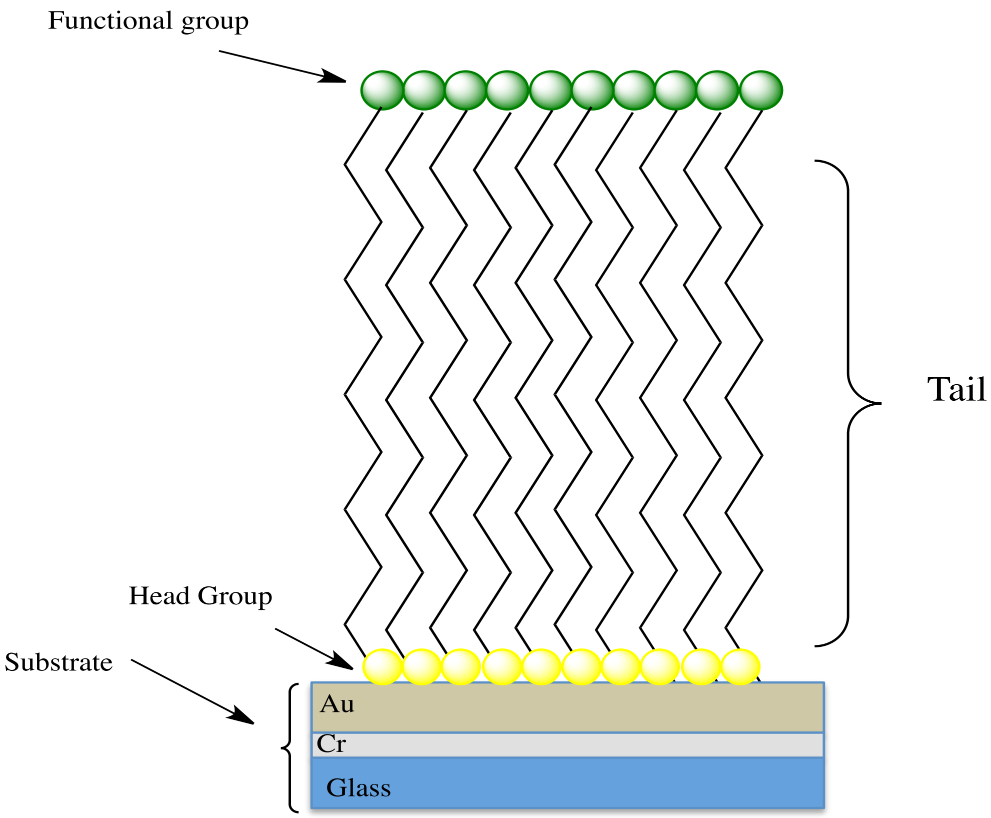

Figure 2.13 Schematic diagram of SAMs of alkanethiolates on gold.

2.7 Protein Immobilization techniques

Protein Immobilisation on a solid substrate is useful both for fundamental studies and for applications in devices such as biosensors.

There are various experimental strategies for this in biology that may be used in applications in diagnostics and drug discovery, leading to a wide range of strategies for immobilizing proteins on sensor surfaces.[218,219,220] The techniques can be divided into three main groups, depending on how the protein is bound to the surface.[221,222]

Physical immobilization that is driven by intermolecular forces (polar, hydrophobic or electrostatic) between the surface and the protein results from a weak attachment of ligands with a heterogenous distribution and random orientation.[223,224] Covalent immobilization, with surface-bound functional groups that react with exposed amino acid side chains on the protein surface is also possible. Coupling to amine and thiol groups is also commonly used,[225,226] and photochemical techniques have been used, including the use of photolabile agents that produce covalent bonds upon UV light activation.[227] Click chemistry, involving cycloaddition of an azide and an alkyne has also attracted interest in this regard. Additionally, bioaffinity immobilization approaches that depend on recombinant affinity tags, for example the naturally occurring biotin-avidin system, have also emerged.[228] Antibody immobilization can be used to selectively bind proteins from solution, while glycoproteins can be immobilised through the binding of their carbohydrate moieties to surface bound lectins. Hodneland et al. demonstrated that SAMs of alkanethiolates on gold enable selective and irreversible immobilization of proteins, a process achieved by utilising active site-directed ligands that first connect to an individual protein and subsequently react with that protein to form a covalent link.[229]

A diversity of techniques can thus be applied to the process of immobilising proteins. The common and extensively used processes depend on nonspecific adsorption of the protein to a solid support,[230] though covalent attachment is also regularly used. Both approaches require extremely pure proteins, yet they often lead to randomly oriented and partly denatured proteins.[231] The use of recombinant tags can facilitate proteins connecting to a substrate in a specific orientation, though the interactions of the tags can be reversible. Tags such as glutathione S-transferase, oligohistidine are thus unstable over the course of subsequent assays and therefore may need larger mediator proteins such as antigen-antibody or biotin-streptavidin.[232,233,234]

2.8 **Polymer brushes**

Polymer brushes are thin films that consist of polymer chains that are tethered to a surface. Polymer brushes began to attract attention in the 1950s when it was first noticed that flocculation could be restricted by grafting polymer molecules to colloidal particles.[235,236] Several of the first quantitative treatments of polymer brushes were described by Alexander,[237] de Gennes,[238] and Semenov,[239] leading to observations that where polymer chains tend to be adsorbed strongly on the surface the macromolecules typically will be a flat pancake at the surface as shown in figure 2.14(a).[240] When the distance between anchoring points is smaller than the radius of gyration of the polymer, and the interaction between the polymer and the substrate is weaker, however, the chain collapses to form a "mushroom" conformation, as shown in Figure 2.14(b). When the grafting density is higher, such that the separation between the grafted chains is smaller than the radius of gyration, steric repulsion between the grafted polymer molecules causes them to swell away from the surface generating the brush conformation as shown in Figure 2.14(c).

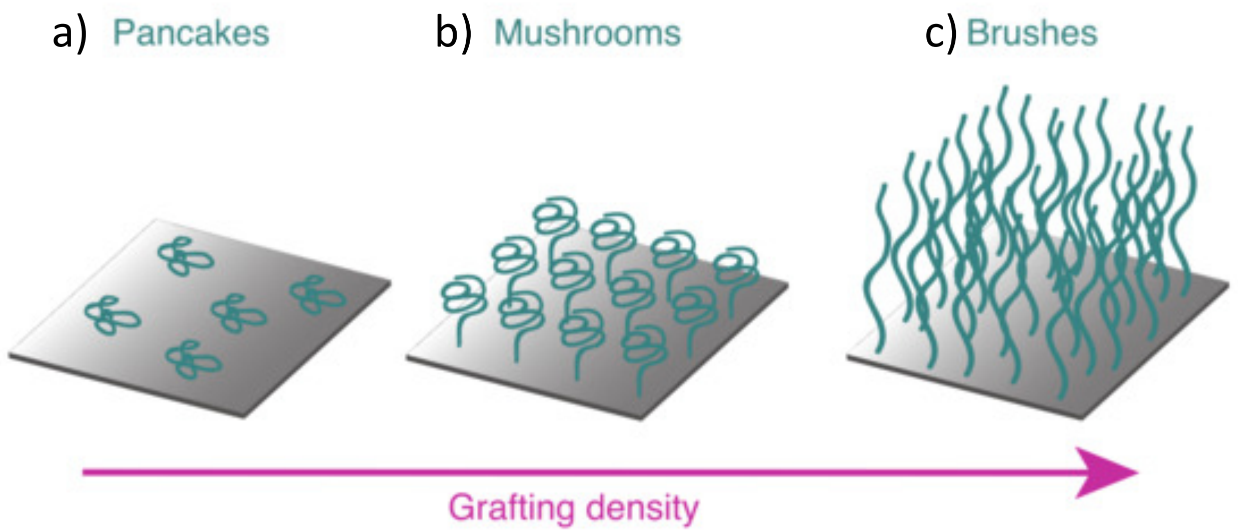

Figure 2.14 (a) The Pancake conformation of a polymer on the surface, (b) Mushroom conformation on the surface that attached polymer and (c)Brush conformation of a polymer on the surface and the arrow increasing grafting density.[240]

2.9 Types of Polymer Brushes

The two principal methods of tethering brushes covalently to a surface substrate are grafting from and grafting to.[241,242]

2.9.1 Grafting To

The grafting to technique applies a preformed polymer with a reactive end-group to add the polymer chain on the substrate (figure 1,12). The most widely used reactive functional groups are thiols, silanes, amino and carboxylic acid groups.[242,236] There are two major drawbacks to this process, however. The first is that the grafting to technique does not yield the highest possible density of polymer brushes due to steric repulsion between the grafted polymer chains and the incoming molecules.[243] As the coverage increases, the grafted chains inhibit access for the new polymer chains to the vacant grafting sites on the surface. Additionally, binding of the polymer to the surface is further inhibited where the molecular weight is large.[244] Figure 2.15 shows the grafting to method.

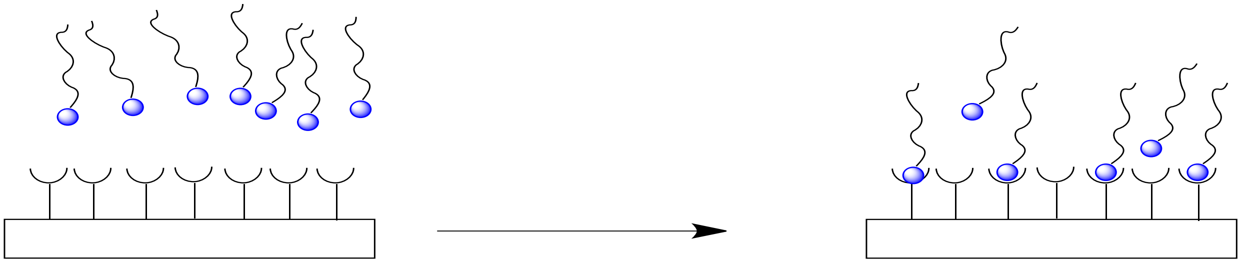

Figure 2.15 Schematic illustration of polymer brushes using the grafting to process.

2.9.2 Grafting From

The grafting technique has been applied by numerous researchers to apply thin polymer films to surfaces.[245,246] In surface-initiated polymerisation, the surface is functionalised with polymerisation initiators, as polymer chains will only grow from initiator sites.[247,248] Monomers at the surface can either add to a growing polymer or react with these initiator sites. Owing to the extremely small chains forming in the initial step and monomers being continuously added to the growing chains, polymer brushes with very high grafting densities can thus be synthesised without steric hindrance.[236] The polymer brushes created using this method are very uniform and dense. To address the limitations of the grafting technique, polymer brushes are commonly prepared using a "grafting from " technique, as shown in Figure2.16.

Whilst the Langmuir-Blodgett technique can be used to deposit a film on a surface, functionalisation is more commonly achieved by forming an initiator including a SAM.[249] The choice of the initiator is dictated by the polymerisation chemistry. Surface-initiated polymerisation is a versatile approach that allows grafted polymer films to be grown from a wide variety of surfaces. Atom-transfer radical polymerisation (ATRP), ionic, radical, ring-opening, and reversible addition–fragmentation chain transfer methods of polymerisation have all demonstrated their ability to form thick surface-initiated polymer films under well-controlled conditions.

For example, Sumerlin et al.[250] used this approach to apply pre-formed poly((ar-vinylbenzyl) trimethylammonium chloride), poly (N, N-dimethylacrylamide) and poly (sodium 4-styrenesulfonate) onto gold films.[251] Similarly, Tran and Auroy[160] used this technique to form dense poly (styrene sulfonate) terminated silane on silicon wafer. By grafting poly (ethylene glycol)-terminated silanes (PEG silanes) onto silicon surfaces, very smooth ultrathin films have also been produced.[222]

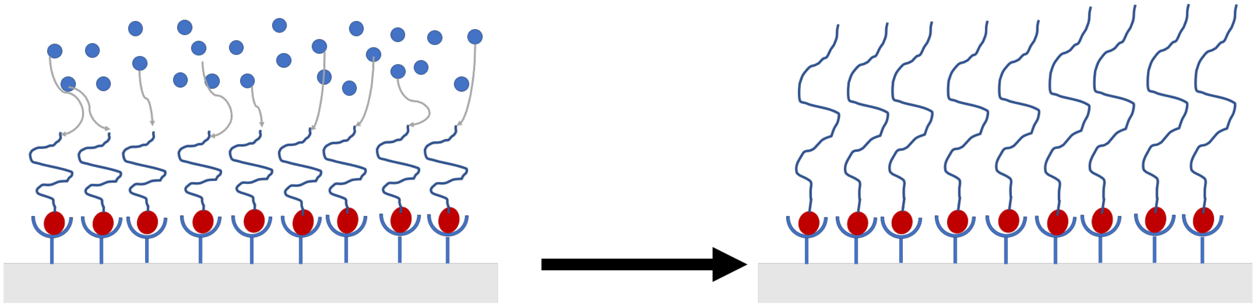

Figure 2.16 Schematic illustration of the grafting from process.

2.9.3 Atom transfer radical polymerization (ATRP)

Due to its ease and flexibility, atom transfer radical polymerisation (ATRP) offer a useful technique for polymerising a wide range of monomers under mild reaction conditions.[252] ATRP is a type of grafting mechanism that offers living radical polymerisation in which the initiator is transferred to the growing chain after each addition of a monomer; it thus confers excellent control of polymerisation. The technique, which was first described by Matyaszewski (1995),[253] relies on an atom (usually a halogen) being reversibly transferred between a propagating radical and a transition metal complex (usually Cu-based). The main value of ATRP is it facilitates the controlled growth of polymer chains. The catalytic method depends upon the L/CuI (L= Ligand) activation of halogen chain ends to generate radicals, which are then reversibly deactivated by means of a halogen atom transferred from an L/CuII-X deactivator (X = Br or Cl). Although the best characterised complexes are copper-based, and these have been widely and efficiently used in ATRP catalysis to polymerise diverse vinyl monomers,[254] other examples of transition metal-based catalysts have emerged, including complexes of iridium,[255] iron,[256] and ruthenium,[257] and organic-based photo-redox catalysts can also be used.[258] The putative mechanism behind ATRP is that, following reaction with Cu(I), the alkyl halides homolytically cleave the C-X bond to produce radicals. Alkyl halides are thus considered efficient initiators of ATRP, providing a straightforward method of synthesising well-defined alkyl end-functionalised polymers. Key ATRP parameters are the exchange dynamics and the rate of deactivation. Where the deactivation process is slower than the propagation process, the system switches to a classic redox initiation process, where radical polymerisation is not controlled, however.

ATRP is a particularly attractive option as it enables polymerisation in aqueous solutions at room temperature.[259] The yield of a broad range of monomers is high, and as any radical species are always at the growing end of the surface-tethered polymer chains, few transfer reactions emerge. The ATRP technique thus offers several benefits.[260,261] These include using catalytic amounts of transition metal complexes; the availability of a broad range of commercially available initiators that include hybrid and multifunctional systems; the ability to use it over a wide range of temperatures; and the fact that ATRP auto-acceleration is not generally a problem due to the localised increases in the viscosity of the polymerising system that slow termination reactions. Further, except for unprotected acids, an extensive assortment of monomers can be polymerised, and, unlike other controlled radical polymerisation (CRP) methods, achieving block copolymerisation is not dependent on order with halogen exchange, making end-functionalization straightforward. However, acidic monomers require protection, and the need to remove the transition metal complex from the product in most cases is a limitation of the ATRP method.

Novel (co)polymers synthesised using ATRP have precisely controlled compositions (block, alternating gradient, graft copolymers) and molecular weights, as well as relatively low dispersity (Mw/Mn < 1.1) and diverse functionalities.[262] Figure 2.17 demonstrates how state of equilibrium is maintained in ATRP between the propagating radicals and dormant species, which is achieved primarily by initiating alkyl halides and macromolecular species (Pn-X).[252,263] Intermittent reactions between the dormant species and transition metal complexes in their lower oxidation state, M_t^n/L, generate radicals (where L is a ligand, and M_t^n is the transition metal species in oxidation state, m). Each radical propagates the vinyl monomer (k_p), though it may be reversibly deactivated or terminated, either by coupling or disproportionation.[195, 196]

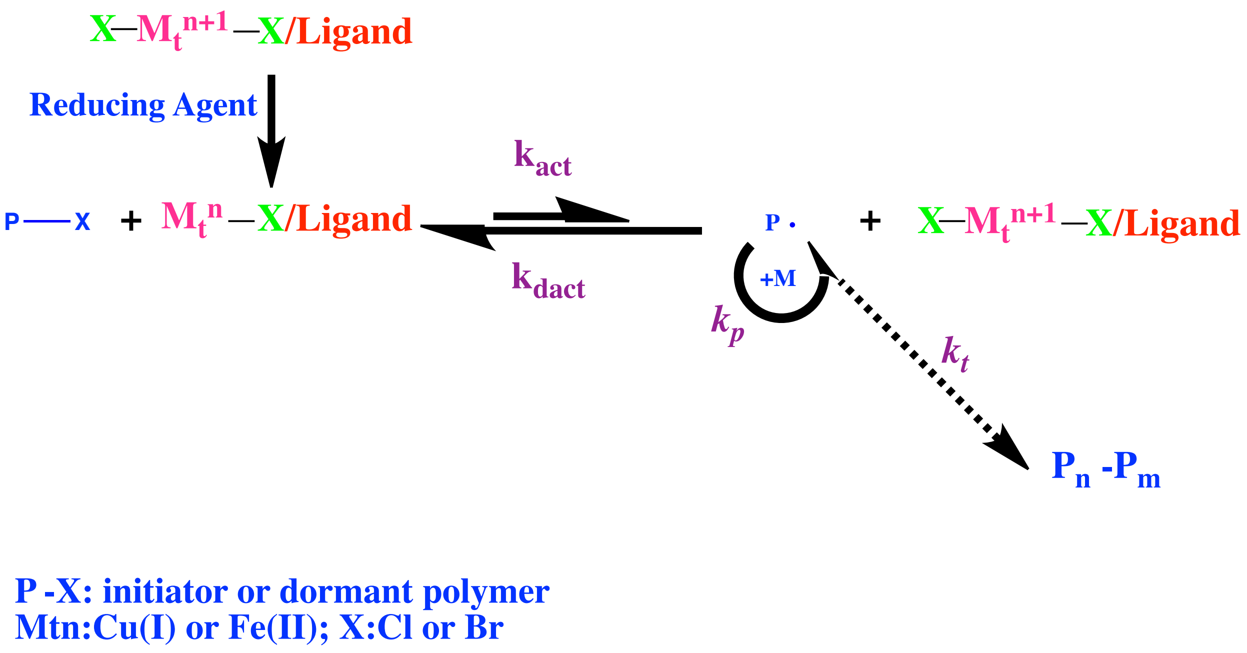

Figure 2.17 Kinetic mechanism of ARGET ATRP technique

Due to a continuing radical effect, the concentration of radicals is reduced in ATRP, enabling the preparation of well-defined polymers. As a catalytic process, numerous redox-active transition metal complexes can modulate ATRP; the most common is the Cu found in CuI/L and X-CuII/L complexes.[264,265]

In AGET ATRP, the activators are generated by electron transfer without the direct involvement of any organic radicals capable of initiating a radical reaction or forming molecules to act as initiators. An additional requirement for a successful AGET ATRP is thus that the reducing agents should be selected so that reduction occurs without forming intermediates or products that might form new initiators for ATRP. Some reducing agents can also react directly with alkyl halides; however, any exchange reactions must then be faster to control polymerisation. A further benefit of AGET is that the reducing agent can remove any dissolved oxygen in the system, allowing the reaction to be conducted in the presence of a limited amount of air.[266,267] AGET ATRP is a technique in which the activators regenerate, allowing, for example, a small amount of copper (II) deactivators to be continuously regenerated into copper (I) activators by the reducing agents.

Many types of reducing agent have been used in AGET-ATRP but the most widely used are ascorbic acid, Cu, glucose, and tin (II) 2-ethylhexanoate. In some studies, hydrophilic macromolecular initiators have been used to synthesise amphiphilic block copolymers, and, in order to generate fewer rigid conditions for initiating polymerisation, a reducing agent can be used. This also improves tolerance to oxygen.

AGET ATRP uses much lower copper catalyst concentrations than conventional ATRP.[268] Its other significant advantage over conventional ATRP is that it can largely reduce side reactions between the metal/ligand catalyst complex, thus achieving higher levels of monomer conversion and retaining chain-end functionality, which in turn improves crossover.[269] In turn, this facilitates the preparation of copolymers with higher molecular weight. Additionally, the lower the concentration of the copper catalyst, the less likely side reactions and termination events are to occur, which further improves control over polymerisation. When combined, these features make ARGET ATRP an appealing and effort method for preparing polyampholyte brushes, particularly those grown on surfaces with low numbers of active chain ends as a result of chain surface densities that are typically in the order of 10^{15} or 10^{16} chains per m^2 (ch m^{-2}).[270] Furthermore, AGET ATRP facilitates higher control in polymerisation when amine-containing monomers are used, offering a number of benefits in terms of copolymerisation. For example, it allows for control over the composition of the polymers, as well as the smooth incorporation of comonomers.

The mechanism behind ATRP is the creation of a metal halide complex by means of a transition metal complex (M_t^nLm) cleaving an alkyl halide bond (R-X). R-X is an adsorbate that forms from the reaction of cysteine bromide with an amino propyl triethoxysilane film.[257] The products are an alkyl radical (R.) and a complex with a higher oxidation state ($M_t^{n+1}LmX$); R. is then added to a monomer (M). This process requires the active propagating radicals from the initiator to be in equilibrium with the deactivated dormant tend of the polymer chain. The radicals added to the monomer are then terminated by connection or by disproportionation, as shown in figure 2.18. The minimal concentration of propagating radicals and minimised probability of termination occur due to the equilibrium between the active and the dormant chains to the left.

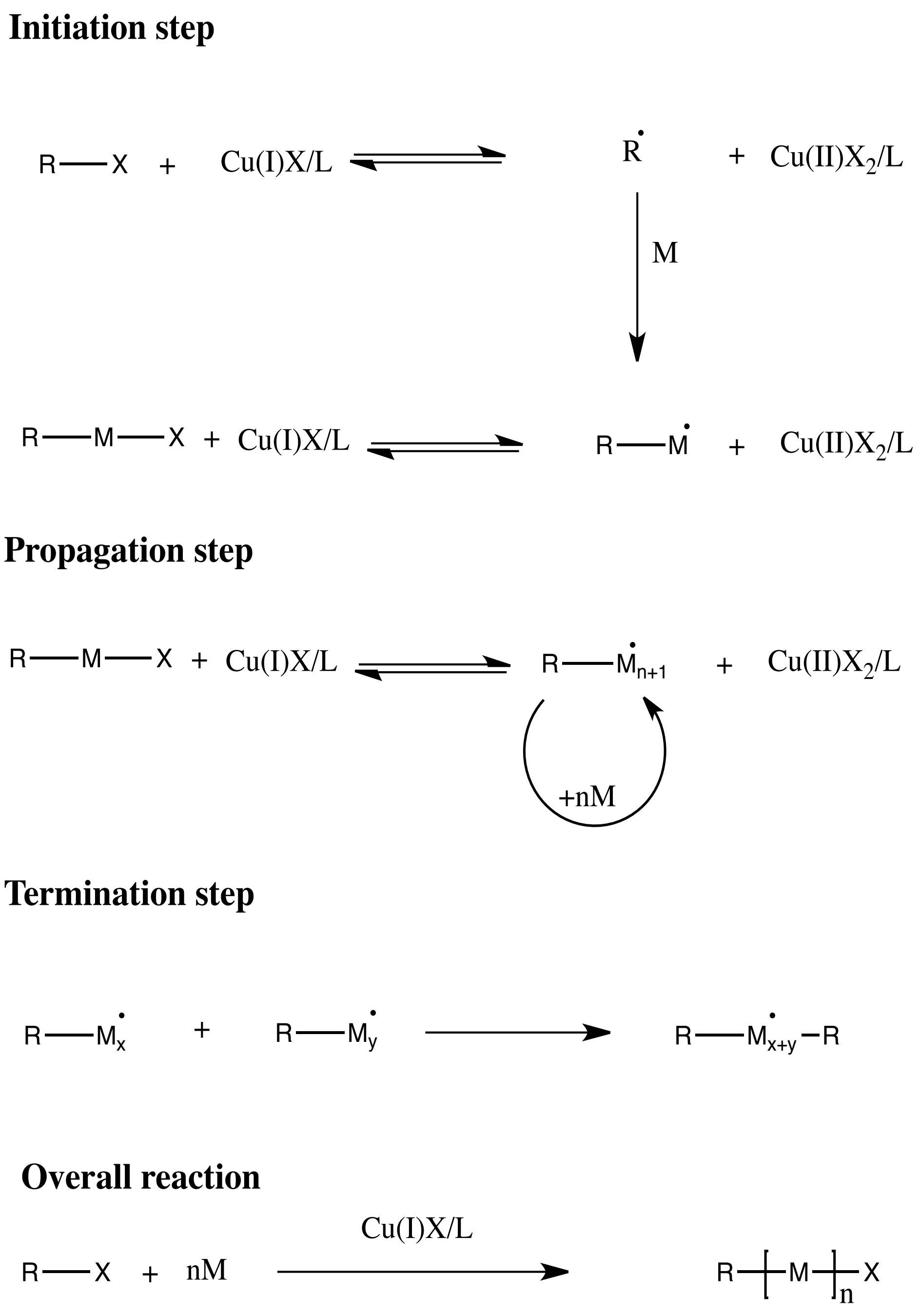

Figure 2.18 The mechanism of ATRP according to Matyjaszewski et.al[271] as a tool for surface functionalisation. In the initiation step, the radical ($R^{\bullet}$) is generated from the alkyl halide of the initiator; this then it reacts with a monomer, forming the radical monomer. The monomer is added to the intermediate polymer radical in the propagation step.

There are multiple factors that influence the kinetics of ATRP. These include the initiators, the monomers, the solvent, and the duration and temperature of the process, as well as the ligands integrated into the transition metals involved.[259] Various vinyl monomers have thus been polymerised using the ATRP method. Propagating radicals can be stabilised by the substituents in acrylonitrile, (meth)acrylamides, (meth)acrylates and styrene, making these particularly suitable for use in ATRP. As the atom transfer equilibrium constant of both the active and deactivated species is unique to each monomer, even when using the same catalyst under the same conditions, each species of monomer has particular requirements for ATRP, however,[263,264] and when equilibrium constants are low, ATRP occurs very slowly, if at all. Equally, an excessive equilibrium constant causes an excessive concentration of radical, which leads to increased termination. To address this issue with large volumes of deactivated species, metal complexes with high oxidation states are used, which shifts the equilibrium toward the dormant species. However, this slows the rate of polymerisation.

Every monomer species has a distinctive propagation rate constant. Controlling polymerisation of each monomer thus required the concentration of propagating radicals and their deactivation rate to be modified. Altering the amount and reactivity of the catalyst then modulates the equilibrium position.

Typically, ATRP initiators are alkyl halides (R-X),[257] and using an appropriate halide (X), allows well-defined, narrowly distributed molecular weight polymers to be generated. The halide migration between the transition metal complex and the growing chains must be rapid, and controlling polymer molecular weight is best achieved with bromine or chlorine, which work as highly reactive and efficient catalysts for ATRP. Iodine may also be used to polymerise acrylate in copper-mediated ATRP, and in combination with rhenium or ruthenium catalysts, iodine can also be used in polystyrene preparation. Fluorine is not suitable for ATRP, however, as the strength of its bonding to carbon is too great to enable haemolytic cleavage. The dormant polymers and the alkyl (R) group of the initiator should also have comparable structures. For the synthesis of acrylonitrile chain ends, α-halopropionitriles are particularly useful, and 1-phenylethyl halides are most appropriate for polystyrene. Polymerisation of methacrylate is often achieved using isobutyrates. Almost any alkyl halide with activating substituents on the α-carbon (e.g. allyl, aryl or carbonyl groups can thus be used as an ATRP initiator, while compounds with a weak R-X bond, such as N-X, S-X and O-X, and polyhalogenated compounds (e.g. CCl_4 and $CHCl_3$) can also be used.[254,257]

As catalysts regulate the atom transfer equilibrium or exchange between the dormant and active species, a catalyst is a key component of ATRP preparation. ATRP catalysis generally involves a transition metal and ligands. However, although the concentration of catalyst determines the polymerisation rate, it does not influence the polymer's molecular weight. For transition metal catalysts to be effective, numerous factors thus need to be considered:

1) The presence of no less than two accessible oxidation states separated by one electron.

2) The metal-ligand bonds must be relatively strong.

3) The metal centre should form bonds with halogen atoms.

4) The catalytic metal centre cannot be a strong Lewis acid, as otherwise the ionization of certain initiators/end groups to carbocations may occur.[254]

5) Upon oxidation, the coordination sphere surrounding the metal centre must be flexible enough to contain the halogen atom.[262]

Co, Cu, Fe, Hf, Mo, Ni, Os, Pd, Re, Rf, Rh, Ru, Ti, and Zr are all transition metals that can be used as ATRP catalytic complexes, [196,200,201] though the most efficient catalysts are copper halides. Ligands are key components that are frequently central to catalyst solubility, while in the M_t^n/M_t^{n+1} cycle, they tune the redox potential. Typically, electron-donating ligands increase the polymerisation rate by stabilising the higher oxidation state of the metal centre. Frequently, ligands contain a nitrogen atom, and they are commonly combined with Cu and multidentate ligands, including derivatives of bidentate bipyridine (bpy), terpyridine(tpy), phenanthroline (phen), and tridentate diethylenetriamine (DETA).[263] ATRP reactions thus often use a ligand of 2, 2'bipyridine and a CuCl or CuBr catalyst.[259]

Non-polar solvents such as diphenyl ether, p-dimethoxybenzene or p-xylene are common polymerisation media. However, specific polar solvents for different monomers have also demonstrated effectiveness. Amongst these are acetone, alcohol, dimethylformamide (DMF), ethyl acetate, ethylene carbonate, toluene and water.[264] One advantage of polar solvents for ATRP is that they hasten the rate of polymerisation. The choice of solvent must, however, be informed by multiple considerations, such as the catalyst complex and solvent interactions. The solvent and solvent-assisted side reactions should not poison the catalyst, nor should the ATRP reaction suffer due to solvent modification of the catalyst's structure. Polymer chain transfer to solvent should also be low, though side reactions might occur in some solvents; for example, in polar solvents at 110 to 130 °C, polystyryl halide end groups can remove HX.[264]

2.9.4 Stimulus-responsive polymer brushes

The conformation of polymer brushes is extremely dependent on the solvent

used. If the solvent is good, this will lead to the polymer chains maximising the polymer/solvent contacts. Allowing them to swell: complete wetting is expected in this case.[236] However, if the brush is poorly solvated, it will collapse to reduce polymer/solvent interactions, as shown in figure 2.19. The features of stimuli-responsive binary polymer brush layers can thus be employed to produce switchable surfaces. The characteristics of these polymer brushes are strongly influenced by their surroundings, including the nature of the solvent-polymer interactions, leading to changes in the degree of solvation and thus to changes to the degree of swelling of the surface grafted polymer; the pH may also change, via changes in the charge density of polyionic brushes leading to electrostatic interactions between neighbouring chains; while the temperature also causes changes in the solvation and hence the swelling of polymers.

In the crowded grafted layers of polymer brushes, chains swell out of the grafting surface into the excluded volume. The impact of this is compensated for by the elastic energy (stretching entropy) of the polymer coils. The difference in feature size between good and poor solvents is thus more significant for polymer brushes as opposed to the polymer chain in solution.[236] For a homopolymer, the difference can be impacted by the grafting density of the brush. For example, in response to low grafting density (e.g., mushroom), brushes' responses are equal to those of a coiled polymer in solution. In contrast, the responses for high-density brushes in a poor solvent are weak due to their very crowded chains. Copolymer brushes are, however, commonly more complex than homo-polymers in terms of their response. Thus, a solvent may be a suitable solvent for one co-monomer while being a poor solvent for another, based on the nature of these individual components.

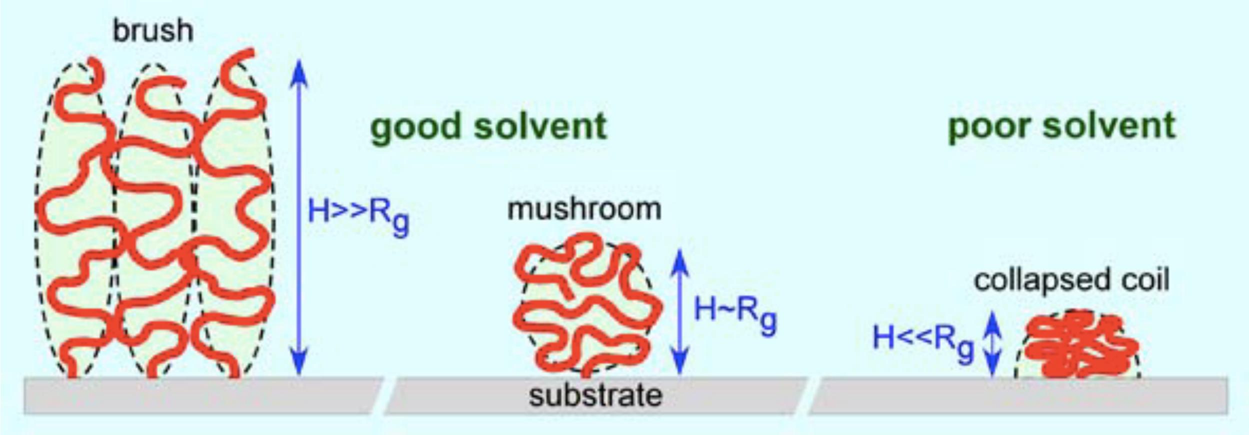

Figure 2.19 Schematic diagram showing how changes in solvent interactions lead to changes in the conformation of a stimulus-responsive polymer. In a good solvent, surface-anchored polymers adopt a brush (left) and mushroom (middle) conformations in good solvents. However, in a poor solvent, a surface-tethered polymer is fully collapsed (right).[272] Here, R_g is the radius of gyration of a polymer, and H is the wet thickness of surface-anchored polymer.

2.9.5 Ion and pH responsive polymer brushes

As well utilising useful neutral brush properties, a wealth of behavioural regimes can be generated by electrostatic interactions induced using a polymer brush formed from strong or weak polyelectrolyte molecules. Using pH and temperature responsive polymers to make brushes has thus become a recent focus of research, with the aim being to devise physiochemical responsive or smart interfaces to be used in actuator and sensor applications, as well as controlling wetting properties.[273] This latter point is essential in applications that involve the interfacial wetting of nanoparticles for the stabilisation of Pickering emulsions of immiscible liquids. The degree of dissociation of the chains in weak polyelectrolyte (PE) or annealed brushes can be modulated by varying the pH and ionic strength, offering a further parameter to be used to tune conformation of polymer reversibly. The degree of dissociation in strong PE brushes is independent of ionic strength and pH, however; such brushes are known as quenched brushes.[274]

Many people have used polymer brushes to study response to pH. Klinghammer et al.[275] found that polymer brushes offer a good complement to SiNW-based FETs, as the actual FET response is stable despite a biocompatible surface being formed. They also found that the large reversibility of swelling properties promotes high tunability of these systems, lending itself to the application of brushes as sensors. Mitsuishi et al.[276] discussed the formation of hybrid nanoassemblies with polymer brushes and gold nanoparticles to allow the detection of nanoscale optical changes based on localised surface plasmon resonance. They found that the actuation of reversible and thermosensitive nanoscale effects was triggered by coupling stimuli-responsive polymer brushes and gold nanoparticles separately and selectively assembling these on substrates. Mitsuishi et al. also revealed that using SPR technique helps support the hydration transitions of such thermoresponsive polymer brushes as grafted to gold surfaces: SPR measurements revealed that the PNIPAAm brush collapses over a temperature range of ∼10−40 °C.

2.10 The objectives of the thesis

Plasmonics is a fast-growing field based around light-matter interactions that provides the basis for new kinds of biological and medical sensors. For many sensor formats, nanoparticles supported on a solid phase are required. Also, existing nanofabrication methods tend either to be very simple (e.g. colloidal lithography) or very expensive (e-beam lithography). The goal of this project is thus to find a fast, flexible method for the fabrication of arrays of gold nanostructures on solid surfaces that are suitable for integration into sensors. These were tested on various biological molecules, such as streptavidin, synthetic maquette light-harvesting proteins, and polycysteine methacrylate (PCysMA). Also, polymer brushes are useful for modification of the nanoparticle surface (PCysMA is fouling resistant to the adsorption of proteins and cells). Some brushes are smart (stimulus-responsive) and it might be useful to detect this behavior. The hypothesis is that changes in conformation due to the response of a stimulus-responsive polymer to its environment may yield a change in the position of the plasmon band, enabling the conformational change to be tracked in situ using a simple optical measurement. The surface grafted polymers grow from nanostructures by studying brushes on gold nanoparticles. The conformations of polymers grown from nanostructures were studied by using AFM to measure the effects of brush-functionalised nanoparticles.

3. Experimental

The principle aim of this thesis was to develop interferometric lithography as a technique for the production of gold nanostructure arrays. The methods used to produce self-assembled monolayer resists are described. The apparatus used for photopatterning and, in particular for interferometric lithography is described. The characterisation of the arrays and of their plasmonic properties is described in sections 3.7. To test the utility of the resulting nanostructures, arrays were functionalism by the binding of proteins, as described in sections 3.8. Novel pH sensors were produced by functionalising gold nanostructure arrays with poly (cysteine methacrylate) brushes. The synthesis of the monomer is described in section 3.9, and the characterisation of the brush-functionalised arrays is described in section 3.7.

3.1 Materials

Microscope coverslip glass slides (22 mm × 50mm, #1.5 thickness) were obtained from (Menzel-Gläser, Germany). Gold wire (>99%) was procured from Goodfellow Metals (Cambridge, UK) and chromium chips (99.5% trace metals basis) were purchased from Agar (Cambridge, UK).

OTESPA-R3 tapping probes (Bruker, Germany) with a resonance frequency of ca. 300 kHz and a nominal tip radius of 7 nm as well as DNP-10 silicon nitride (Si_3N_4) contact mode probes with spring constants 0.06 N m^{-1} and 0.12 N m^{-1} (Bruker, Germany) were used in this study.

Chemicals used as received in this project are listed in Table 3.1.

Table 3.1 Chemical compounds that were used in the present research.

Compound	***Purity***	***Supplier***
Hydrogen peroxide	30%	Fisher Scientific
Sulfuric acid	99%	Fisher Scientific
n- Octadecanethiol	98%	Sigma-Aldrich
Ethanol	HPLC grade	Fisher Scientific
Ammonia	35%	Fisher Scientific
Cysteamine	99%	Sigma-Aldrich
Dichloromethane (DCM)	HPLC grade	Fisher Scientific
Triethylamine	98%	Sigma-Aldrich
Bromoisobutyryl bromide (BIBB)	98%	Sigma-Aldrich
Copper (II) bromide	≥99%	Sigma-Aldrich
3-Aminopropyltriethoxysilane (APTES)	98%	Sigma-Aldrich
2, 2’-bipyridyl	99%	Sigma-Aldrich
Ascorbic acid	99%	Sigma-Aldrich
Sodium hydroxide	≥ 98 %	Fisher Scientific
3-(Acryloyloxy)-2-hydroxypropyl methacrylate	99%	Sigma-Aldrich
Dimethylphenyl phosphine	99%	Agar Scientific
Streptavidin	-	Sigma-Aldrich
L-cysteine	98%	Sigma-Aldrich
Ethyl acetate	HPLC grade	Fisher Scientific
IHC Select Secondary Goat Anti-Mouse IgG Antibody	-	Sigma-Aldrich

3.2 Instrumentation

Coherent Innova 300C FreD frequency-doubled argon ion laser (Coherent FreD 300C, Coherent U.K., Ely, emitting at 244 nm) was used as a light source to create micro- and nano- scale patterns on SAMs. The essential emission wavelength of this laser is 488 nm and the UV wavelengths (244 nm) are acquired after doubling the frequency of using a Brewster-cut beta-barium borate crystal. Atomic force microscopy images were acquired using a Multimode V atomic force microscope (AFM) (Digital Instruments, UK). In tapping mode OTESPA-R3 silicon probes were used at a scan rate of 1.5 Hz, and the lines per image were 512. Friction-force images were using DNP-10 silicon nitride probes.

Cary-50 UV-visible spectrophotometer (Agilent Technologies, USA) was used to collect absorption spectra of plasmonic arrays of gold nanostructures. UV-visible absorption spectra at normal incidence were recorded in both air and liquids using a Cary50 spectrophotometer (Agilent Technologies, USA). The wavelength scan range was 480 – 900 nm (unless otherwise stated). The samples were fixed in a home-made PTFE holder enabling absorption measurements of the same spot on the sample during all experimental stages. During the measurements in liquid, the holder with a sample was placed in a standard quartz cuvette (10 mm transmitted path length).

The M-2000 spectroscopic ellipsometer (J. A. Woollam, USA) was exploited to measure the relative amplitude ratio of reductions after reflection, $\Psi(\lambda)$ and the relative phase shift, $\Delta(\lambda)$, of the thin films investigated in this work. Ellipsometric $\Psi(\lambda)$ and $\Delta(\lambda)$ spectra of continuous Cr/Au thin films functionalized with SAMs, SAMs + proteins and grafted with PCysMA brushes were collected with an Alpha-SE (J. A. Woollam Co., Inc., USA) ellipsometer operating in a spectral range of 370-1000 nm at the incident angle of 75°. All data were acquired and modelled using CompleteEASE (v.6.6) software. The oval-shape beam was in the size of the ca. 1.46 x 0.35 cm. Measurements were carried out in the air and each sample was measured at 3 locations to obtain an average.

3.3 Cleaning Glassware

All glassware was cleaned by washing them with water and sodium lauryl sulfate (SDS) followed by immersion in Piranha solution (a mixture of 30% hydrogen peroxide, H_2O_2 and concentrated sulfuric acid, H_2SO_4 (95%) in the ratio 3:7. Samples were immersed until the solution stopped bubbling, and allowed to cool to room temperature (caution: Piranha solution is a very strong oxidizing agent that may explode on contact with organic material), before being rinsed with copious amount of deionized (DI) water, sonicated for 5 min and finally, dried at 90 ^{o}C in an oven.

3.4 Sample handling

All instruments, i.e., tweezers, metal ruler, glass-cutter, samples, etc. used were rinsed with ethanol and dried under nitrogen to minimize surface contamination.

3.5 Preparation of self-assembled monolayer (SAMs) resists.

SAMs are layers of molecules that stick together on a surface, usually from a solution. A specific functional group that has a strong attraction to a particular surface makes their creation possible. SAMs are a cheap and flexible surface coating that can be used to control wetting and adhesion, chemical resistance, biocompatibility, sensitization, and molecular recognition for sensors and nanofabrication. Metal coated glass slides were immersed in 1 mmol solutions of n-octadecanethiol in degassed ethanol immediately after removal from the evaporation and immersed for at least 24 hours to form close-packed self-assembled monolayers.

3.6 Photopatterning of SAMs resist.

3.6.1 Micron-scale patterning

Micro scale patterning of SAMs was done by using a Coherent Innova 300C FreD argon ion laser (Coherent, UK). Samples were cut to 5x5 mm^2.

The micropatterning set-up (as shown in Figure 3.1) consists of a beam collimator, sample stage, and a periscope mirror at 45° to the incident beam. The laser spot had a diameter of approximately 5mm measured at the sample surface. A copper grid (2000 and 1500 mesh, Agar, UK) was employed as a mask. The grid consisted of a pattern of orthogonal bars (masked) that defined square regions that were exposed to UV light.[277,278] The mesh grid was placed on the sample, and a clean quartz disc was placed on top of it to hold it in position during exposure.

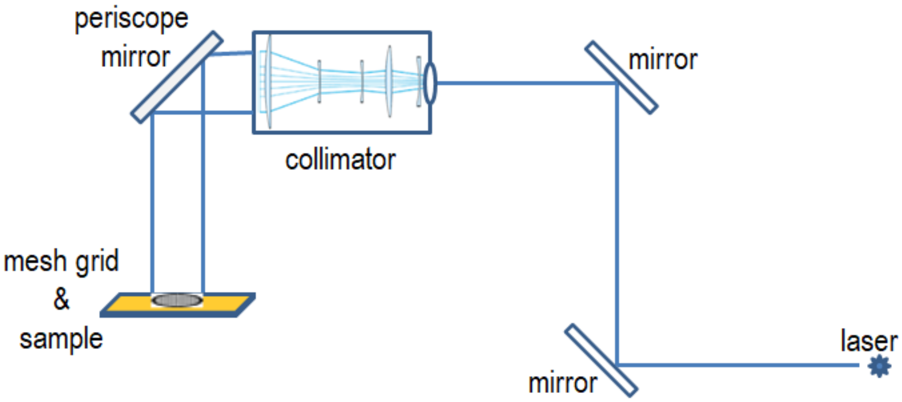

Figure 3.1 Schematic diagram of a micro-patterning set-up.

3.6.2 Nano-scale lithography

Interferometric lithography is a technique used to fabricate large-area arrays of nanosturctures.[279] A pattern is formed when two coherent beams interfere to generate a sinusoidal pattern of intensity with a period given by:

$$\text{period} = (\lambda/2) / \sin\theta \quad 3.1$$

Where λ is wavelength (244 nm, θ is the angle between the sample and the incident beam.

SAMs of octadecanethiol on gold were photo-patterned by interferometric lithography (IL) using a Lloyd's mirror two-beam interferometer (as shown in Figure 3.2) where half of the coherent beam is pointed directly onto the sample surface, and the other half of the beam is pointed onto a mirror, from which it is reflected onto the sample surface where it interferes with the other half of the beam to yield a sinusoidal pattern.

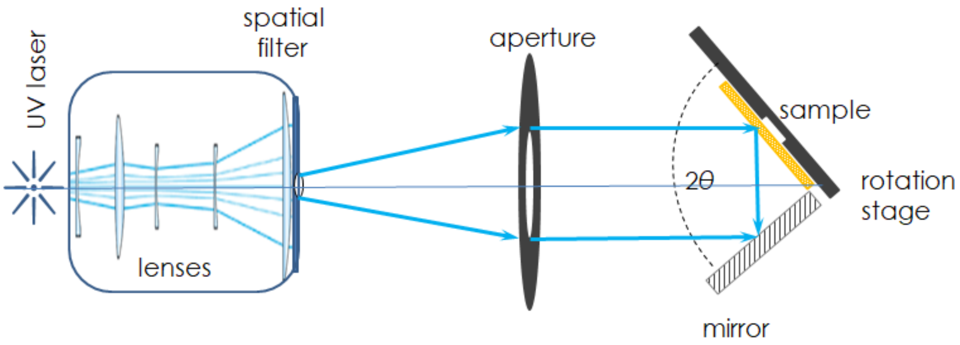

Figure 3.2 Schematic diagram of a Lloyd's mirror two-beam interferometer set-up.

The light source used was a Coherent Innova 300C FreD frequency-doubled argon ion laser is UV light at 244nm. Detailed description of nanofabrication routine is given in the chapter 4.

3.7 Characterisation of films and nanostructures by (a) contact angle measurement (b) XPS (c) AFM (d) UV-vis (e) spectroscopic ellipsometry)

Thin chromium/gold films were deposited on the clean and dry microscope coverslip slides in a diffusion pumped Edwards 306 thermal evaporator, with a bell jar evaporation chamber and a piezoelectric film-thickness control monitor. It involves of vaporizing a solid material (pure metal) by heating it to appropriately high temperatures and recondensing the material onto a cooler substrate to form a thin film. The heating is acquired by passing a large current through a filament container (tungsten boat or material coated tungsten rod). Cleaned glass slides were coated with two metals: chromium (or titanium) primer layer ca.5 nm thick followed by a 15 to 25 nm thick gold film. Both metals were deposited using an Edwards 306 thermal evaporator coater system, with a base pressure of $5 \cdot 10^{-6}$ mbar and a deposition rate of ca. 0.1 nm s^{-1}

Contact angle measurement, spectroscopic ellipsometry (SE), atomic force microscopy (AFM), and X-ray photoelectron spectroscopy (XPS) were used to analyze the chemical and physical properties of the thin films.

3.7.1 Contact Angle Measurements

The contact angle can be determined by calculating the relationship between the surface tension of the liquid and the perimeter of the sample. The measurement of the advancing angle occurs during the immersion of the sample into the liquid, while the measurement of the retreating angle occurs when the sample is withdrawn from the liquid. Contact angles were measured using the sessile-drop method.[280] A drop of liquid is placed on the surface and allowed to spread while being observed through a telescope. The contact angle at the solid-liquid-vapor interface is measured using a goniometer scale.

At the perimeter of the drop, the solid, liquid and vapour phases are in equilibrium, as shown in Figure 3.3. The free energy changes as a result of the spreading of the drop on the solid surface.[281,282,283]

The equilibrium is described by Young's equation:

$$\gamma_{sl} + \gamma_{lv} \cos \theta_o = \gamma_{sv} \qquad 3.2$$

where is the contact angle (the angle between the surface and a tangent to the drop surface at the three phase-boundary, and γ_{sl}, γ_{lv} and γ_{sv} are, respectively, the interfacial free energies for the solid-liquid, liquid-vapour, and solid-vapour interface.

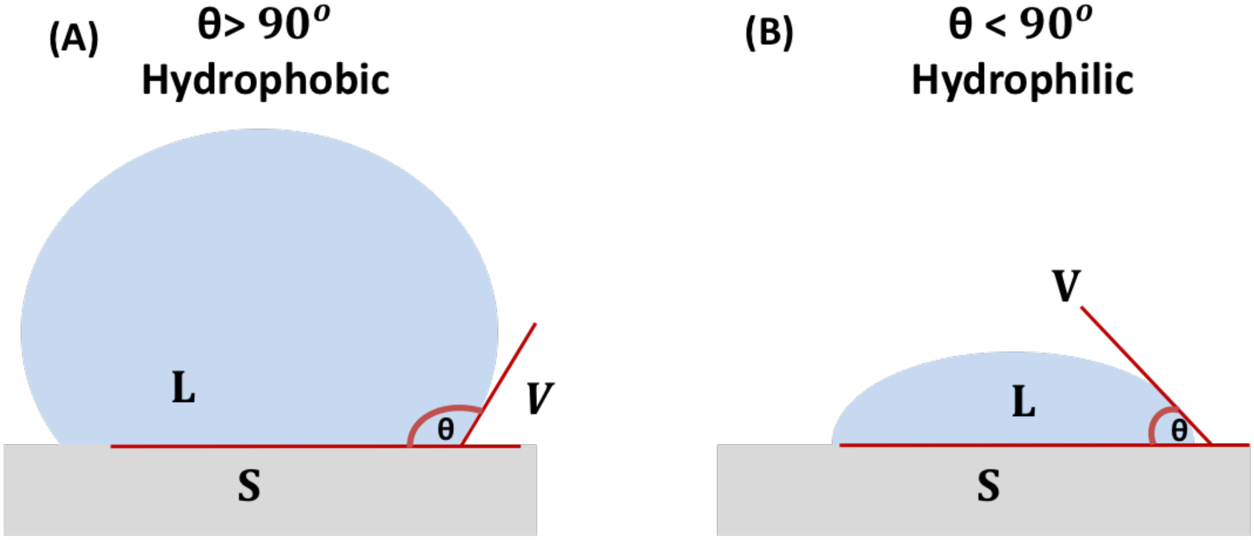

Figure 3.3 Schematic diagram showing the contact angles of water drops placed on (a) a hydrophobic surface and (b) a hydrophilic surface.

The contact angle of water increases as the surface free energy of the solid decreases. The wetting hysteresis between the advancing and receding affords a measure of the degree of surface roughness or morphology of the interface.[283,284]

A Rame-Hart model 100-00 goniometer (Netcong, USA) was used to measure contact angles. A microliter syringe was used to place a drop of water 2 µL onto the surface of the sample. The angle between solid/liquid and liquid/vapour interface was measured at three different locations on the sample and the average was taken.

3.7.2 X-Ray Photoelectron Spectroscopy (XPS)

XPS, also referred to as electron spectroscopy for chemical analysis (ESCA), is a method for analysing the surface chemistry of a material. XPS can determine a material's elemental composition as well as its chemical and electronic states. In XPS a sample in an ultra-high vacuum environment is irradiated with X-rays causing the emission of photoelectrons, whose energies are analyzed to yield information about the surface composition and bonding.[285,286] XPS yields quantitative compositional information and enables the determination of chemical states. The physical process underpinning XPS is shown in Figure 3.4.[287]

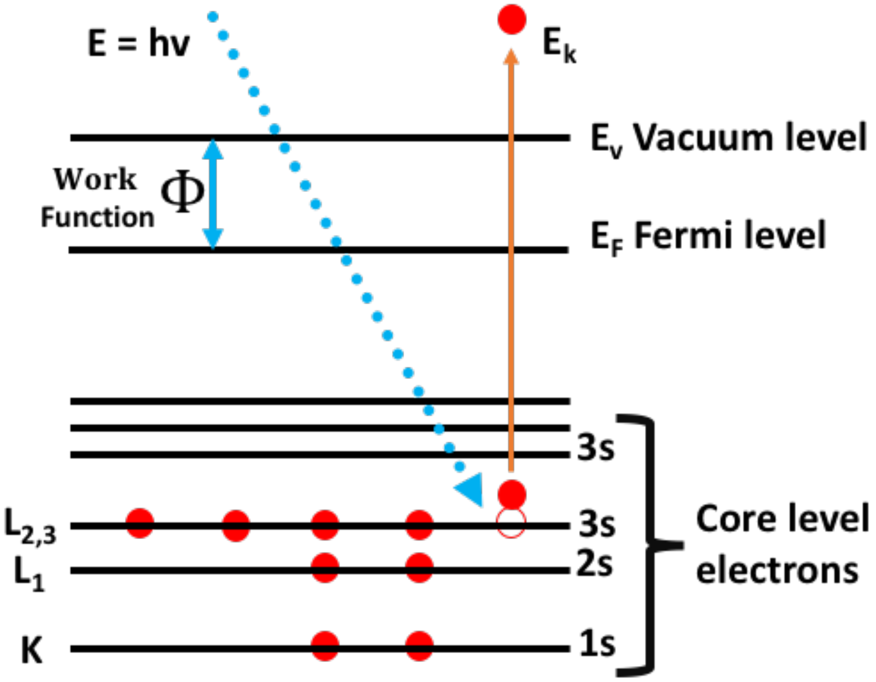

Figure 3.4 Schematic diagram illustrates the photoemission process and the relation to atomic band structure. XPS involves the measurement of the kinetic energies (KE) of photoemitted electrons ejected by irradiation of the sample with X-rays of energy hυ.

Absorption of X-ray photons leads to ejection of core electrons. The binding energy E_B is given by:

$$E_B = h\nu - E_K - \Phi \quad 3.3$$

Where hv is the energy of the incident x-ray photon, E_K is the photoelectron kinetic energy and ϕ is the work function of the spectrometer. The binding energy is element-specific and is effectively the ionisation potential of the orbital from which the photoelectron is emitted. The photoelectron spectrometer measures the intensity of photoelectrons as a function of kinetic energy, but this is usually displayed as a plot of intensity against binding energy.

The concentration of the atomic species in the sample surface layer can be calculated directly from the integrated peak area with a sensitivity of the order of 0.1 atomic %. The chemical sensitivity of XPS is based on the observation of small shifts in the BE energy of the core level electrons, which are dependent upon changes in the local bonding environment. Changes in the binding energy lead to changes in the photoelectron kinetic energy as recorded by the spectrometer.[287,288]

The surface sensitivity of~~,~~ arises because of the comparatively short inelastic mean free paths of photoelectrons, which are only able to travel a few nm through the solid before they experience inelastic scattering. The average distance traveled before electrons are inelastically scattered is identified as the inelastic mean free path (λ).

$$\boldsymbol{I(d) = I_o\, e^{-d/\lambda(\mathrm{E})}} \qquad \mathbf{3.4}$$

where I(d) is the intensity of photoelectrons emitted from depth d and I_o is the intensity emitted at the surface.

XPS measurements were performed using a Kratos Axis Ultra X-ray photoelectron spectrometer (Kratos Analytical, Japan), equipped with a delay-line detector and a monochromatic X-ray source. Monochromatic X-ray sources generate X-rays with a singular energy level or wavelength. X-rays strike the parallel crystal planes at an angle θ and are reflected at the same angle. The distance travelled by the X-rays depends on the crystal plane at which they are reflected. If the distance between two crystal planes each reflecting X-rays is d, then the path length difference is 2dsinθ. If this is equal to an integral number of wavelengths, then the X-rays interfere constructively. This effect produces the Bragg equation:

$$n\lambda = 2d\sin\theta \qquad 3.5$$

This is commonly achieved by employing an X-ray tube that has a certain anode material, such as aluminium (Al Kα, 1486.6 eV), magnesium (Mg Kα, 1253.6 eV), or copper (Cu Kα, 1486.6 eV). Monochromatic sources are characterised by their ability to offer exceptional energy resolution, rendering them well-suited for conducting intricate chemical analyses.

The operating pressure was 1×10^{-9} mbar. Survey spectra were acquired at pass energy of 160 eV and high-resolution spectra were acquired at pass energy of 20 eV. All XPS spectra were analyzed and curve-fitted using the Casa XPS software (v.2.3) (Casa, http://www.casaxps.com, U.K.) and were corrected relative to the C 1s signal at binding energy BE = 285.0 eV.

3.7.3 Atomic Force Microscopy (AFM)

The morphologies of nanostructured materials were characterized using atomic force microscopy (AFM). Tapping and contact mode were used in this study to obtain topographical images.[289,290]

In the tapping mode, a stiff rectangular cantilever oscillates, or taps, at or near the cantilever's resonance frequency as it traverses the sample. The tip strikes the sample intermittently at the bottom of each oscillation. In tapping mode, the tip sample contact time is short, and there is little drag, despite the fact that a mechanical tip-sample interaction occurs. Hence sensitive samples can be imaged without damage or severe image distortion. These advantages led to improvement in the resolution of a topographical image relative to contact mode. Tapping mode can be operated in air and liquid.[291]

In contact mode, the AFM tip is in mechanical contact with the surface of the sample and the tip-sample repulsive force is measured. While the tip is scanning the surface of a sample, the deflection of the cantilever is measured using a laser beam reflected from its back face onto a photodetector. In constant force mode, instantaneous changes in force as the probe travels across the sample are measured, and a feedback loop is used to adjust the tip height so that the cantilever deflection is restored to its present value. With the proper choice of softer AFM cantilevers, contact mode has been effectively utilized to image the morphology of soft samples, for instance, blood cells and self-assembled monolayers.[160] Moreover, measurement of local mechanical properties (e.g. stiffness, friction) is also possible in solution. In contact mode, the application of a load may cause damage to soft materials. Thus, the conditions used must be optimized carefully and for some samples it is necessary to use tapping mode instead.

A Digital Instruments Multimode V AFM (Digital Instruments, UK) instrument was used in this study. OTESPA-R3 silicon tapping probes were used at a scan rate of 1.5 Hz, and 512 lines per image to reveal the morphologies of nanoarrays samples. DNP-10 silicon nitride contact mode probes were used to measure the frictional properties and the roughness of micro-patterned samples. A liquid environment was used in contact mode to eliminate effects due to the formation of a meniscus at the tip-sample contact, thus reducing the force acting at the tip-sample contact. Additionally, liquid imaging reduces contamination. A biological buffer can be used to image and maintain the nature of biological samples in vitro.[161]

All samples were rinsed with ethanol then dried under dry nitrogen before imaging. The sample was placed on a metal disc and placed on the scanner head. In both tapping mode and contact mode, the tip was positioned in the cantilever holder, before being approached towards the sample under control from the instrument software. The laser was aligned on the end of the cantilever then the horizontal and vertical positions of the photodetector were aligned. Then the tip was moved manually close the surface until it was very nearly in contact with the surface, after which a routine in the software was used to detect the cantilever oscillations and bring the probe into interaction with the surface to enable image acquisition.

3.7.4 UV-visible absorption spectroscopy

UV-visible (UV-vis) spectroscopy determines the absorbance spectrum of a solution or solid compound. UV absorptions are primarily of an electronic nature and are associated with molecular resonance structures. UV absorption is an indispensable instrument for qualitative and quantitative analysis of a single-component substance or isolated extract. The UV-visible absorption spectra were acquired for samples. Figure 3.5 shows a schematic diagram of the spectrophotometer containing four essential parts: the light source, monochromator, the sample holder, and the detection system.

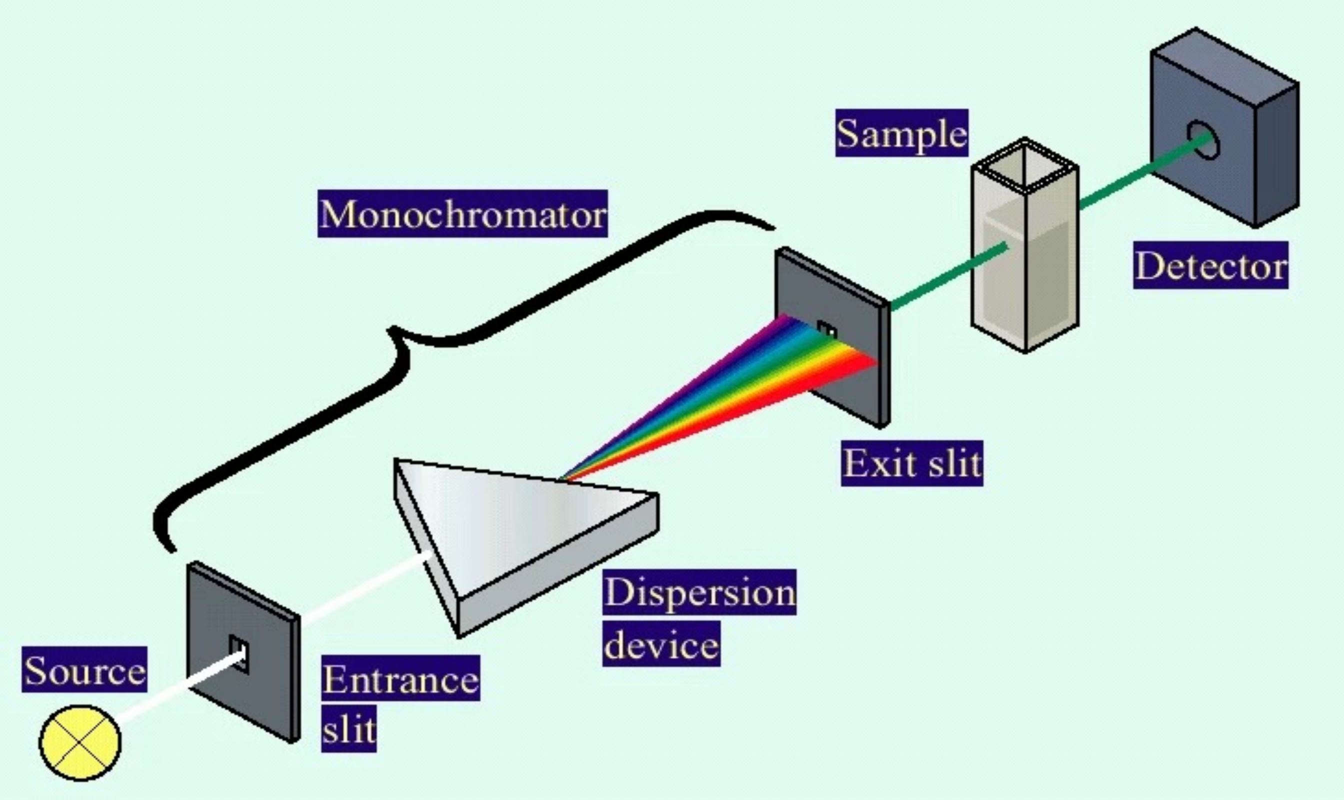

Figure 3.5 Schematic diagram of a Cary 50 UV-visible spectrophotometer.[224]

Most spectrophotometer instruments cover the spectral range from 190 nm to 1100 nm and they are used to study the transmittance spectra and absorption of the samples. Near UV refers to the portion of the ultraviolet spectrum that ranges from 185 nm to 400 nm. This region is just beyond the visible spectrum and is not visible to the human eye. The visible region of the spectrum ranges from 400 to 700 nm, while near infrared (NIR) starts from 700 nm and extends to 1100 nm. The absorption or attenuation takes place when the light passes through a thin film or a translucent liquid sample.

The samples were mounted on a home-made 3D printed sample holder. A standard quartz cuvette (10 mm transmitted path length) was used for the measurements in liquids. A zero/baseline correction was performed followed by the measurements of plasmonic arrays of gold nanostructures. Data processing included smoothing and identification of the absorbance maximum of gold nanostructures.

3.7.5 Spectroscopic Ellipsometry

Spectroscopic ellipsometry (SE) is a non-destructive optical technique commonly used to measure the thickness and optical properties of thin films.[292] SE measures the change in polarization when light is reflected or transmitted from a thin film. Figure 3.6 shows a schematic diagram of an ellipsometer. The optical part comprises a light source, two polarizing elements, called respectively polarizer and analyzer, and a photodetector.[293]

Ellipsometry measures a change in polarization as light reflects or transmits from a material structure. The polarization change is represented as an amplitude ratio, Ψ, and the phase difference, Δ. The measured response depends on optical properties and thickness of individual materials. Thus, ellipsometry is primarily used to determine film thickness and optical constants. However, it is also applied to characterize composition, crystallinity, roughness, doping concentration, and other material properties associated with a change in optical response.

The M-2000™-V spectroscopic ellipsometer system used in this study is based on advance diode array rotating compensator ellipsometer technology from J. A. Woollam Co. The model "V" (visible) ellipsometer uses a quartz tungsten halogen lamp (beam diameter 2–5 mm and spectral range 370–1000 nm) and diffraction grating in one unit with beam collimation optics, a fixed polarizer, and a compensator on a continuously stepped motor. The "output unit" is the stepper motor that drives an analyzer stage. Detector arrays and four-quadrant detectors align the system and sample. The ellipsometer may measure in situ (dynamic) and ex-situ (spectroscopic) with its manually controlled angle-of-incidence mechanism (-40° to 90°).

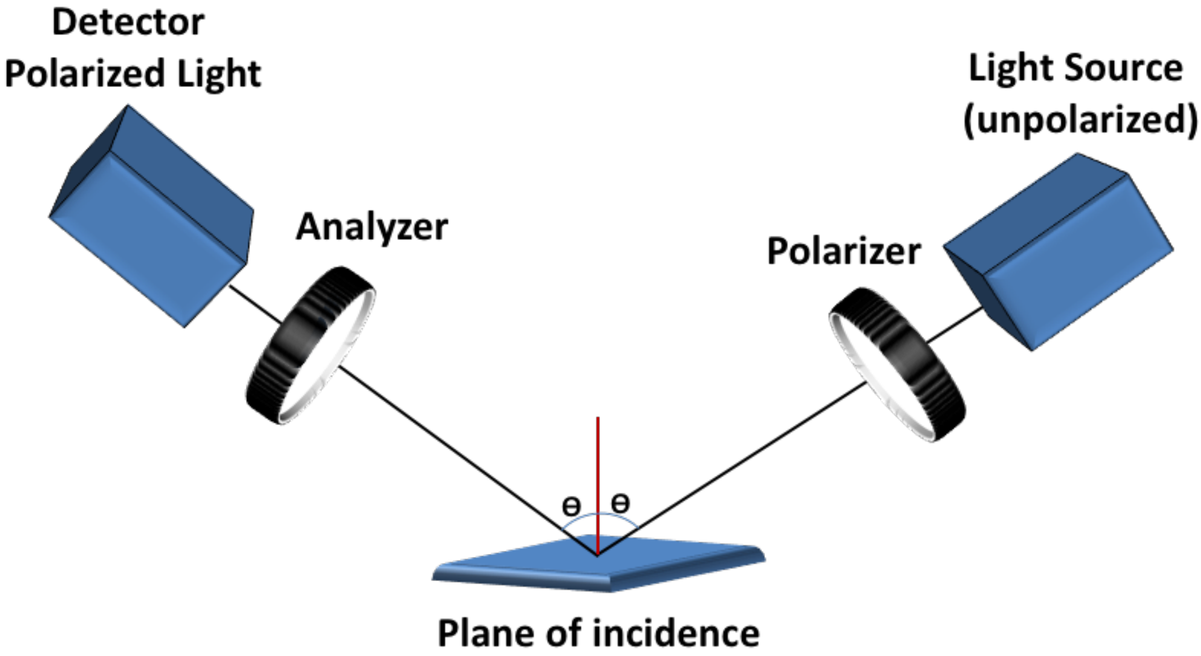

Figure 3.6 Schematic diagram of a spectroscopic ellipsometer.

.

Two measured parameters, Ψ and Δ by themselves are not very useful in characterizing a sample. Physical properties of the sample such as film thickness, optical constants and surface roughness are more informative. Ellipsometry does not directly measure these parameters; however, it measures functions of these parameters Ψ and Δ. Ψ is an angle whose tangent gives the ratio of the amplitude change for the s and p components, while Δ is the relative phase shift of the p and s components upon reflection. Analytic expressions can be written for predicting Ψ and Δ as functions of optical constants and the layer thickness. Complete EASE software (v. 6.2) was used to analysis the data that acquired by an ellipsometer. Fitting of the experimental spectra Ψ (λ) and Δ (λ) was carried out using the model presented in the Table 3.2. A Cauchy dispersion function was used for fitting the adsorbed protein layer. Optical parameter n and k for adhesive Cr layer, thin gold film and glass substrate were taken from the materials library.

Table 3.2 The model used for spectroscopic ellipsometry data fitting.

Layer	*Material*	*Fitted parameters*	*comments*
Layer #3	Organic layer	d, A	d is the thickness of the adsorbed layer in nm. The parameters of Cauchy model A_n=1.396, B_n=0.01 and C_n=0 were fixed during the fitting.
Layer #2	Au	d	thickness of the evaporated gold film in nm
Layer #1	Cr	d	thickness of the evaporated chromium film in nm
Substrate	BK7 glass	-	n=1.515

Plasmonic arrays of gold nanostructures were fitted with a more complex model. Briefly, the Au layer was replaced with a general oscillator layer containing 4 Gaussian oscillators. A Cauchy layer model was used to describe polymer film or adsorbed protein layer. In the Cauchy dispersion function n and B, and C are constants:[294]

$$\boldsymbol{n(\lambda) = A_n + \frac{B_n}{\lambda^2} + \frac{C_n}{\lambda^4}} \qquad \textbf{3.6}$$

With the fixed parameters A_n=1.396, B_n=0.01, and C_n=0 yielding a value of refractive index n=1.42 (at 633 nm) for all the molecular adsorbed layers. A is a dimensionless parameter: when λ → ∞ then n(λ) → A. B affects the curvature and the amplitude of the refractive index for medium wavelengths in the visible. C affects the curvature and amplitude for smaller wavelengths in the UV.

.

Figure 3.7 shows CompleteEASE Software of SE data is measured on the sample and how to analysis the data. Figure 3.7(A) shows the analysis tab of a layered optical model is built which represents the nominal structure of the sample. This model is used to “generate” SE data. The model includes many choices to build model and modify, for example, add, delete, and save. Figure

3.7(B) illustrates the model fit parameters are defined, and then automatically adjusted by the software to enhance the agreement between the measured data and model-generated by SE data. This is known as “fitting” the data.

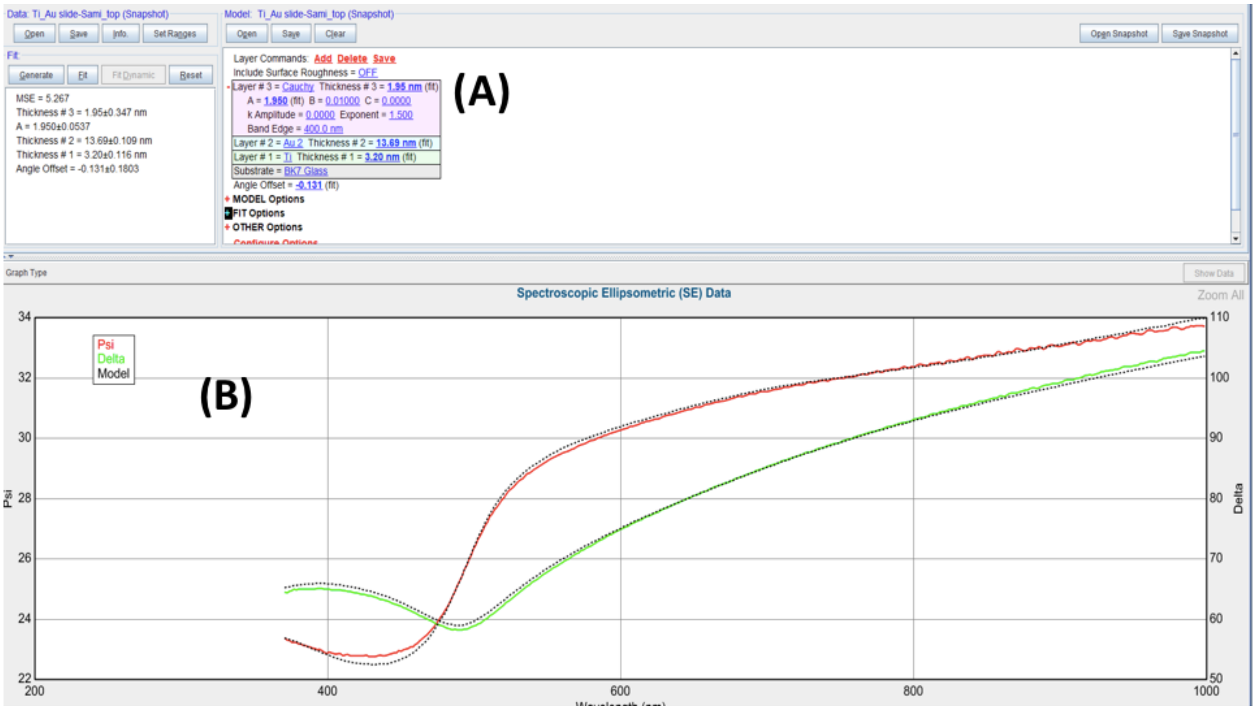

MSE = 5.267
Thickness # 3 = 1.95±0.347 nm
A = 1.950±0.0537
Thickness # 2 = 13.69±0.109 nm
Thickness # 1 = 3.20±0.116 nm
Angle Offset = -0.131±0.1803

Layer Commands: Add Delete Save
Include Surface Roughness = OFF
Layer # 3 = Cauchy Thickness # 3 = 1.95 nm (fit)
A = 1.950 (fit) B = 0.01000 C = 0.0000
k Amplitude = 0.0000 Exponent = 1.500
Band Edge = 400.0 nm
Layer # 2 = Au 2 Thickness # 2 = 13.69 nm (fit)
Layer # 1 = Ti Thickness # 1 = 3.20 nm (fit)
Substrate = BK7 Glass
Angle Offset = -0.131 (fit)

Figure 3.7 CompleteEASE Software for SE data is measured on the sample. (A) model of Au substrate with SAMs and (B) illustrate the fitting data.

3.8 Protein Immobilization

A comparatively stable method of protein immobilization is to link a protein to the substrate via a covalent bond. For protein immobilization, we followed the protocol described in Tsargorodska et. al.[295] Figure 3.8 shows schematically the procedure used for protein immobilisation. An amine-terminated self-assembled monolayer is formed on the gold surface, and incubated with glutaraldehyde, which binds to the amine-terminated SAM via the formation of an imine bond (Schiff’s base). The free aldehyde is able to couple to aminobutyl nitrilotriacetic acid (AB-NTA), to yield an NTA-functionalised surface which, after complexation with Ni^{2+}, is able to bind strongly to His_6-labelled proteins.

Gold nanostructure nanoarrays were functionalized with 11-amino-1-undecanethiol hydrochloride by immersion in a 1 mmol solution in ethanol for overnight, then washed with ethanol and dried with nitrogen, derivatized with glutaraldehyde (12.5% in water) for 30 min, and immersed in a 20 mM aqueous solution of Nα,Nα-Bis (carboxymethyl)-L-lysine trifluoroacetate salt (AB NTA), pH 5 for overnight. Then the samples were rinsed with DI water, dried under a stream of nitrogen and immersed in a 10 mmol aqueous solution of nickel sulfate for 5-7 min to ensure complexation of NTA by Ni^{2+}. The samples were washed with DI water and dried under a stream of nitrogen to remove excess Ni^{2+}. The samples were then immersed in His-tagged BT6 Maquette in 20 mM HEPES buffer, 0.03% BDDM, pH 7.5. The samples were left immersed in the maquette/buffer solution for overnight in a humid chamber in a fridge. The relative humidity is the ratio of the amount of moisture in the air to the moisture it can hold. Finally, the samples were washed with 2HEPES buffer and deionized water and dried under a stream of nitrogen. To produce the ideal conditions for particular biological or chemical processes, such as protein attachment or cell culture, the humidity level is adjusted and maintained at a specific percentage. Humidifiers, water reservoirs, and other humidity control systems can help with this.

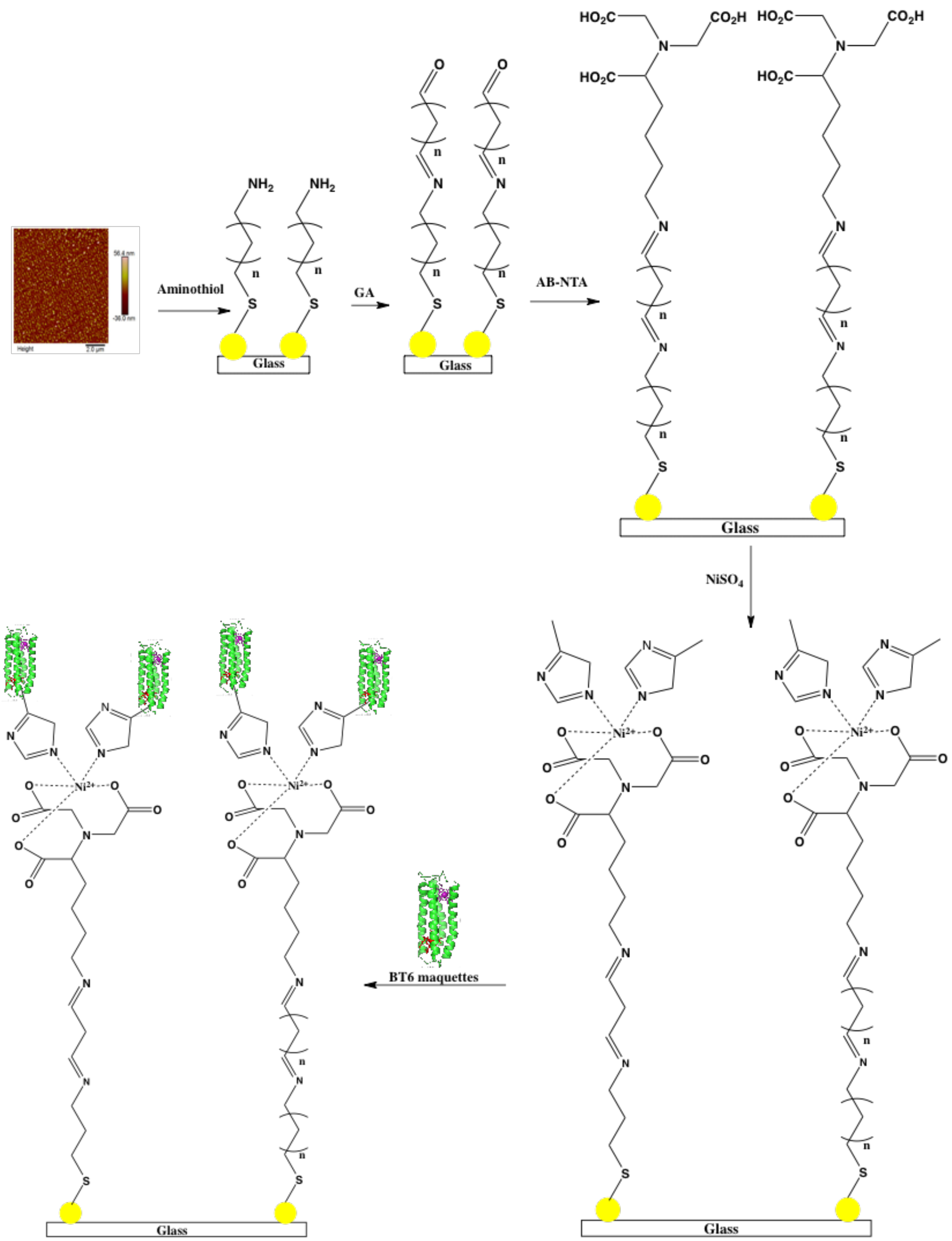

Figure 3.8 Schematic representation of the method used to couple His-labelled proteins to gold nanostructures. On the gold surface, an amine-terminated SAM forms. This monolayer is then incubated with glutaraldehyde, which attaches itself to the amine-terminated SAM by forming an imine bond, or Schiff's base. After reacting with Ni2+ to form an NTA-functionalized surface, the free aldehyde can couple to aminobutyl nitrilotriacetic acid (AB-NTA) and form a strong bond with His6-labelled proteins.

Streptavidin and Immunoglobulin G (IgG) were dissolved in 0.1 M PBS buffer then prepared at different concentrations. The sample was immersed in protein solution for different times, rinsed with buffer, and gently dried with a stream of nitrogen.

3.9 Cysteine Methacrylate (CysMA) Synthesis

Cysteine Methacrylate (CysMA) was synthesized following the published method of Alswieleh et al,[296] via the selective thia-Michael addition of cysteine to a commercially available methacrylate-acrylate precursor in aqueous solution without recourse to protecting group chemistry (as shown in Figure 3.9). In a 250 mL round-bottom flask, L-cysteine (15.13 g, 124.88 mmol) was dissolved in 100 mL of deionized water. Then 3-(acryloyloxy)-2-hydroxypropyl methacrylate (29.43 g, 137.36 mmol) was added to the reaction mixture, followed by dimethylphenyl phosphine (20 µL, 1.47 x 10^{-1} mmol). The aqueous reaction solution was stirred for 2 h at 20°C and subsequently cooled to room temperature. The solution was washed twice with 50 mL of ethyl acetate and 50 mL of dichloromethane. In the final step the concentrated aqueous solution was freeze-dried overnight, yielding the CysMA monomer product as a pure white solid (39.8 g, 97% yield). The reaction mechanism is shown in Figure 3.10.

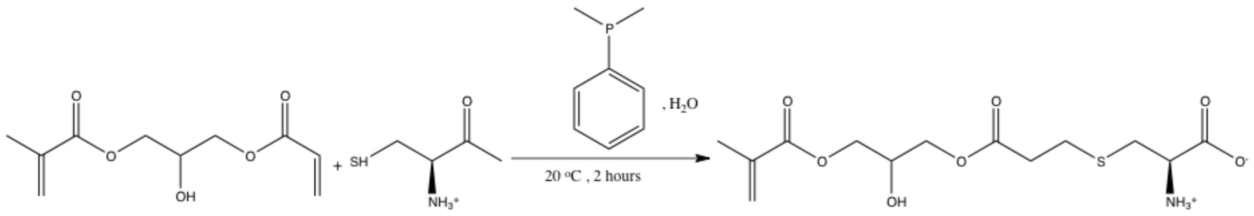

Figure 3.9 Synthesis of cysteine methacrylate (CysMA) monomer via the selective thia-Michael addition of cysteine to a commercially available methacrylate-acrylate precursor.

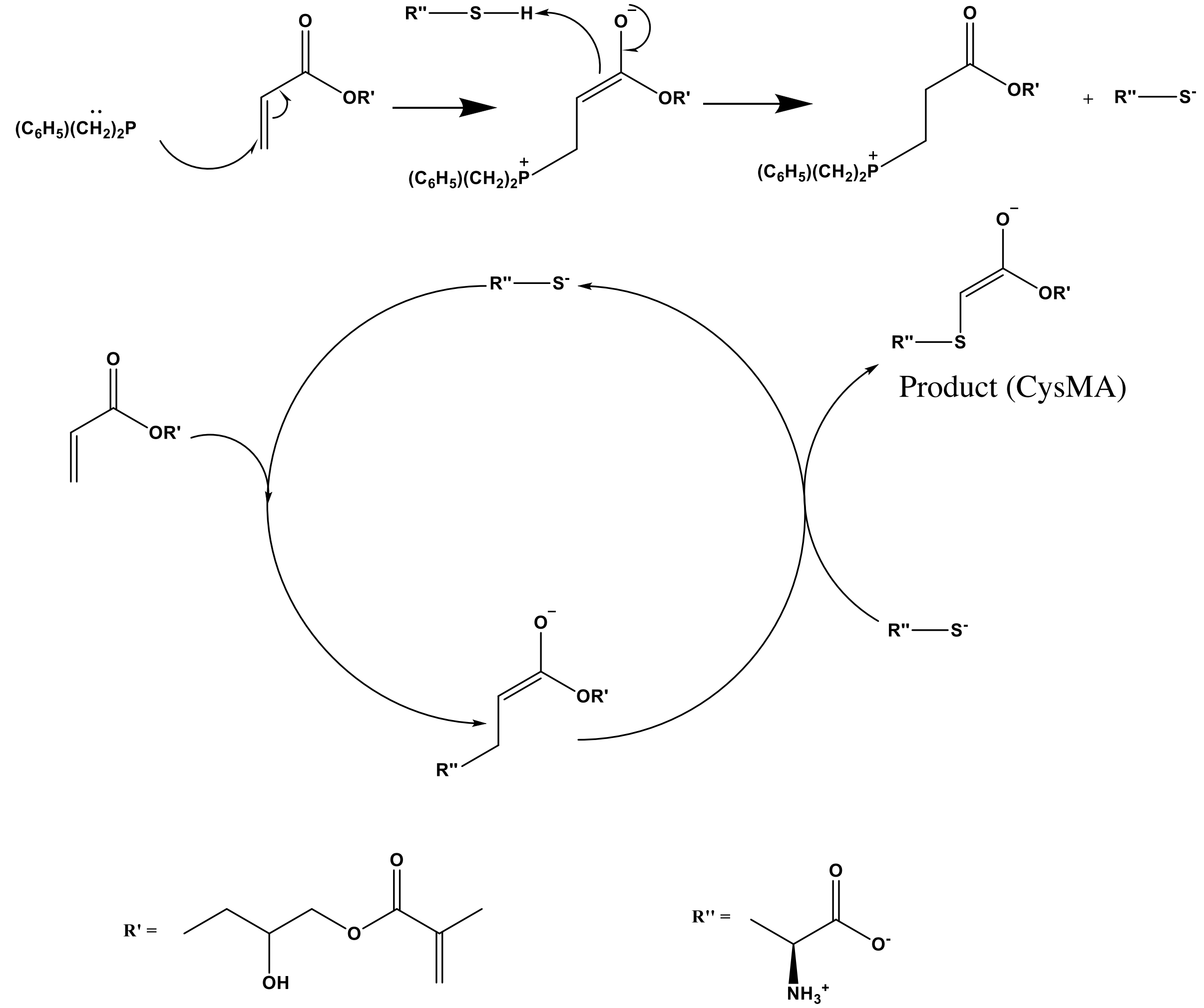

Figure 3.10 The mechanism of preparing the cysteine methacrylate monomer (CysMA) by a selective thia-Michael addition.

4. Fabrication and characterization of gold nanostructures for biosensor applications

4.1 Introduction

Developing chip-based plasmonic diagnostic systems capable of widespread utilization in hospitals and GP surgeries, requires the creation of inexpensive methods for the fabrication of surface-supported films of gold nanostructures with programmable properties. The objective of this chapter is to examine the possibility of using interferometric lithography to produce films constructed of gold nanostructures with well-defined dimensions and properties that cover macroscopic (~ cm^2) regions.

The free electrons at a metal surface oscillate about their mean positions with a characteristic frequency identified as the plasma frequency. Resonant coupling of incident electromagnetic radiation to these plasma oscillations leads to the formation of surface plasmon polaritons, (or plasmons). Localised surface plasmon resonances (LSPRs) result from the resonant coupling of light to the plasmons of sub-wavelength metallic structures. Gold and silver nanoparticles exhibit plasmon oscillations whose frequencies correspond to the visible region of the electromagnetic spectrum and are therefore strongly coloured.[297] There has been widespread interest regarding the use of LSPRs in medical diagnostics, by measuring small red shifts in the energies of their plasmon bands following the adsorption of biomolecules at their surfaces.

Utilising such sensors in healthcare settings requires the fabrication of surface-supported films of nanoparticles with well-defined properties that are tailored to a specific application, and which cover large enough areas for convenient analysis with commonly available analytical instrumentation (such as, a spectrophotometer). Two approaches have been explored in the literature: firstly, electron beam lithography (EBL) has been used to fabricate nanostructures that have precisely controlled structures. The advantage of EBL is that it provides nm precision; however, it also requires the use of highly expensive apparatus and skilled technical operatives and therefore, EBL is considered too expensive to be used for the mass production of sensor chips. Secondly, an alternative approach is provided by colloidal lithography, in which metal is evaporated through the interstices between polymer nanoparticles in self-assembled films of particles formed on a suitable substrate. While colloidal lithography provides an inexpensive solution to the production of nanostructures over large areas, the degree of programmability is very modest.

This chapter explores an alternative approach based on the use of interferometric lithography (IL) in conjunction with a self-assembled monolayer (SAM) resist. The aim is to achieve a high degree of control over nanoparticle morphology, and facilitate nanofabrication over significant areas, thus combining the superior aspects of EBL and colloidal lithography in a single approach.

SAMs have been used to fabricate nanostructured materials with extremely high resolution via techniques such as electron beam lithography, interferometric lithography and scanning near-field photolithography.[164,298] SAMs of alkanethiols on gold surfaces can be patterned via photolithographic techniques. In these processes, the thiol is photo-oxidised, rendering it labile at the surface, and enabling it to be replaced by a contrasting thiol or displaced from the surface by an etchant which subsequently erodes the underlying material.

Photo-oxidation is initiated by hot electrons that are produced on the gold surface following irradiation with deep UV light.[299] These hot electrons may tunnel into an antibonding state of the adsorbate sulfur atoms which initiates the photo-oxidation reaction that leads to the formation of alkylsulfonate products as shown.[267]

$$Au - SR + {}^{3}/_{2}\, O_2 + e^- \longrightarrow Au + R - SO_3^-$$

In contrast to the strongly bound alkylthiol, the alkylsulfonate is easily displaced from the surface to expose clean gold substrate which can be modified by the adsorption of a second, contrasting thiol or treatment with an etching solution.[300,301]

Octadecanthiol (ODT) monolayers have been utilized as etch resists to fabricate micro- and nanostructures in 3D by using a solution of mercaptoethylamine (MEA) as a mild etchant for gold.[111] Etching was achieved after patterning the SAMs via exposure to UV light through an electron microscope grid, or by scanning near-field photolithography (SNP).

This chapter presents a systematic investigation of the lithographic process. The effects of variations in the exposure and etching conditions on the morphologies of the resulting nanostructures are characterised. This research hypothesises that the plasmonic properties of the resulting nanostructures can be improved by annealing; therefore, the extinction spectra of nanostructure arrays formed by IL are examined as a function of the annealing conditions. Finally, measurements are made on a series of model analytes. Under certain conditions, it is demonstrated that strong coupling of the plasmon mode to the analyte may occur, leading to the creation of new hybrid light-matter states identified as plasmon-exciton polaritons (or plexcitons) which can be observed experimentally when splitting the plasmon band.

4.2 Results and Discussion

4.2.1 Fabrication of Gold Nanostructures

The photooxidation of octadecanethiol SAMs on Au was examined via X-ray photoelectron spectroscopy (XPS). The composition of the gold substrate and the octadecanethiol SAMs was assessed using high-resolution XPS to determine that they were free from contamination. The samples were exposed to light from a frequency-doubled argon ion laser at a range of doses before the acquisition of the XPS spectra. Figure 4.1 shows the XPS spectra acquired for SAMs of octadecanethiol before and after exposure to a dose of 64 J cm^{-2} of UV light. The C1s peak remains unchanged after exposure to UV light. No oxygen is observed in the spectrum of the as-prepared film, but a substantial O1s peak is observed after expsure to 64 J cm^{-2} of UV light. The spectrum of the as-prepared sample exhibits a doublet at 161.5 and 163 eV attributed to the S2p$_{3/2}$ and S2p$_{1/2}$ peaks (as shown in Figure 4.1 (b)) that result from the spin-orbit coupling.[301] Based on the previous work of Tarlov et al.[108] and Huang , Hemminger and Leggett,[301] it was expected that a feature would be observed at ~167 eV which correspond to alkylsulfonate oxidation products. However, such a feature is not observed in the S2p spectrum in Fig 4.1 and instead, a small shoulder appears at 165 eV and the reason for this difference remains undetermined. As described below, it was possible to create nanostructured films when the exposure was conducted using an interferometer; therefore, the SAM must be removed during UV exposure. One possible explanation for the lack of sulfonate features in the S2p spectrum is that under the conditions of this study, there was only partial oxidation of the thiolates occurred which yielded an intermediate product (for example, RSO_2^-) that caused the small peak at 165 eV.

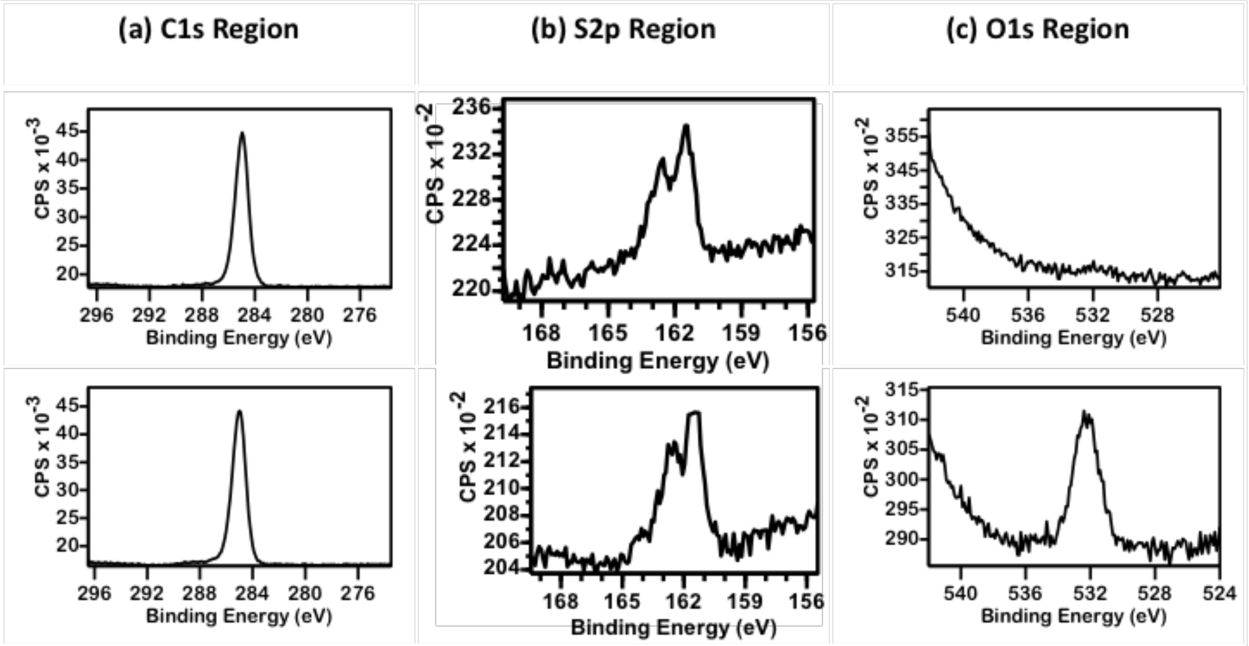

Figure 4.1 XPS spectra of octadecanethiol SAMs as prepared (top) and after exposure to a UV dose of Jcm^{-2} (bottom). (a) C 1s spectrum. (b) S 2P spectrum and (c) for O 1s spectrum.

The photo-oxidation process was also characterized using atomic force microscopy (AFM). AFM topographical images were acquired for the photo-oxidation of SAMs of ODT to study their surface roughness. Friction force microscopy (FFM) images were acquired in parallel with the height images. In FFM, the lateral photodetector deflection in mV is proportional to the friction force acting at the tip-sample contact. The FFM images were acquired, and the mean lateral force was determined by calculating the mean of the lateral photodetector signal along line sections through the images. Figure 4.2 (a to c) contains a series of illustrative friction force images of samples exposed to different doses up to 32 Jcm^{-2}. Figure 4.2 (d) shows the variation in the mean lateral photodetector signal as a function of the UV for several of samples. It was found that the friction force of the films increased with the dose: it increases rapidly with doses up to 10 Jcm^{-2}

and more gradually thereafter, reaching a limiting a value at a dose of 32 Jcm^{-2}. These data suggest that a dose of 32 Jcm^{-2} is sufficient to cause complete photo-oxidation of the SAMs.

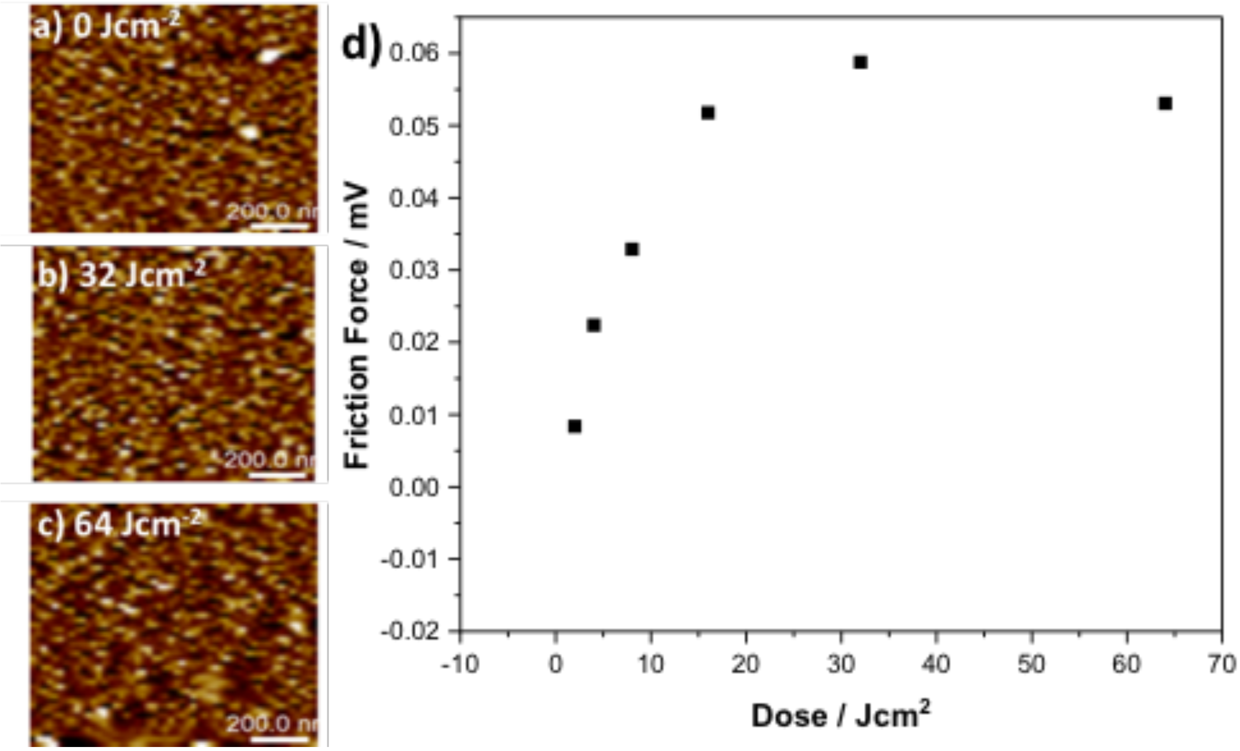

Figure 4.2 AFM topographical images of exposed samples in different doses (a) 0 J cm^{-2} (b) 32 J cm^{-2} (b) 64 J cm^{-2} (d) the FF as functions of doses.

4.2.2 Optimization of etch time

The optical properties of metal nanoparticles are determined by their dimensions and morphologies.[11] A fundamental aim of this work was to achieve effective control over nanostructure morphology during the lithographic process. The etching time can be varied to control the sizes of the nanostructures produced by determining the height and full width at half maximum (FWHM) of the structures. If the etch time is too short, the nanostructures will be inadequately defined and if the etch time is protracted, the nanostructures will be too small, or completely eradicated. Arrays of gold nanostructures were fabricated by exposing SAMs of ODT onto gold surfaces at a dose of 30 J cm^{-2} at 244 nm using a Lloyd's mirror interferometer and subsequently etching them in a solution of mercaptoethylamine (cysteamine) in ethanol. A drop of ammonia is added to the etch solution to act as a potential catalyst in the etching process. Cysteamine dissolves the gold by acting as a bidentate ligand to coordinate with gold atoms by both the thiol and amine groups.[111] The samples were imaged using AFM (Figure 4.3). To determine the optimum etching times, the gold nanostructures were immersed in the etch solution for various lengths of time. Figure 4.3. (a to d) shows samples formed by exposing ODT SAMs on 15 nm thick gold films to a dose of 32 Jcm^{-2} and immersing them in the etch solution for 5, 10, 13, and 20 min. As demonstrated in Figure 4.3, the space appears to vary from 250 nm to 500 nm. In Figure 4.3(a) the peak to trough height (from left to right) varies between 3.6 and approximately 2 nm. The peak to trough height in Figure 4.3(b) appears smaller than in Figure 4.3(a) even through the etch time is prolonged. Figure 4.3(d) shows that the gold nanostructures began to erode when the etching time exceeds 20 min.

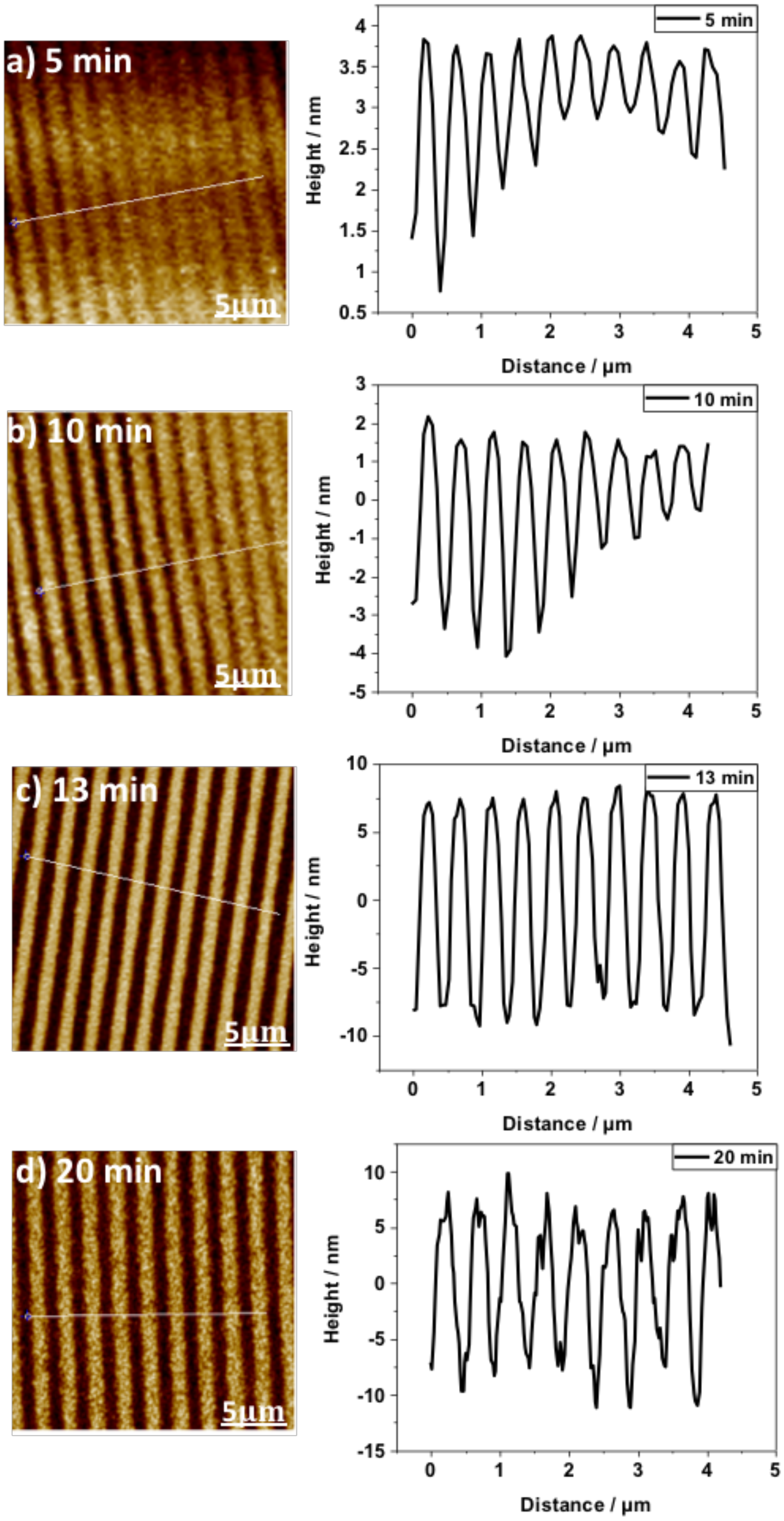

Figure 4.3 AFM images with cross sections detailing the effect of etching time on gold nanostructures: (a) 5 min etching time, (b) 10 min etching time, (c)13 min etching time and (d) 20 min etching time.

Figure 4.3 shows AFM images of nanostructures formed under optimized conditions created by adequate exposure and etching time. Although fully formed SAMs of ODT on gold may resist etching by the cysteamine solution, it was observed that unoxidized areas in the samples patterned by IL were affected by exposure. This could be attributed to the effect of the etching solution on the ODT monolayers in unoxidized areas, via undercutting of the SAM (lateral etching) due to the isotropic nature of the etch process.

Using IL, areas as large as 10 x 5 mm^2 can be exposed. The pitch was varied by changing the angle of incidence of the laser beam on the mirror. The dose was kept constant at 34 J cm^{-2}, and identical developing processes and conditions were maintained for all samples. The angle between the sample and the mirror was varied systematically (from 13^o to 35^o) and the AFM images were recorded. As seen in Figure 4.5, increasing the angle leads to the production of narrower features with a higher density at the surface. At 13^o, the FWHM and pitch were 238 and 251 nm, whereas at 35^o, they had decreased to 122 and 131 nm, respectively. Figure 4.6 shows that increasing the mirror angle leads to a reduction in the period and FWHM.

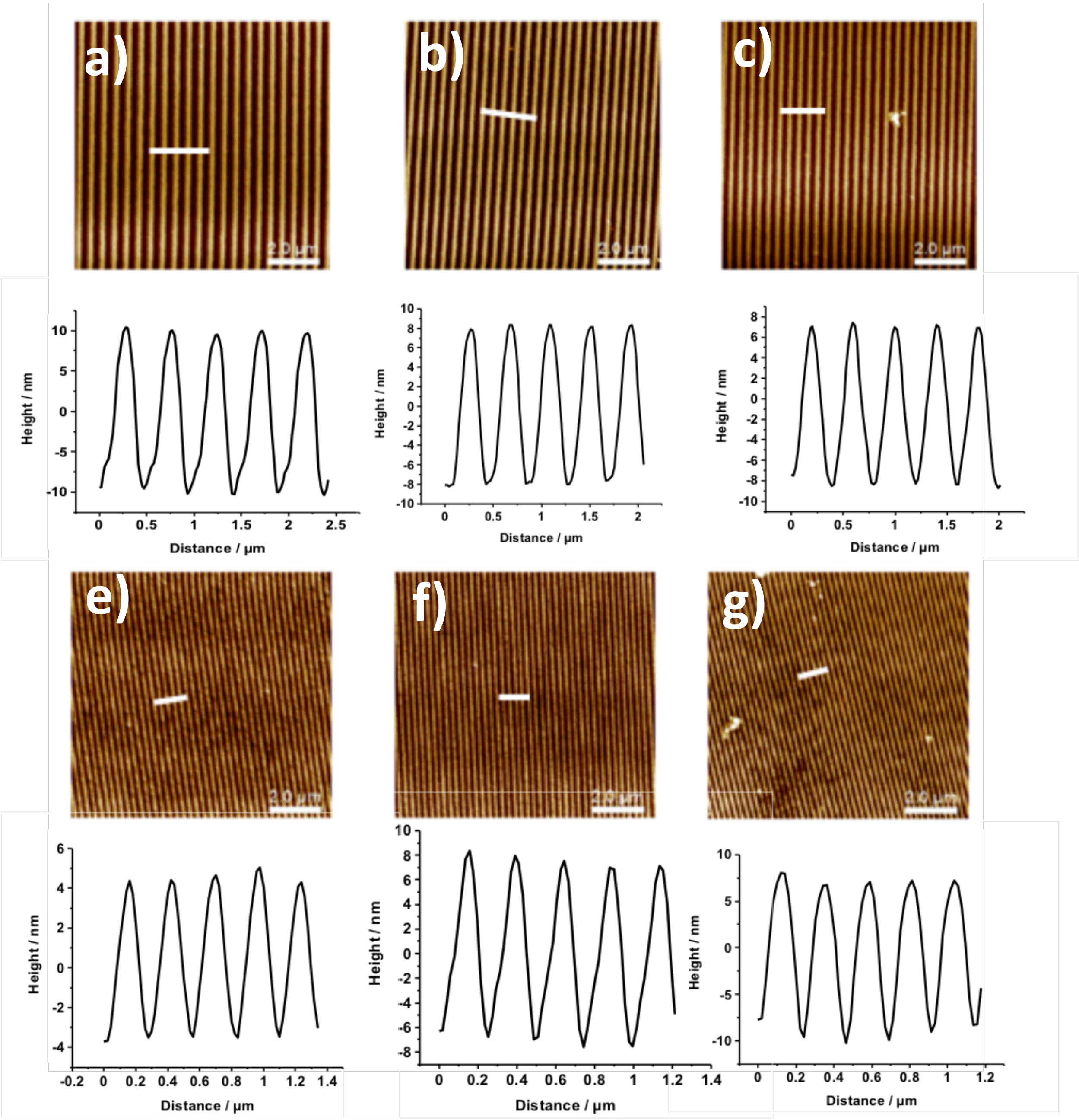

Figure 4.4 AFM topographical images of Au nanostructures on SAMs of ODT when exposed to UV-laser (244) through IL system. The mirror angle was set as (a) 13°∓ 2, (b)15°, (c)20°, (d)25°, (e)30° and (f)35° respectively and cross sections.

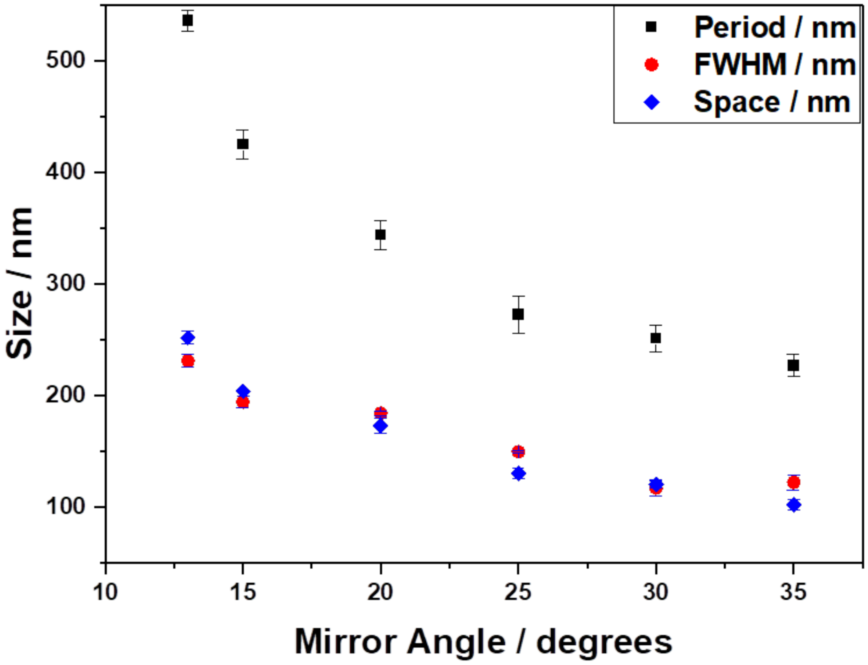

Figure 4.5 The change in the period (peak to peak distance between the rows of nanostructures) , space (distance between one particle to the next particle in the array) , and FWHM (the width of particle size) of the lines of nanostructures as a function of the mirror angle 13°∓ 2, 15°, 20°, 25°, 30° 35°.

4.2.3 Fabrication of Gold Nanodots by Etching Gold after Patterning using Orthogonal Exposures

To create arrays of nanocrystals, a double exposure process was developed, in which the sample is rotated between exposures. The overlapping interferograms enable the fabrication of a wide variety of structures. A double exposure was carried out after rotating the sample on the stage through an angle ϕ (as shown in Figure 4.6).

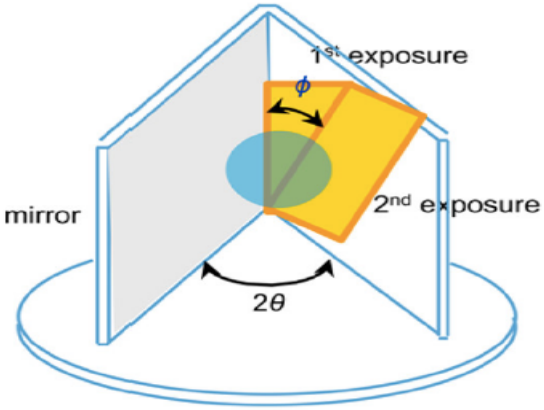

Figure 4.6 Schematic of the fabrication of nanostructures via two exposures. The sample is rotated through an angle φ between exposures.[111]

The sample was exposed to 34 J cm^{-2}, rotated by 90° on the stage, and subsequently exposed to an additional dose of 20 J cm^{-2}. After photopatterning, the samples were immersed in the etching solution for between 12 and 15 min. The resulting samples consisted of arrays of gold nanostructures of distinct types. Figure 4.7 shows AFM topographical images of these Au nanostructures. The mirror angle (angle of incidence) varied between 10^{o} and 40^{o}, and the rotation angle was fixed at 90^{o} for each exposure. The pitch of the rows of nanostructures and FWHM was found to be 249 nm and 257 nm at 13^{o} respectively, whereas at 35^{o}, they had decreased to 106 and 100 nm, respectively.

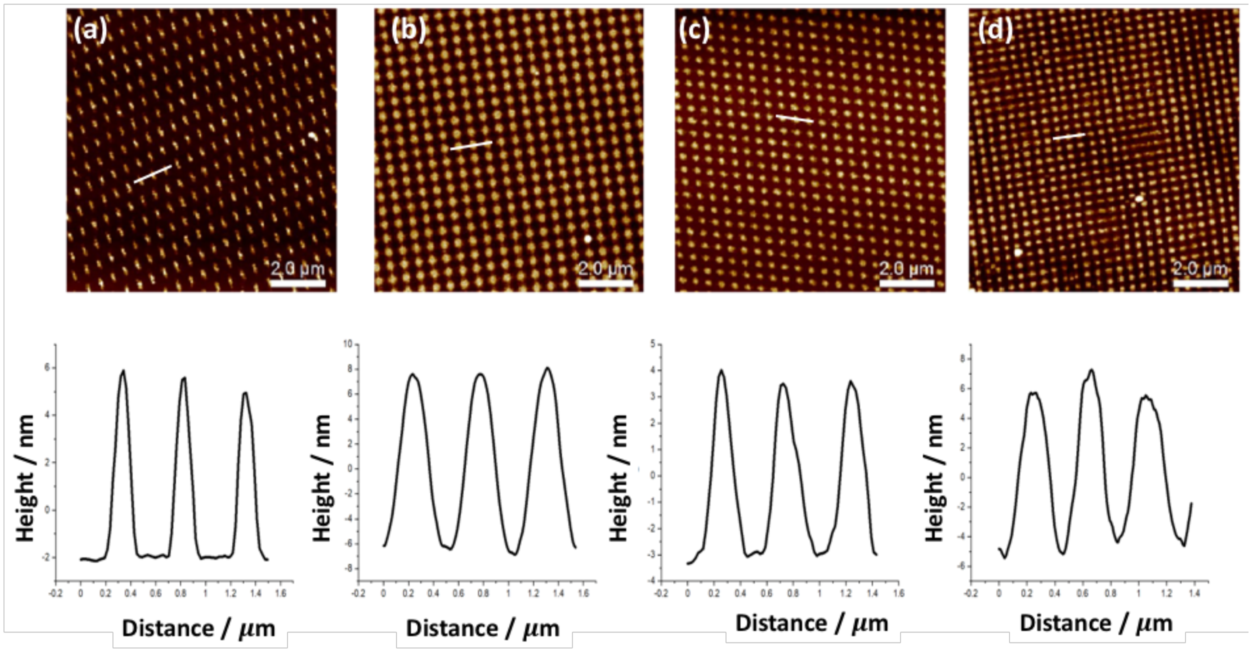

Figure 4.7 AFM topographical images of Au nanostructures on SAMs of ODT formed by IL using a double-exposure process when the exposure to UV-laser (244 nm) through IL system and the mirror angle was (a) 25°, (b)15°, (c)20°, and (d)35° respectively and $\phi = 90^o$ for all samples and cross sections.

Figure 4.8. shows AFM topographical images and cross sections of Au nanostructures fabricated via a double-exposure process which used the same mirror angle (25° angle of incidence) and different angles of rotation between exposures. The sample was exposed to 34 J cm^{-2}, rotated by 20°, 30°, 40°, 50° and 60°, and exposed to a further dose of 20 J cm^{-2}. After photopatterning, the samples were immersed in the etching solution for 12 to 14 min. The resulting samples consisted of arrays of gold nanostructures. For an angle of 2θ between the two beams of 20°, the period was equal to the laser wavelength. The pitch was 260, 381, 522, and 540 ±12 nm for samples a to d, respectively, and the corresponding FWHM are 162, 161, 216, and 241±12 nm.

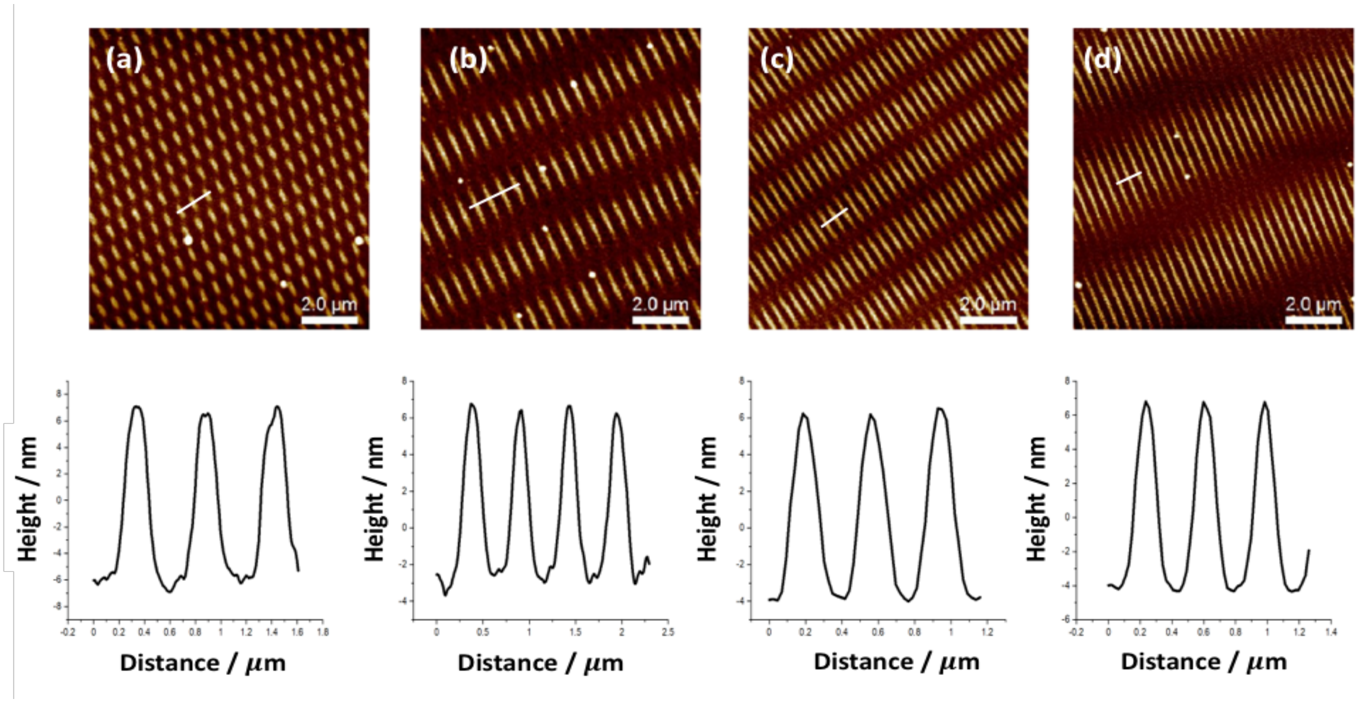

Figure 4.8 AFM topographical images and cross sections of Au nanoarrays formed by IL using a double-exposure process in which the mirror angle is kept fixed at 25° while the angle of rotation is varied. $\phi = 60^o, 45^o, 30^o, and\ 20^o$ in (a-d) respectively.

Figure 4.9 illustrates that the period and FWHM decrease with an increasing angle of incidence and that the rotation of samples between exposures has no effect~~; therefore,~~ based on these studies, can be concluded that the period and FWHM decrease when the mirror angle decreases. This facilitates the design and creation of gold arrays of specific sizes and pitches for any specific application.

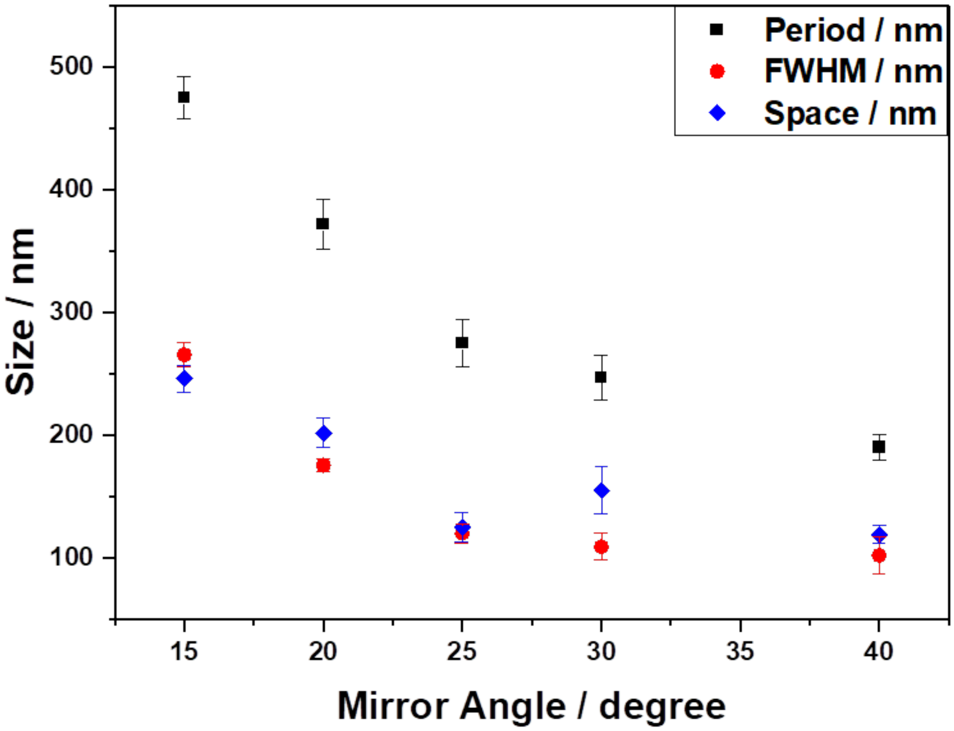

Figure 4.9 The change in the period (peak to peak distance between the rows of nanostructures) , space (distance between one particle and the next particle in the array) , and FWHM (the width of particle size) nanostructures as a function of the mirror angles for various samples while the mirror angle caries and the dose remains constant at 64 Jcm^{-2}.

However, calculating the expected angle of incidence based on the period of patterns in the various samples and comparing it to the predetermined angle of incidence revealed that there is no significant difference.

4.2.4 Annealing

The gold films employed in nanofabrication are formed via thermal evaporation and are polycrystalline. To create structures with improved plasmonic properties, arrays were annealed following nanofabrication. Annealing produced nanostructures with a uniformly high degree of crystallinity, which led to the observation of intense plasmon bands. Samples were annealed by heating at 525 °C for 120 min and characterised by AFM. AFM images of a sample before and after annealing are presented in Figure 4.10. After annealing, the periodicity of the nanostructures is retained; however, the morphologies of the nanoparticles are altered. Annealed nanostructures were found to be higher but smaller, laterally, than was the case before annealing. Data shows the extent of the change in dimensions that was observed for a representative selection of samples that exhibited no plasmon absorptions in their as-prepared state. AFM images of representative samples are shown. The morphologies of the structures also changed because of annealing, undergoing a transition from being approximately flat-topped to approximately pyramidal in cross-section and after annealing, all structures yielded absorbance spectra that were significantly altered and exhibited strong plasmon bands (see Figure 4.10). Gold nanostructures yield strong plasmon bands, and annealing causes recrystallization of the gold so that all the specimens yield strong plasmon absorptions.

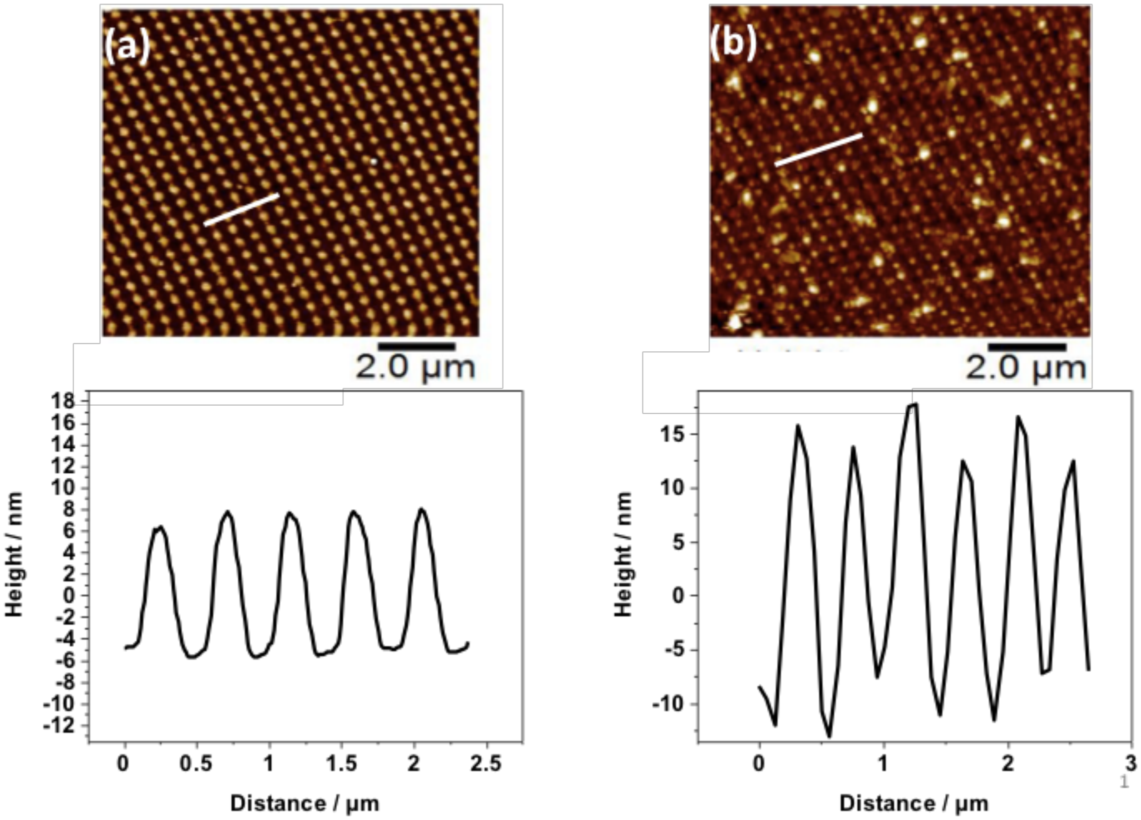

Figure 4.10 AFM topographical images of Au nanoarrays with cross sections (a) as prepared by IL before annealing and (b) after annealing at 525 °C for 120 min.

Figure 4.10 contains AFM images of a sample before and after annealing. After annealing, the sample still exhibits a periodic structure; however, the morphology is somewhat altered: there is a significant change in the heights of the nanostructures (which doubled in magnitude from 8 to 18 nm) which is attributed to recrystallization of the gold during annealing. Additionally, in some locations, a small number of crystallites is formed between rows in the pattern which suggest that the gold becomes mobile during annealing.

4.2.5 Plasmon Absorption and Extinction Spectra of Gold Nanostructures with Different Shapes

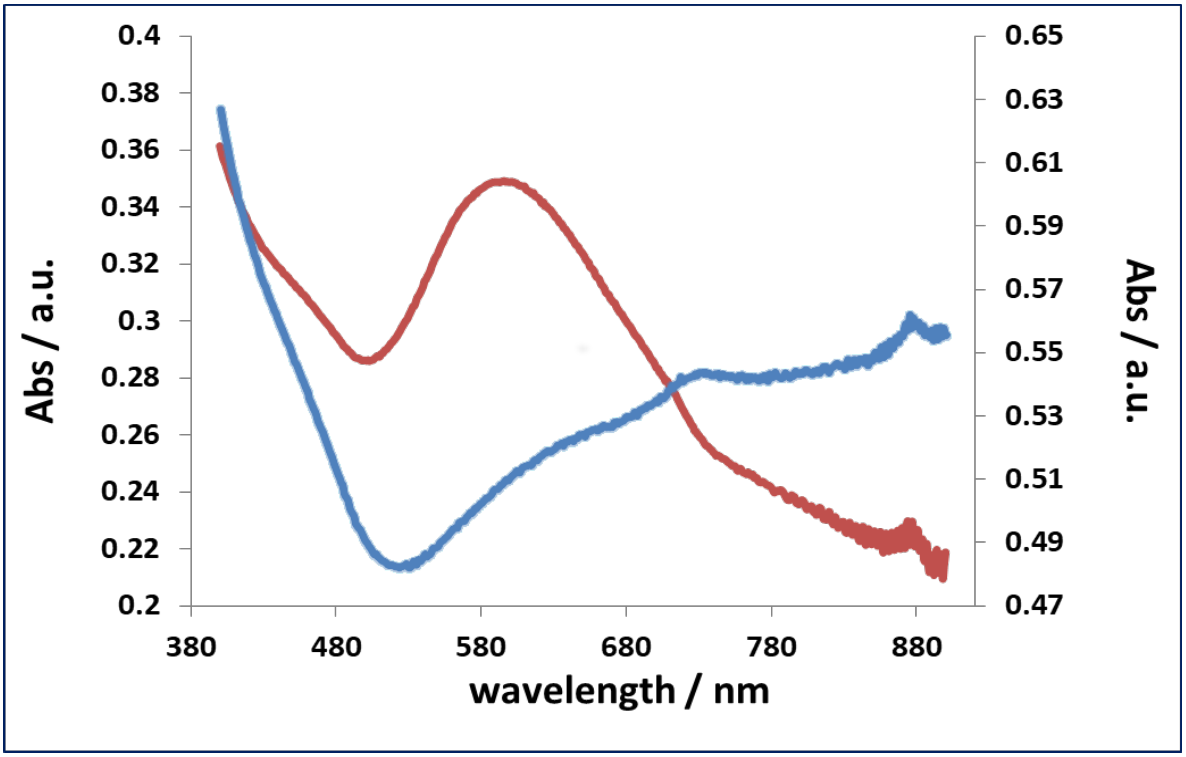

Figure 4.11 Absorption spectra of the array of gold nanodots shown in Figure 4.10 before annealing (blue line) and after annealing (red line). Annealing was conducted at 525 °C for 120 min with pitches of (a) 230 nm and (b) 270 nm, FWHM of (a) 250 nm and (b) 287 nm and phi 90°.

Arrays of gold nanostructures fabricated using IL were characterised via optical spectroscopy. Figure 4.11 shows the extinction spectra of the array of gold nanodots (whose morphology is shown in Figure 4.10) as recorded before and after annealing. A plasmon band is not observed for the as-prepared array; however, after annealing a strong feature emerges at 580 nm that is attributed to a gold plasmon band. There was some variation in the plasmon band depending on the nanofabrication conditions and the annealing temperature. This is illustrated in Figure 4.12, which displays extinction spectra for two different arrays, which consist of particles with pitches of (a)

230 nm and (b) 270 nm and FWHM of (a) 250 nm and (b) 287 nm. The presence of such additional features means that care must be exercised when examining complex spectra. For example where there is strong light-matter coupling: it is necessary to carefully compare spectra against the reference spectrum for the clean gold nanostructures.

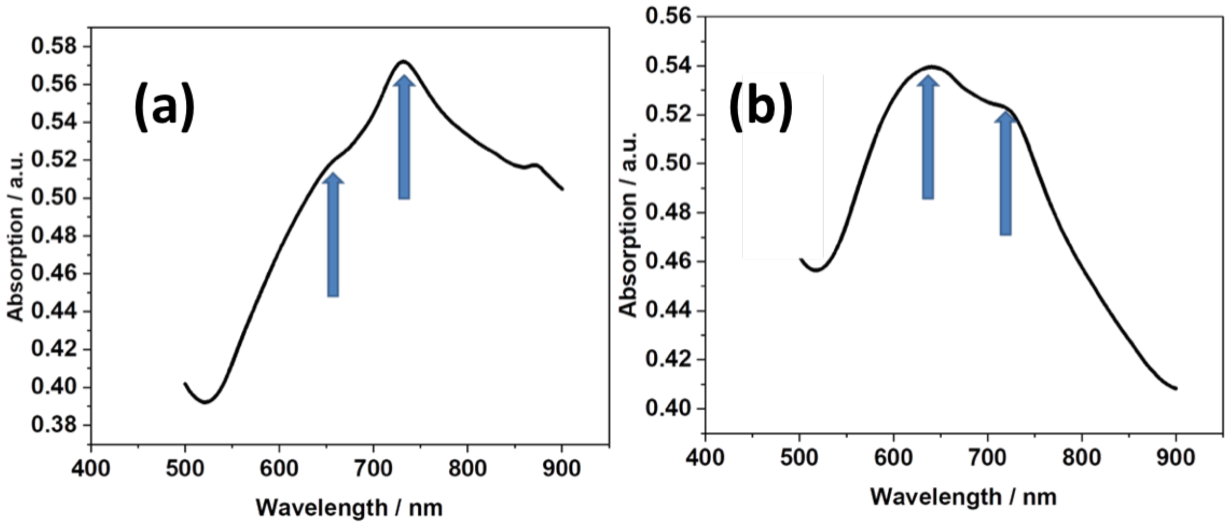

Figure 4.12 **Absorption spectra of two arrays of gold** nano**line** with pitches of (a) 230 nm and (b) 270 nm and FWHM of (a) 250 nm and (b) 287 nm. In each case the extinction spectra exhibit a main absorption band and a small shoulder. The positions of these two features are indicated by arrows.

The relationship between the pitch (the peak-to-peak distance between nanostructures) and the position of the λ_{LSPR} is shown in Figure 4.13. The pitch varied from 220 to 480 nm. The position of the plasmon band was found to become increasingly red-shifted and increased as the pitch of the array increased. The particle size (FWHM) increases as the pitch of the array increases, and this causes a reduction in the energy of the LSPR. The variation in the associated plasmon wavelengths is shown in Figure 4.13.

The resonance wavelength λ_{SPR} of LSPR for gold nanostructures that have been fabricated by the IL technique using two exposures can be tuned by varying size, height, and spacing. The dependence of λ_{LSPR} on the pitch shown in Figure 4.13 is consistent with published data by Vazquez-Mena et al.[302] who prepared samples by evaporating gold through a stencil mask. The

RI sensitivities obtained by Vazquez-Mena et al. were m = 179 nm/RIU for nanodots with spacing S = 300 nm, m = 93 nm/RIU for S = 200 nm, and m = 30 nm/RIU for S = 100 nm.

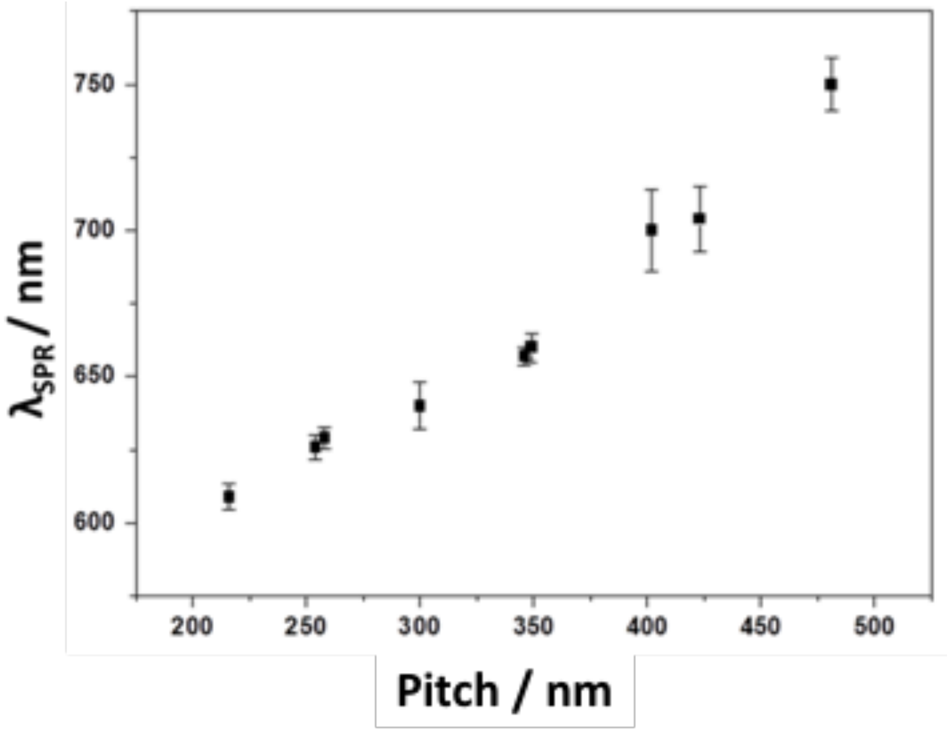

Figure 4.13 The variation in λ_{SPR} as a function of the pitch (the peak-to-peak distance between nanostructures). ϕ varied between 20° and 90° to achieve a range of pitch from 230 nm to 473 nm.

4.2.6 Refractive index sensitivity (RIS)

Adsorption of molecules onto gold surfaces causes a change in the local refractive index, which in turn yields a change in the measured energy of the plasmon band. In several varieties of plasmonic sensors, these red shifts in the position of the plasmon band are measured and used for analytical purposes. The plasmon band will shift as a function of the refractive index of the medium. The relationship between λ_{LSPR} and the refractive index of the medium, *n*, is,[119]

$$\boldsymbol{\lambda_{max} = \lambda_p\sqrt{2n^2+1}} \qquad \textbf{4.1}$$

Where λ_{LSPR} is the wavelength corresponding to the plasma oscillation. At optical frequencies, the relationship between the LSPR wavelength and the refractive index is approximately linear.[119] Thus, the refractive index sensitivity m, defined as $m = \lambda_{LSPR} / n$ where n is the refractive index of the mediums used as a convenient figure of merit and is determined from the slope of a plot of λ_{LSPR} against n for a series of liquids.

The UV-visible absorption spectra were measured for three replicate gold nanostructure arrays with a pitch of 360 ± 30 nm in media with different refractive indices, including aqueous NaCl and a variety of organic liquids including ethanol, dimethyl formamide, acetone, and mixtures of toluene with ethanol and methanol. Representative spectra are shown in Figure 4.14 (a) which shows that the wavelength at which the plasmon band was observed varied significantly in each of the different liquids. The dependence of λ_{LSPR} on the refractive indices of this set of test liquids is shown in Figure 4.14(b). A straight line was fitted to the data by linear regression to enable the determination of the refractive index sensitivity. The error bars are calculated as the standard error of the data. Based on the fitted line, the refractive index sensitivity (the slope of the fitted line in Figure 4.14(b)) was 87 nm per unit of refractive index (87 nm RIU^{-1}).

The same method was employed to determine the refractive index sensitivity of a series of samples fabricated with different sizes (FWHM) and these results are shown in Table 4.1. The refractive index sensitivity increased with the nanoparticle size which is consistent with expectations based on published literature.[303]

Larger nanoparticles tend to have high sensitivities; however, multipolar excitations and radiative damping broaden their peaks.[119]

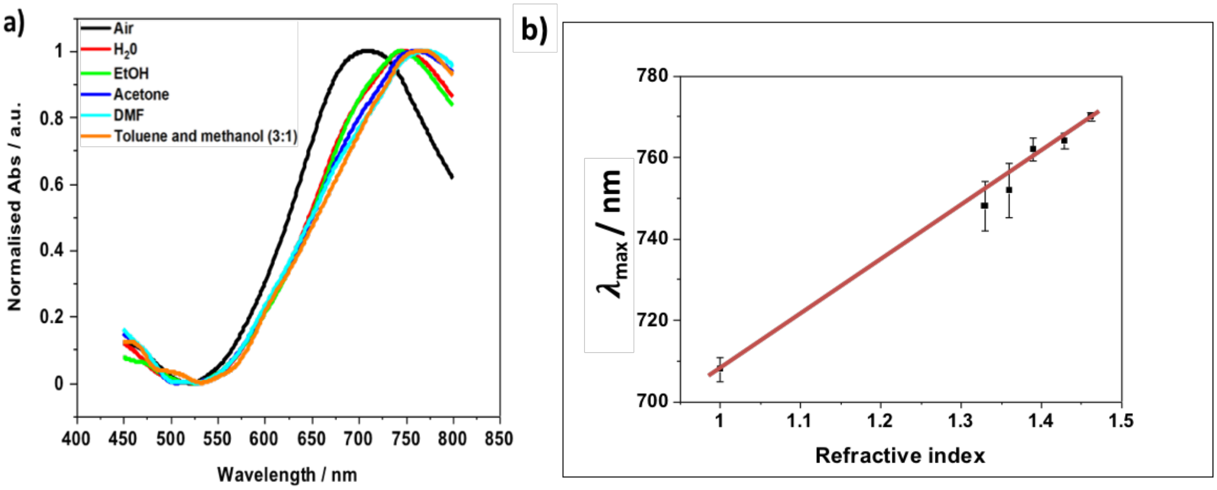

Figure 4.14 (a) UV-vis absorption spectra of Au nanostructures with a pitch of 360∓30 nm and a FWHM of [330] nm, fabricated in a double exposure process with ø= [25]were measured in media with different refractive indexes (NaCl at different concentrations and other solutions such as EtOH, DMF, Acetone, a mixture of toluene with ethanol and MeOH). (b) Variation in λ_{SPR} as a function of the refractive index for three replicate samples with a pitch of 360 ± 30 nm. The measurements were repeated in triplicate for each sample.

Table 4.1. The effect of particle size on the refractive index sensitivity/RIU. Different annealing Au nanoarrays samples reported the sensitivity to UV-vis as measured in media with a different refractive index.

Size of the nanoparticle (FWHM) / nm	Refractive index sensitivity / nm RIU^{-1}
280	87
300	97
321	104
329	117
330	131

4.2.7 Protein adsorption onto arrays of gold nanostructures

One of the primary objectives of this study concerns the development of a new approach to the fabrication of chip-based arrays of gold nanostructures for biological sensing. A key question concerns the sensitivity of the arrays to the binding of biological molecules. When proteins adsorb onto the surface, the local refractive index changes which results in a shift in the energy of LSPR, the magnitude of which is determined by the number of adsorbed biomolecules; therefore, to calibrate the sensitivity of the arrays, this research examined the adsorption of streptavidin. Streptavidin is a model protein which is used to quantify the sensitivity of the LSPR to protein adsorption. It is a protein that is employed in biosensor design because many antibodies are conveniently modified in a site-specific way to introduce biotin as a linker which facilitates binding to adsorbed streptavidin with a controlled presentation. SAMs afford a flexible platform to modify the surfaces of metals and metal oxides. Protein immobilization is one of the most important applications of the modified SAMs. Non-specific adsorption (NSA) is a constantly recurring issue which negatively affects biosensors by making them less sensitive, less specific, and less reproducible.

Streptavidin is a protein formed by the bacterium Streptomyces avidin which has four binding sites for biotin (in common with avidin). Both have been widely used as probes in immunochemical systems, conjugated to antibodies, enzymes, or fluorochromes; however, avidin has a more basic isoelectric point (pI ~ 10.5) than streptavidin (pI ~ 5-6).[304,305]

The adsorption of streptavidin onto gold nanostructure arrays was characterised using UV-vis spectroscopy (Figure 4.15). Subsequently, the arrays were immersed in streptavidin solutions for various times. Following the adsorption of streptavidin, the LSPR peak redshifted by 10.0 nm after an adsorption time of 30 min and 20.0 nm after an adsorption time of 1 hour (see Figure 4.15).

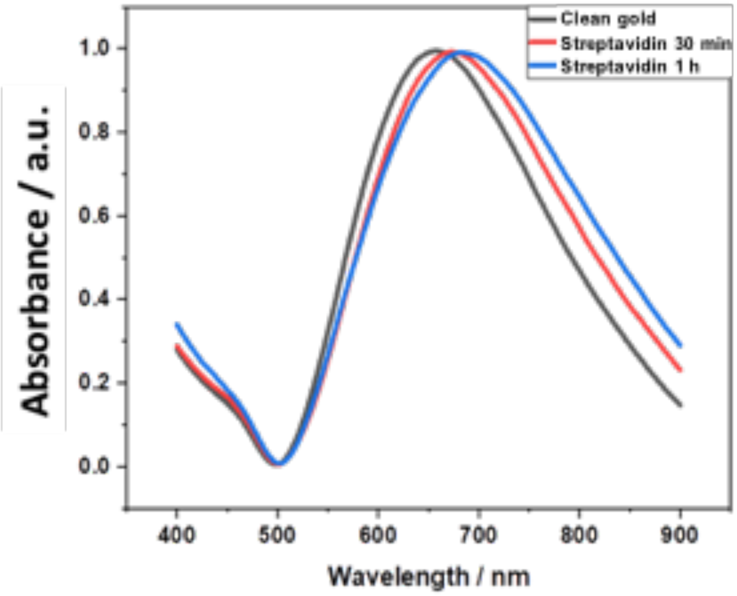

Figure 4.15 λ_{LSPR} extinction spectra of gold nanostructures surfaces (black lines) and (coloured lines) after immersion in a solution of streptavidin for 30 min (red) and 60 min (blue). The features of the gold nanostructures' pitch are 300 ∓20nm, FWHM 270 ∓37 nm, and φ 25°∓2.

Adsorption isotherms were acquired on continuous gold film. The samples were immersed in protein solutions with a range of concentrations and allowed to equilibrate for one hour before the adsorption spectra were collected. Spectroscopic ellipsometry was employed to determine the film thickness. Figure 4.16 shows the variation in the ellipsometric film thickness, proportional to the amount of adsorbate, as a function of the concentration of streptavidin in the solution. Initially, the amount of adsorbate increases rapidly as a function of concentration and approaches a limiting value at a concentration of >700 nM (which corresponds to monolayer formation). The thickness of the layer of adsorbate formed at this concentration (5.5 nm) is in accordance with the expected height of a streptavidin molecule (5.6 nm).[306] Protein adsorption follows Langmuir kinetics,[295] and the behaviour observed in Figure 4.16 is consistent with this. Langmuir kinetics are observed where the adsorbate binds to the surface strongly but where the interactions between adsorbate molecules are much weaker. Consequently, in Langmuir kinetics adsorption ceases the formation of an adsorbate monolayer. Proteins interact only very weakly with each other but are expected to adsorb robustly onto gold surfaces. The equilibrium constant is in agreement with the literature.[307] The Langmuir adsorption isotherm describes the adsorption of molecules onto a solid surface, assuming a finite number of identical sites and no interactions between adsorbed molecules. Figure 4.16 shows variation in the fractional coverage with the concentration of streptavidin. The red line has been fitted to the data using the Langmuir equation:

$$\theta \text{ or } q_e = \frac{bC}{1 + bC} \qquad 4.2$$

Where:

Theta is the fraction of the surface covered by streptavidin. b appears to be about 200 nm, related to the affinity of streptavidin for the gold surface. C is the concentration of streptavidin.

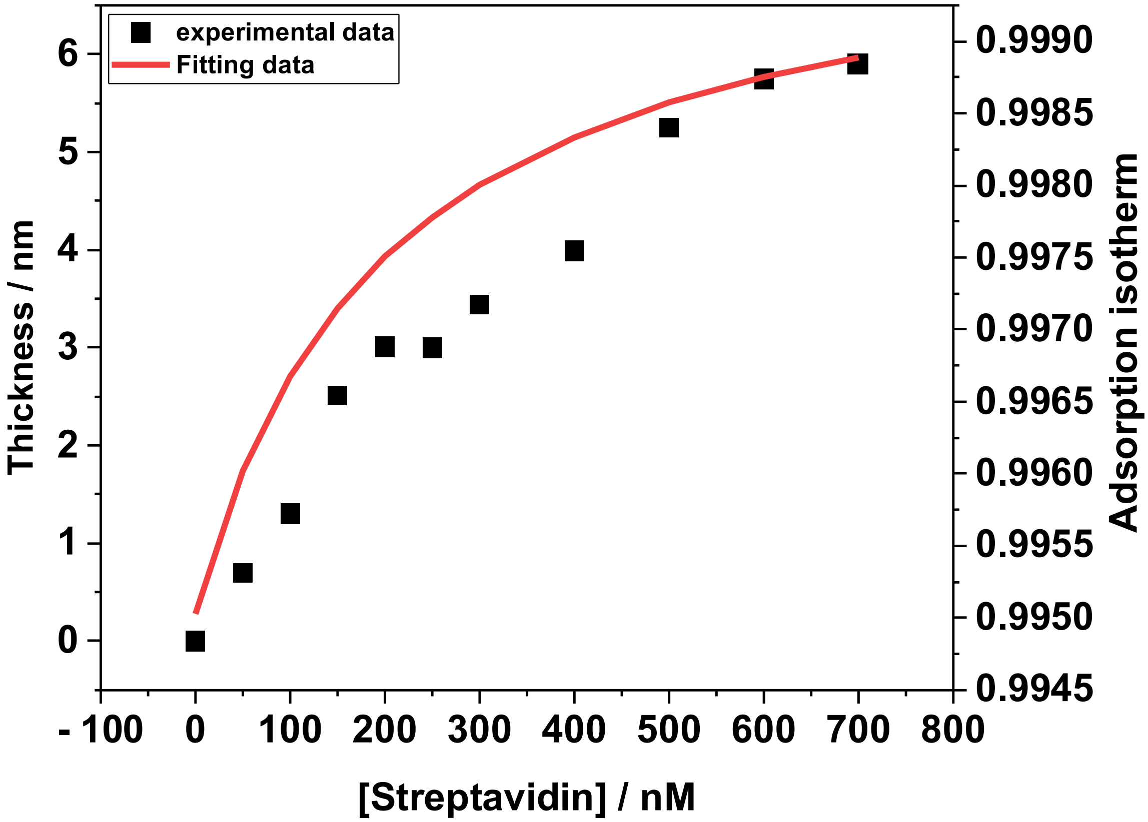

Figure 4.16 Adsorption isotherm for Streptavidin adsorbed on polycrystalline gold film. (black square) The ellipsometric thickness of the streptavidin layer is assumed to be proportional to the amount of adsorbate and plotted as a function of the streptavidin concentration. (red line) Variation in the fractional coverage with the concentration of streptavidin. The red line has been fitted to the data using the Langmuir equation.

For gold nanostructure arrays, streptavidin adsorption was studied by measuring the redshift in the position of the plasmon band (see Figure 4.17). The red shift in the position of the LSPR is proportional to the refractive index change in the vicinity of the gold surface, which in turn is proportional to the amount of adsorbate.[119] Therefore, the plot of λ_{LSPR} against the streptavidin concentration provides an alternative means to measure the adsorption isotherm for the protein. Initially the size of the red shift increases rapidly; however, the rate of increase decelerates as the concentration increases above 400 nM and reaches a limiting thickness. This data suggests that the adsorption kinetics are similar for nanostructured and continuous gold films,[308] and no significant changes were perceived in the extinction spectra of nanostructured gold films when exposed to protein solutions with concentrations in the range 50 nM to 1 M.

At concentrations of approximately 400 nM, streptavidin's binding behavior on the Au nanostructures can be effectively explained using by the Langmuir adsorption isotherm (following the attainment of saturation coverage). Each streptavidin molecule was independently bound to a finite number of identical sites on the gold surface until all the sites were occupied. The system achieved its highest coverage level at 400 nM, implying that the gold nanostructure binding sites were maximally utilized, thereby promoting the optimal streptavidin-substrate interaction.

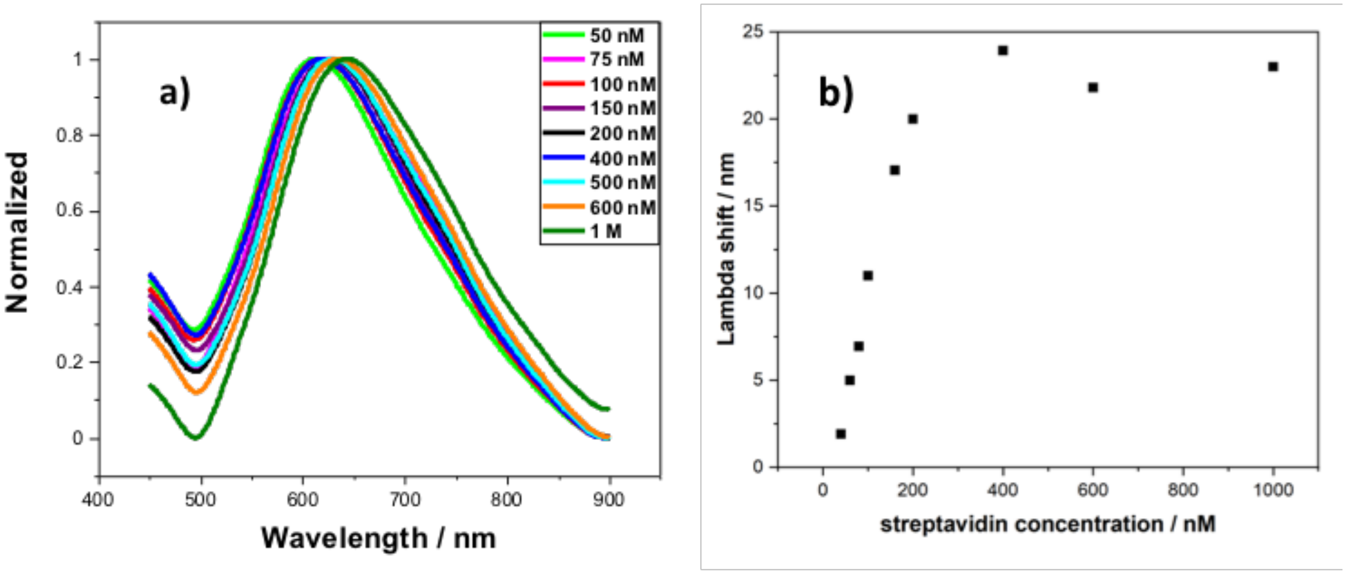

Figure 4.17 (a) Absorption spectra of bare Au nanoarrays following immersion in solutions of streptavidin with different concentrations. b) The dependence of the red shift in the LSPR, $\Delta \lambda_{LSPR}$, as a function of the concentration of streptavidin.

The extinction spectra of Au nanoarrays following the immobilization of streptavidin with different concentrations are shown in Figure 4.17. The plasmon band was observed to become increasingly red-shifted as the concentration of streptavidin increased (see Figure 4.17(b). The variation in Δ_{LSPR} with streptavidin concentration in Figure 4.17 (b) correlates closely with the ellipsometry data contained in Figure 4.16. The amount of adsorbate increased with the concentration of the streptavidin and reached a limiting coverage at a concentration of ~700 nM. Above 500 nM, the plasmon band becomes stable when it reaches the limit of detection which is in agreement with the spectroscopic ellipsometry measurements. The ellipsometric data closely aligns with the LSPR shift and indicates a coverage level of 400 to 500 nM.

Compared with other plasmonic devices, such as gold nanoparticles and nanorods, LSPR sensors exhibit equal or superior sensitivity to traditional plasmonic devices. This is attributed to their high surface-area-to-volume ratio and amplified electromagnetic fields. Performance can be influenced by factors such as particle size, shape, and surface modification. Performance comparisons between LSPR sensors and traditional plasmonic devices for protein adsorption are dependent on experimental conditions and device configurations.

In label-free sensing, streptavidin can be used to anchor a probe antibody in a site-specific manner via biotinylation of the antibody.

To determine the feasibility of using gold nanoparticle arrays in this way, streptavidin functionalized nanostructures were immersed in a solution of biotinylated IgG and the extinction spectra were recorded. A redshift of 17 nm was observed in the extinction spectra following the adsorption of streptavidin; however, following the binding of biotinylated IgG, a further redshift of 15 nm was observed (see Figure 4.18).

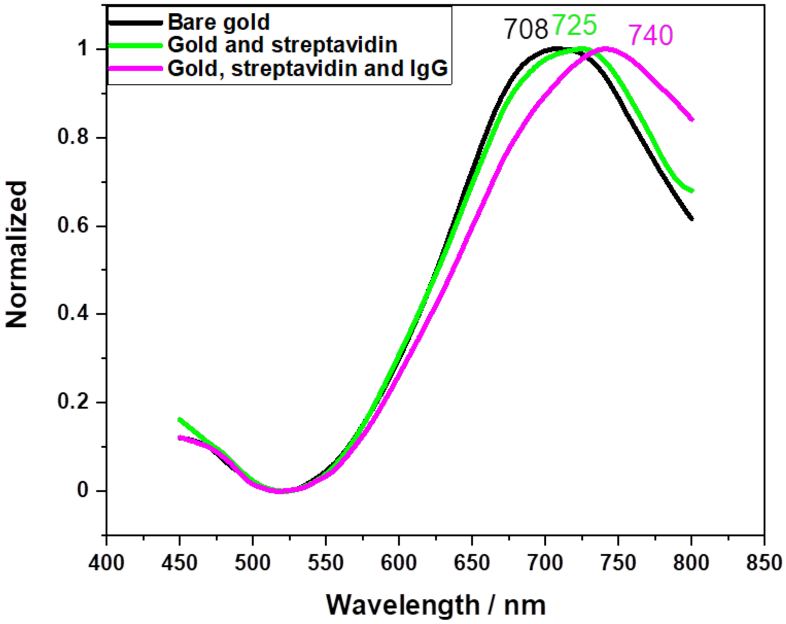

Figure 4.18 The adsorption spectrum of gold (black line) following the addition of immobilized streptavidin (green line) and the after attached IgG (pink line).

When streptavidin adsorbs onto gold nanostructures, it changes the local refractive index on the gold surface which leads to a red shift in the position of the plasmon band.

However, a very different kind of behavior was observed when synthetic light-harvesting Maquette proteins were attached to gold nanostructures. Maquette proteins are synthetic proteins that consist of α-helical bundles that are designed and created to incorporate cofactors that convey specific roles. Figure 4.19 is a schematic diagram of the structure of BT6 maquettes, and the location of the two chlorins.

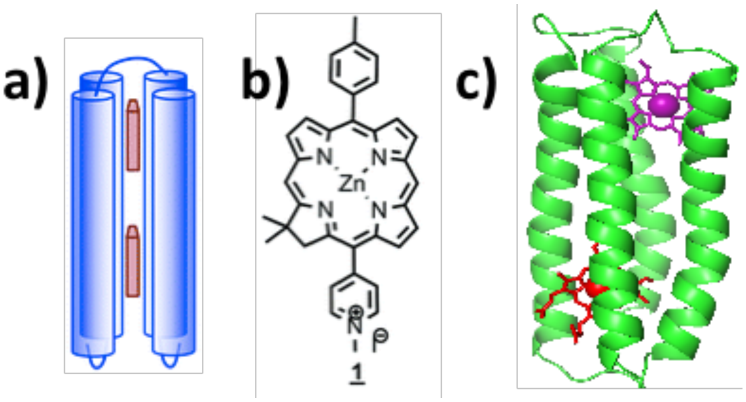

Figure 4.19 (a-b) Schematic diagrams showing (a) the structure of BT6 maquettes, (b) the location of the two chlorins,[309] and (c) maquette design as shown by pigment.[310,311,312]

For example, Dutton et al. designed maquette proteins that bind oxygen to replicate the biological function of myoglobin.[313] They are designed from first principles, with minimal reference to natural protein sequences, and provide an ideal platform from which to address essential questions regarding the relationship between biological structure and function. In this chapter measurements are described for a synthetic light-harvesting maquette protein.

Light-harvesting BT6 maquette proteins containing terminal His_6 tags were attached to gold nanostructures as described in chapter 3.8. These maquettes contain two binding sites for synthetic chlorin (a tetrapyrrole structure with robust photosensitizing properties). The His_6 tag binds strongly to nitrilotriacetic acid functionalised surfaces that have been complexed to Ni^{2+}. These surfaces are prepared by binding aminobutyl nitrilotriacetic acid to aminoundecanethiol SAMs via incubation with a bifunctional linker (glutaraldehyde).

XPS C 1s high-resolution spectra for different surfaces are shown in Figure 4.20. Figure 4.20 (a) shows the C1a spectrum of a SAM of aminoundecanethiol. It is fitted with two peaks, one with a binding energy (BE) of 284.5 eV that is attributed to C−C−C and another with a BE of 286.6 eV that is attributed to C−$\underline{\text{C}}$−N. Aminoundecanthiol SAMs were reacted with GA and Figure 4.20(b) contains the spectrum of the product of this reaction. It is fitted with three peaks: a component at

284.5 eV corresponding to aliphatic carbon atoms; a peak at 286.5 eV attributed to carbon atoms in unreacted amines (C−C−N) or adjacent to the nitrogen atom in the imine group (C−C=N); and a component at 288.1 eV attributed to C− C=O in the free aldehyde group ω to the imine bond. Figure 4.20(c) shows a C1s spectrum of a sample like that in (b) after incubation with ABNTA.

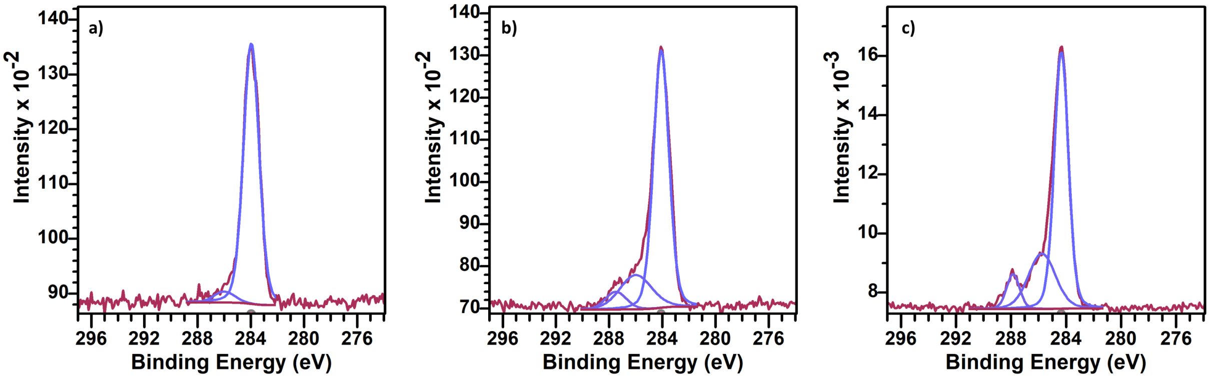

Figure 4.20 XPS C1s spectra of SAMs and Maquette BT6: (a) an aminoundecanethiol SAM of gold, (b) an aminoundecanethiol SAM on gold after reaction with glutaraldehyde, and (c) an NTA-functionalised monolayer.

This is consistent with previous studies regarding aminosilane systems by Xia et al.[314] and previous studies on gold film systems by Lishchuk et al.[309] After the reaction of glutaraldehyde with an AUT SAM, a component was observed at 288.4 eV corresponding to the aldehyde terminal group. The area of this peak was 5.6 at%, compared to a calculated value of 12.5 at% (assuming complete reaction) which indicates slightly less than 50% derivatization of the surface. After the final stage of the surface derivatization process, the attachment of aminobutyl NTA, a carboxylate peak is observed at 289.0 eV, with an area of 1.8 at%, compared to a calculated value of 5.6 at %. Although the overall yield is 32%, it should be noted that surface reactions frequently produce poor yields because of the severe steric constraints and, moreover, the multiple stages of this process. Given that the cross-sectional area of a BT6 maquette is ~4 nm^2, and the efficiency of NTA-His complexation is high, this density of NTA groups should be considered adequate for the formation of a close-packed layer of maquettes.

Figure 4.21 (b) shows the spectra of a clean gold nanostructure array (blue line) and the same structure following the deposition of Maquette BT6 (red line). Additionally, the plasmon peak has shifted to a lower wavelength and split following the adsorption of the protein. The blue line shows the extinction spectrum of clean Au and a significant change is observed following the binding of Maquette. The red line shows that the plasmon band splits to yield new components at 570 and 650 nm. The splitting of the plasmon band is attributed to the strong coupling between the LSPR and the chlorine excitons in the maquette proteins. Surface plasmon polaritons (SPPs) on various nanostructures can exhibit strong coupling to molecular excitons that depend on the plasmon mode volume. A linear combination of the exciton and the uncoupled plasmon resonance yields new states above and below the energy of the SPP mode, and this produces the characteristic splitting in spectra of plasmon energy. Recently, significant interest has been shown in this phenomenon. This coupling may be explained by a Fano theory in which a broad mode (the plasmon mode) is coupled to a narrow one (the exciton) or (by using the coupled dipole approximation).[295]

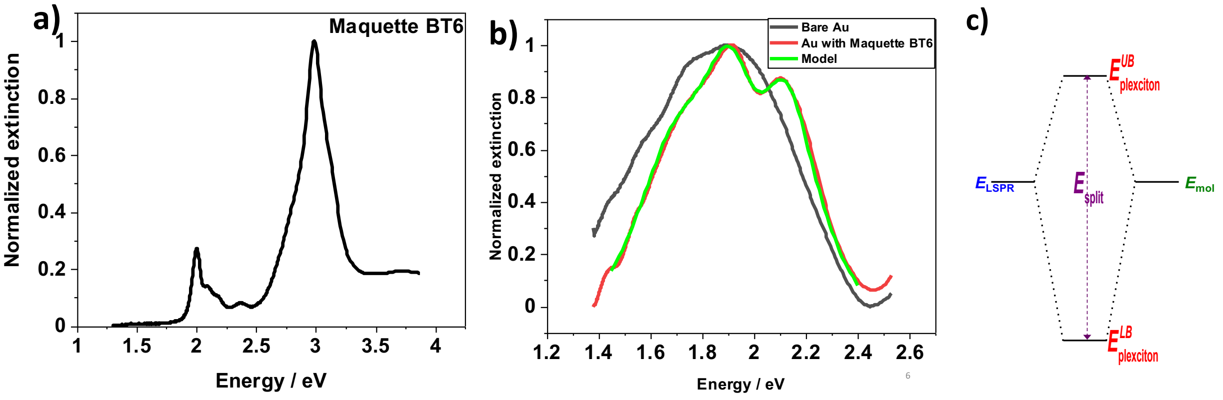

Figure 4.21 (a) Adsorption spectrum of maquette protein BT6. (b) Extinction spectra of a gold nanostructure array before (black) and after (red) attachment of maquette protein BT6. The green line has been fitted to the red data using a coupled oscillator model. (c) Schematic diagram illustrating the linear combination of LSPR and exciton states in strong coupling, to yield two new peaks with energies E_1 and E_2.[309]

In the strong coupling regime, a linear combination of a protein exciton (energy E_{mol}) and the uncoupled LSPR (energy E_{LSPR}) yields new states above and below the energy of the LSPR (with energies E_1 and E_2) giving rise to the splitting of the main plasmon resonance (Figure 4.21 (c)). Plasmon-exciton coupling was modelled with a classical model based on two coupled harmonic oscillators.[295]

To establish whether the coupling energies obtained by fitting the model to experimental data are realistic (considering the dipole moments and densities that can be expected), this study relates the coupling energy (E_C) to the microscopic expression for the coupling energy:[315,316]

$$\boldsymbol{E_c \approx \sqrt{\frac{M^2 E_{mol}^2\, N}{\varepsilon_0 \varepsilon_b E_{LSPR}\, V_{LSPR}}}} \qquad \textbf{4.3}$$

where μ is the transition dipole moment associated with each of the N dipoles within the LSPR mode volume V_{LSPR}, ε_o is the permittivity of free space, ε_b is the relative permittivity of the background medium (in case one, the medium is air with an ultrathin protein layer). Using this expression, and the values for E_C, E_{mol} and E_{LSPR} γ_{LSPR} obtained from the earlier modeling and dipole moments provided by the literature, this study established the basis for further research.[317,318]

The robust correlation between the model and the experimental data (see Figure 4.21) facilitated the determination of the energies of the coupled modes. The energies of the two plexcitonic states were found to be 2.03 eV and 1.69 eV and the coupling energy was found to be 2.01 eV. For natural photosynthetic light-harvesting complexes, coupling energies were found to be in the range of 0.19 eV (dependent on the type of light-harvesting complex and its pigment composition).[295]

To determine whether a system is in the strong coupling regime, several criteria are employed.[295] When the linewidths of the modes are similar, the coupling energy (E_C) must be nearly equal to, or greater than, the average of the linewidths of the two modes/oscillators for normal mode splitting (Rabi splitting) at resonance to be observable (modes 1 and 2). However, it should be noted that this is a wide-ranging criterion as the visibility is dependent on how the linewidths are shaped. A double-peak structure (on and slightly off-resonance) is more noticeable when there is one large and one smaller linewidth and, on occasions, the condition. $Ec \geq \sqrt{\gamma_1 \gamma_2}$ (where γ_1 and γ_2 are the line widths of the plasmon mode and the exciton) is applied as a guide. In this instance, it is crucial to take into consideration the fundamental standard for strong coupling: $E_c \ \geq \frac{1}{2}\ (\gamma_1 - \gamma_2)$. By doing so, it is ensured that the word describing the separation between two modes at resonance $\sqrt{E_c^2 - \frac{1}{4}(\gamma_1 - \gamma_2)^2}$, remains true, and two distinct normal modes exist.[295,104]

4.2.8 Stability

The research evaluated the feasibility of cleaning and reusing gold nanostructure arrays. Following the adsorption of streptavidin, the arrays were immersed in cold piranha solution for 4 to 7 min, rinsed, dried, and re-used. To investigate the effect of the cleaning procedure on the nanoparticle properties, extinction spectra were collected. Figure 3.22 contains representative spectra which reveal only a minimal alteration in the position of the plasmon band. The extinction spectra displayed in Figure 4.22 show a blue shift of less than 4 nm (from λ_{LSPR}=617 nm to λ_{LSPR}=613 nm) between a fresh fabricated sample and a sample that has been reused 24 times. Additionally, an AFM analysis of the reused samples indicated small alterations (less than 1%) in the height, width, length, and spacing of fabricated gold nanodots.

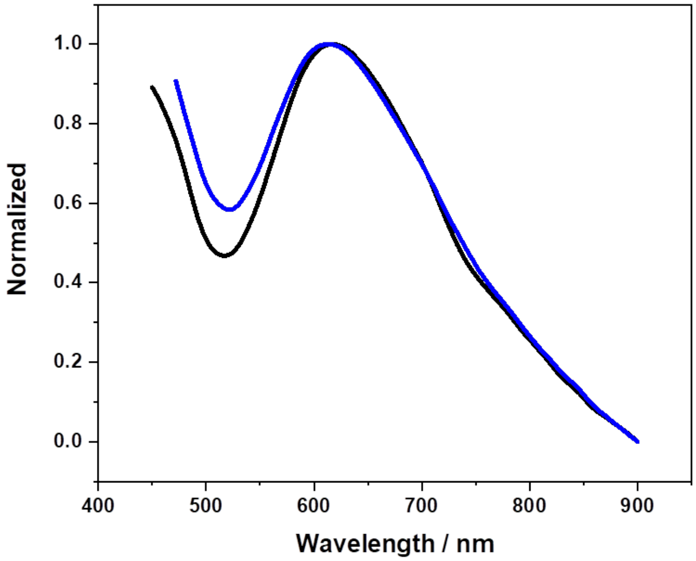

Figure 4.22 The extinction spectra of a newly fabricated sample (black line) and the same sample after multiple uses (blue lines).

SAMs of ODT on 20 nm gold films were patterned by exposure to UV-laser (244 nm) at a power per unit area of 5.9 mW on the sample for 22 min during the first exposure, and 12 min during the second exposure with an angle of 30° between the two exposures. The sample was etched by a solution of cysteamine (0.2 mol) in 4% ammonia in ethanol for 12±1 min. The sample was functionalized with different dyes. After storing this sample for over 1 year in EtOH, it was characterized again by AFM (see Figure 4.23(b)) and the images were compared with those of the as-prepared films (see Figure 4.23(a)) which confirmed that the gold nanostructure has not undergone any significant change (as illustrated in Figure 4.23). AFM topographical images with cross sections of Au nanorods in Figure 4.23 show no change in the morphologies of the nanolines after storing and re-functionalization with different dyes. Gold nanostructures were found to remain stable after storing in EtOH for up to 1 year.

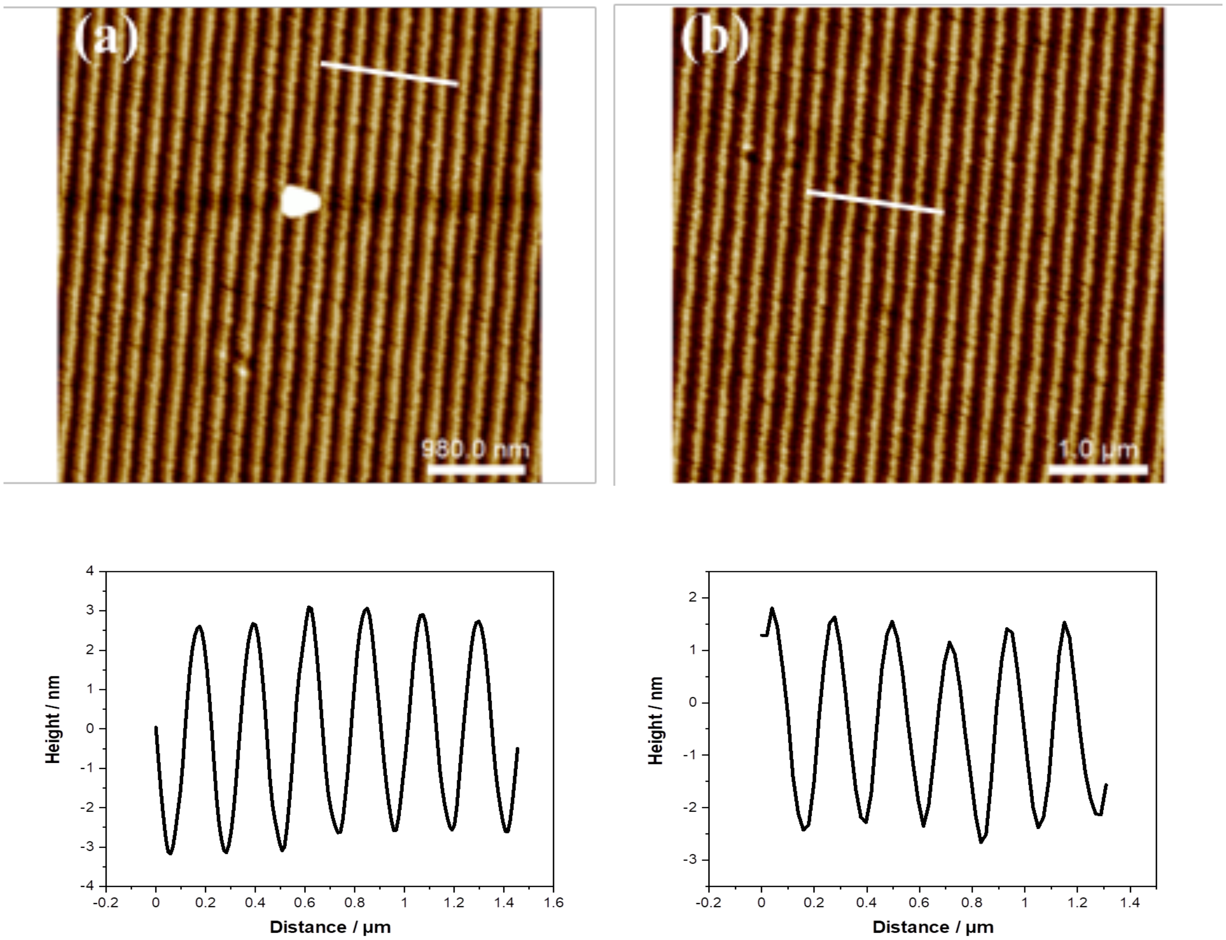

Figure 4.23 AFM topographical images and cross sections of gold nanolines (a) after preparation and (b) after being stored for over 1 year.

4.2.9 Creating near-IR active nanostructures

The aforementioned results are focused on the visible region of the electromagnetic spectrum; however, for some applications, it would be advantageous to be able to fabricate nanostructures arrays that possess plasmon resonances in the near-infrared (NIR) region of the spectrum, i.e. the wavelength range of 600 to 1,000 nm. Therefore, this study attempted to fabricate nanostructure arrays by IL that exhibit efficient strong plasmon resonances at NIR wavelengths.

The samples in Figure 4.24 were exposed using identical conditions to the lithographic process; however, the primer layers were different. The thickness of the gold is around 25 nm, the etching period is 13 min, the angle between the mirror and the sample is 25^{o}, and the rotation of the sample is 90^{o}.When Cr was used as an adhesion layer (Figure 4.24 (a)), the longest wavelength achieved by the LSPR was 750 nm. However, when Ti was employed as the adhesion primer (Figure 4.24 (b)), it was possible to produce arrays whose LSPRs appeared at longer wavelengths of 812 nm. Additionally, the FWHM for sample 4.24 is larger and higher.

NIR-active structures can have a variety of morphologies depending on the materials and manufacturing processes employed. The previous discussion focused on nanoparticles, specifically gold on Cr or Ti acting as an adhesive primer. Nonetheless, nanorods, nanoshells, nanocages, nanostars, and other intricate geometries can also be considered NIR-active structures and when considering their surface-enhanced effects and optical characteristics, these structures have particular advantages. These diverse morphologies provide customized surface features and optical qualities that are advantageous for other purposes including drug delivery systems, bioimaging, photothermal therapy, and sensing platforms.

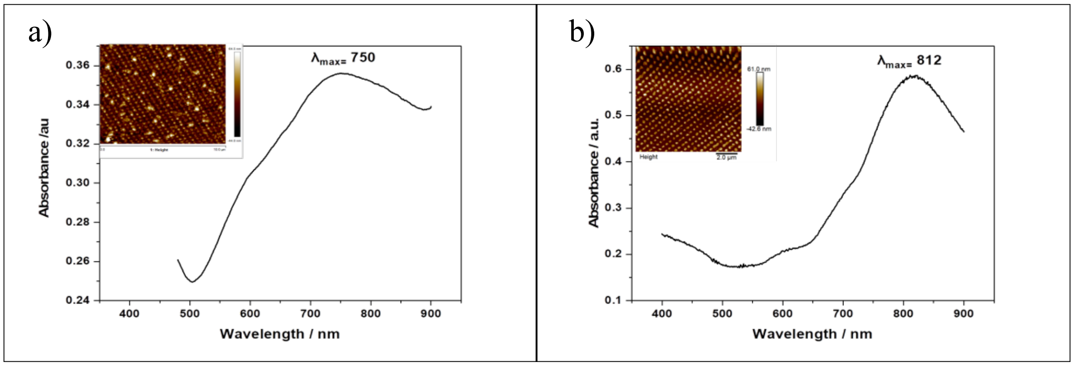

Figure 4.24 Au nanostructures using Cr (A) and Ti (B) as the adhesion primer.

4.3 Conclusions

SAMs of ODT on gold were patterned rapidly, simply, and inexpensively by using a Lloyd's mirror two-beam interferometer over large areas with control of morphology. SAMs of ODT are photo-oxidized by exposure to a UV dose of 30 J cm^{-2}. ODT monolayers were utilized as resists for wet etching by cysteamine solution to fabricate gold nanodots of assorted size and morphologies. From the relationship period = λ/2 sin θ, the angle (2θ) between the two beams that interfere on the sample is the primary parameter controlling the size of the fabricated nanostructure. The geometry of gold nanodots can be regulated by changing the angle of rotation of the sample between the two exposures of SAMs on gold. The absorption spectra indicate that nanorod arrays afford the best-localized surface plasmon resonance. The pitch was between 170 and 280 nm. The particle FWHM was in the range 110 to 370 nm. The period was between 200 and 500 nm. The λ_{LSPR} wavelength of the fabricated nanorods was at ca. 530 and 720 nm. It was found that Maquette protein on gold nanodots provides red-shift of LSPR wavelength 13.0 nm and 18.9 nm, respectively in the λ_{LSPR} extinction spectra, and yielded a splitting of the plasmon band.

Additionally, this research used streptavidin on gold nanostructures which provided a red-shift in the λ_{LSPR} wavelength of 17.0 nm, and IgG on the nanostructures provided a red-shift of 15.0 nm. For the model, the plasmon–exciton coupling is modeled with two coupled harmonic oscillators which align closely with the experimental data and enables the extraction of the exciton energies. The fabricated gold nanostructures are very stable, reusable (more than 24 times), and can be stored for more than six months.

5. Growth of stimulus-responsive polymers from arrays of gold nanostructures

5.1 Introduction

Stimulus-responsive (smart) surfaces are attractive for numerous applications because they enable the regulation of a variety of properties such as wettability, stiffness, biocompatibility, friction coefficients, and specific binding. For example, smart materials have been used in the design of nanoparticles for applications in drug delivery and solar cells.[251] In the presence of either lysozyme or bovine serum albumin, Rosen et al.[319] demonstrated that cysteine-functionalized silica nanoparticles are resistant to protein fouling (BSA). The reversible adsorption and desorption of nanoparticles or proteins by pH manipulation, as demonstrated by Jiang and co-workers, is a second potential use for such brushes.[320] The superior in vitro and/or in vivo anti-cancer efficacy of these dual and multi-stimuli responsive polymeric nanoparticles has been demonstrated by reports regarding their unmatched control over drug distribution and release. Dual and multi-stimuli responsive nanoparticulate drug formulations demonstrate enormous potential for targeted cancer therapy due to their programmed site-specific drug delivery characteristic. For instance, pH-sensitive nanoparticles have been designed and developed to release drugs in the tumour and/or endo/lysosomal compartments by taking advantage of the slightly acidic environments in cancerous tissues (pH 6.5-7.2), endosomes (pH 5.0-6.5), and lysosomes (pH 4.5-5.0) as compared to the physiological pH of 7.4 in blood and normal tissues.[321,322] According to research, conformal, percolating metal nanoparticle electrodes can modify silicon microwire-based solar cells. The proposed technique employs a thin polymer brush as a guide for forming the metal nanoparticle electrode layer. Due to the plasmonic scattering capabilities of the metal nanoparticles, the resulting films can operate as both an electrode and a light-capture enhancer.[323,324]

Polymer brushes synthesized by the grafting-from method including living radical polymerization techniques such as atom transfer radical polymerization (ATRP), have been used in the preparation of polymer films with controlled thicknesses of up to several hundred nanometres on either planar or colloidal substrates. Polymer brushes are dense polymer films attached to a solid surface and are prepared either by solution phase synthesis of a polymer that is subsequently attached to a surface (grafting to) or by growth from a surface-bound initiator (grafting from), (as detailed in Chapter 2, Section 2.9.2).[252,253,254] Polyelectrolyte brushes have attracted interest because of their stimulus-responsive character. Several recent studies have considered polyacid and polybasic stimulus-responsive polymer brushes, which change their behaviour with pH and ionic strength.

For example, at basic pH levels, polyacid brushes become anionic leading to electrostatic repulsion between chains which causes increased swelling of the polymer and leads to an increase in height.[255,256] The responses of poly(acrylic acid) brushes to such changes have been investigated, and established a threshold at pK_a (pKa describes a molecule's acidity and measures acid strength by how tightly a Bronsted acid holds a proton). Above this limit, swelling was observed whereas below this limit, collapse typically occurs.[325] Both atomic force microscopy (AFM) and ellipsometry have been applied to poly(methacrylic acid) brushes, enabling their pH response to be observed as capable of switching between collapsed and stretched. Similar responses have been shown in typical polybase brush materials, such as poly(2-(diethylamino)ethyl methacrylate) (PDEAEMA)[326] and poly(2-(dimethylamino)ethyl methacrylate) (PDMA).[327,328]

Zwitterionic polymers are highly resistant to biological adhesion, resisting protein adsorption, cell adhesion, and preventing biofilm formation. Minimal fouling is observed for poly(sulphobetaine methacrylate) (PSBMA) and poly(carboxybetaine methacrylate) (PCBMA) brushes when applied as grafts to glass slides.[329] Zwitterionic brushes also display pH-responsiveness, although the pH dependence is not considered a universal trait, with some, such as PSMBA and PMPC exhibiting no change whereas some substances such as poly (carboxybetaine methacrylate) transition to polyelectrolytic behaviour when pH is reduced.[273,330]

Comparatively few authors have considered amino acid side chain branching polymers. Ionic transport mediation has been conducted using pH variation across a silica substrate activated using surface-initiated radical polymerization to grow cationic poly(methacryloyl-L-lysine) brushes. Liu et al. employed surface-initiated photoinitiator-mediated polymerization (SI-PIMP) to create zwitterionic poly(serine methacrylate) (PSerMA) brushes, which were grafted onto a planar gold substrate to test its potential as an anti-biofouling material.[273] The most notable recent publication regarding this area involves the application of 3- or 5-step protocols to a pair of novel amino-acid-based methacrylic monomers to produce polycarboxybetaine brushes.[296] pH- responsive polymer brushes are widely used in biomedical and engineering applications. Poly (cysteine methacrylate) (PCysMA) was prepared by Alswieleh et al.[266] who noted that the polymer was highly resistant to biofouling and provided effective support for lipids. A commercial methacrylate-acrylate precursor bilayer was coupled to cysteine using a thia-Michael addition, providing a simple and inexpensive method for CysMA synthesis at multigram scale (Figure 3.9 in experimental Chapter 3, Section 3.9). This protecting group chemistry free process operates at a multigram scale and notably, only requires water as a solvent. Effectively, this guarantees the availability of a cost-effective zwitterionic polymer brush system, which compares favourably against extant methods such as PMPC. AFM and ellipsometry were employed to monitor the stimulus-responsive behaviour of PCysMA brushes grown on gold nanostructures and gold substrates using ATRP method which facilitates an assessment of any alterations in pH and ionic strength.[296]

In this chapter, the stimulus-responsiveness of PCysMA brushes grown from gold nanostructure arrays is investigated. Gold nanostructures were functionalised to introduce surface-bound initiator species, and the brushes were grown using surface-initiated atom transfer radical polymerisation and the resulting zwitterionic brush nanostructures were characterised to determine their pH-responsiveness. Brushes with dry thicknesses in the range of 5 to 26 nm were prepared and characterised in solutions with low pH (<2) and very high pH (>12). The influence of such brush films on the extinction spectra of gold nanostructure arrays was measured to determine whether such functionalised gold nanostructures may have utility in the measurement of pH.

5.2 Results and Discussion

The chemical structure of the purified CysMA monomer was confirmed by 1H and 13C NMR spectroscopy, mass spectroscopy, and elemental analyses.

NMR

1H NMR (400.13 MHz, D_2O, 298 K) δ (ppm): 1.79 (s, 3H, $-CH_3$); 2.60-3.11 (m, 6H, $-SCH_2-CH_2-COO-$, $-S-CH_2-CH(COO-)NH^{3+}$); 3.73 (m, 1H, CHOH); 3.80 (m, 1H, $-CH(COO-)NH^{3+}$), 4.10-4.40 (m, 4H, -CH2-CHOH-CH_2-); 5.65 (s, 1H, vinyl), 6.10 (s, 1H, vinyl).

13C NMR (400.13 MHz, D_2O, 298 K) δ (ppm): 17.29 ($-CH_3$); 26.25 ($-S-CH_2-CH_2-$); 31.004 ($-S-CH_2-$); 33.78 ($-S-CH_2-CH_2-$); 53.50 ($-CH_2-CHOH-CH_2-$); 65.20, 65.24 (2C, $-CH_2-CHOHCH_2-$); 67.01 ($-CH(COO-)NH^{3+}$); 127.40, 135.60 (2C, vinyl); 169.40, 172.65, 174.00 (3C, carbonyls).

Mass spectrometry

Theoretical 336.17111

Experimental 336.1

Elemental Analysis

Calculated: C: 46.56%; H: 6.31%; N: 4.18%; S: 9.56%

Found: C: 46.33%; H: 6.30%; N: 4.30%; S: 9.57%

5.2.1 Wettability and Contact Angles (CA)

Wettability was studied via contact angles. For PCysMA, the contact angle (CA) is less than 90° which designates the surface as hydrophilic and this is caused by the presence of polar groups such as amines and carboxylic acids. Numerous contact angle measurements were taken from PCysMA samples prepared using polymerization. Figure 5.1 shows the variation in the contact angles of PCysMA films alongside the polymerisation time. The contact angle of the initiator layer was measured at 77˚±.3˚. After 60 s growth of PCysMA, the contact angle was found to have decreased to 59°. This decreased further with additional polymerisation time and attained a limiting value of 27° after 15 min of polymerization.

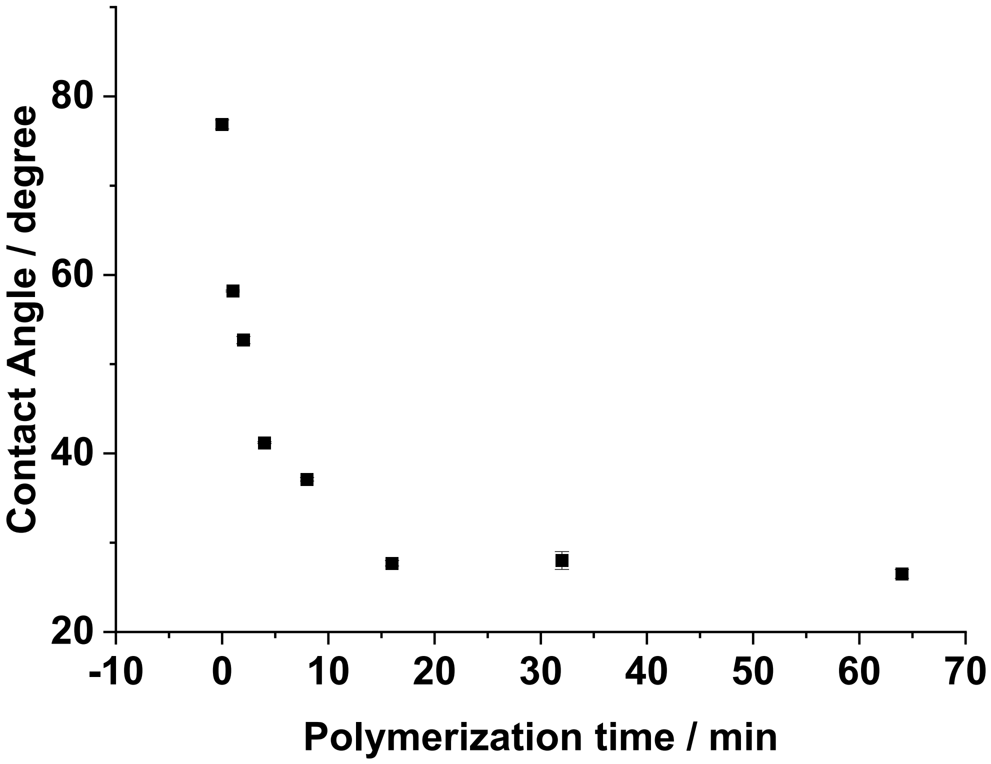

Figure 5.1 Contact angle measurements as a function of polymerization time of a deionized water droplet on a PCysMA on Au substrate. The error bars represent the standard deviation of at least three separate measurements.

5.2.2 Roughness

Measurements concerning the surface roughness provide insights regarding the polymerization reaction: well-controlled ATRP should give rise to smooth film with low roughness, whereas poorly controlled or very rapid polymerization may yield film with higher roughness. Measurements of surface roughness may also be employed to calculate the skew and kurtosis parameters. Skewness is a method for measuring the size of the two tails when compared to each other while kurtosis is used to calculate the total size of two tails and measure how likely it is that the tails will occur. The value is frequently compared with the kurtosis of the normal distribution. To examine surface roughness, this study obtained the AFM topographical images for unpatterned PCysMA brushes and the gradual change in brush roughness as a function of the polymerization time (see Figure 5.2). The interpretation of measurements of surface roughness by AFM is based on the hypothesis that the probe tip faithfully traces the peaks and valleys of highly convoluted surfaces. These measurements aimed to determine the existence of a correlation between the roughness of the polymer brushes and the polymerisation time.

Figure 5.2(a-d) contains a selection of representative AFM height images of PCysMA films grown for different polymerisation times. The morphology of the surface noticeably changes overtime: after 1 minute, the surface is covered with comparatively small features; however, as the polymerisation reaction progresses, the dimensions of these features increase. To quantify the change, the surface roughness was measured (Figure 5.2(e)) and the data indicates that, initially, the roughness increases rapidly decelerates and reaches a limiting value after 16 min. The mean thickness of the PCysMA film was measured by SE. The thickness of the polymer brushes was constant at 12.7 ± 3 nm after a polymerisation time of 32 min (as shown in Figure 5.2e). The roughness increased in line with the sample thickness, up to a polymerisation time of 30 min, following which it demonstrated very little change. The roughness of clean gold was measured as 0.52 ± 0.2nm which is less than the roughness of the polymer film (~ 0.9 nm). Therefore, the roughness of the polymer film correlates with the morphology of the surface grafted polymers, rather than that of the underlying gold substrate.

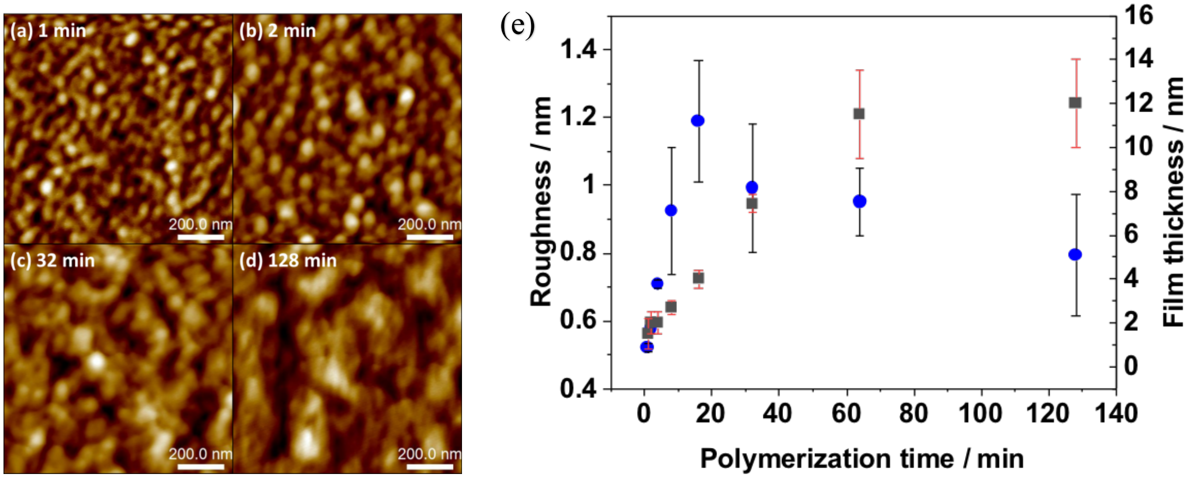

Figure 5.2 (a-d) Height images of PCysMA brushes grown from gold substrates by ATRP for different polymerisation times. (e) Variation in the roughness and the ellipsometric film thickness of PCysMA on gold as a function of the polymerization time.

5.2.3 PCysMA Brush Growth pH-Responsiveness

PCysMA contains a carboxylic acid and an amine group in each CysMA repeat unit which confer pH-responsive behavior on the PCysMA brushes. This complex pH-sensitive behavior has been examined by several studies. Alswieleh et al.[296] who synthesized zwitterionic PCysMA brushes grown from BIBB-APTES-functionalized silicon wafers via SI-ATRP. PCysMA brushes were grown from DTBU-functionalized gold substrate via ATRP, which is recognised to be an effective and convenient technique for the synthesis of dense uniform polymer brushes with controlled thickness.

The polymerization kinetics of fully dense polymer layers were characterized using spectroscopic ellipsometry (SE) which measured brush thicknesses as being between 4 and 33 nm. Using ellipsometry they determined that the thickness of the PCysMA films was 33 ± 3 nm after 270 min. PCysMA brushes exhibit complex pH-responsive behavior. For example, the mean brush thickness increased significantly less than pH 2 and above pH 9.5, as judged by ellipsometry and AFM studies.

In the present work, gold nanostructures were prepared and coated with a monolayer of DTBU. PCysMA brushes were grown from initiator functionalized monolayers (as shown in Figure 5.3); and ellipsometry was employed to establish the brush thickness on the gold substrate. Figure 5.4 shows the variation in the ellipsometric brush thickness as a function of polymerisation time. Gold films were brominated by using DTBU, PCysMA brushes were grown from these initiator-functionalized gold substrates via ATRP and the dry brush thicknesses were determined using ellipsometry. Over time, the brush thickness increased to become more stable until it reached the limiting brush thickness of 33 nm in the dry condition. The thickness of PCysMA brushes on gold films collapsed into a mushroom-like structure in the dry condition. The swelling of PCysMA brushes was compared in different media and revealed that in water, the PCysMA brushes are zwitterionic between pH3 and pH9.[296]

Figure 5.4 shows the polymer film thickness as a function of polymerisation time. In a 1:3 mixture of DMF and H_2O, the polymer brushes swell because the surface-grafted polymers become solvated and cause additional steric repulsion between neighbouring chains. There is an additional swelling of 50% for PCysMA brushes in 1:3 DMF: H_2O and these chains also swell in water (relative to dry brushes in air). Any adjustment of the pH to very high or low values yields additional swelling and, at a neutral pH, the chains are zwitterionic. However, below pH 3 the PCysMA brushes on gold film carry a net positive charge and above pH 9 the PCysMA brushes are negatively charged. The charges in these brushes repel each other which causes additional swelling away from the gold surface. The brush thickness increases from 9 nm in the air to approximately 118 nm above pH 12.56 because the carboxylic acid groups become deprotonated, and the brush chains acquire anionic character which causes interchain repulsive interactions that lead to increased swelling. Conversely, at low pH, the amine groups become protonated and the brush becomes cationic. Thus, at low and high pH there is an additional swelling of the polymer brush of approximately 30%.

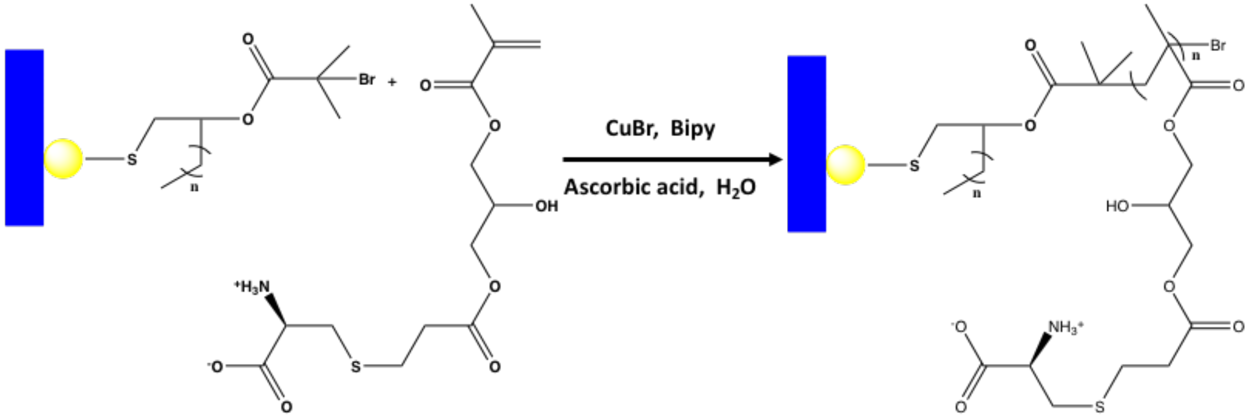

Figure 5.3 Polymer brush growth on gold nanostructures films after initiated the surface DTBU then growth PCysMA.

These findings are consistent with the work conducted by A. Lishchuk.[331] In research conducted by Abdullah M. Alswieleh et al,[296] PCysMA brushes were grown from silicon wafer surfaces using ATRP, and brush thicknesses of roughly 27 nm were attained in 270 min at 20 °C which is consistent with the work presented in this chapter.

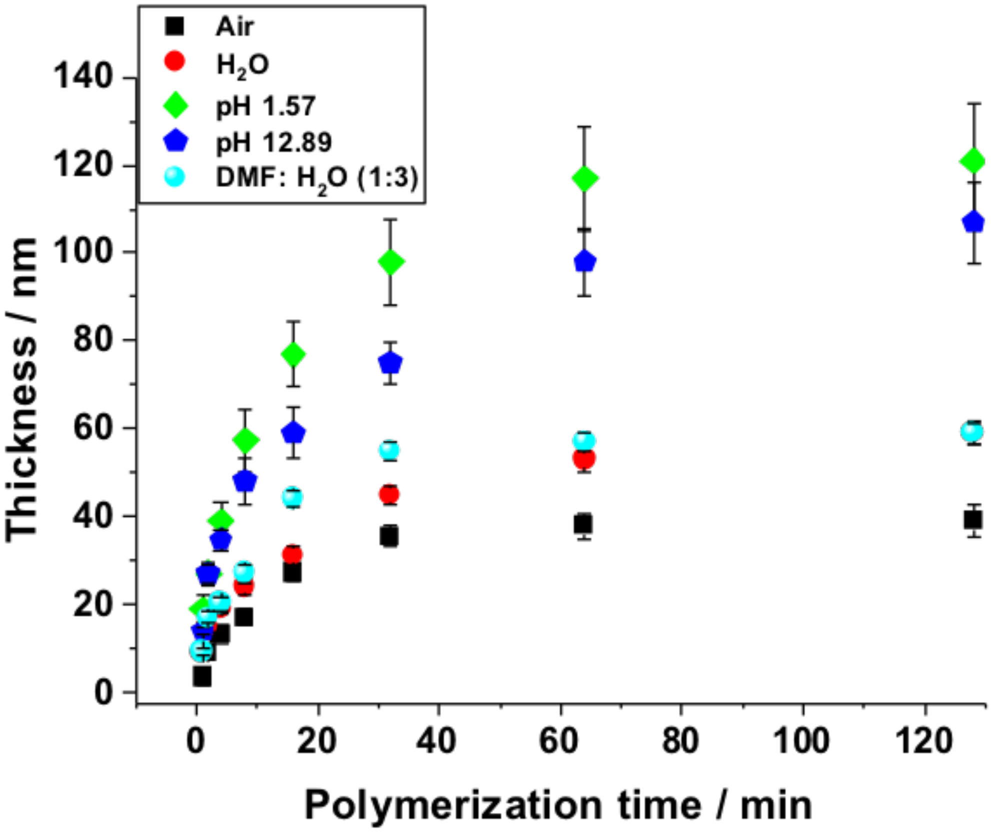

Figure 5.4 The variations in ellipsometric brush thickness with polymerization time for the synthesis of PCysMA brushes via the ATRP method on Au in dry condition and different mediaH_2O, pH 1.57 (HCl), pH12.89 (NaOH) and a mixture of (DMF:H_2O(1:3)). Three measurements were recorded for each brush sample and reported as the mean ± standard error.

It was concluded that the amine groups and carboxylic acid in the CysMA present pH-responsive behaviour on the PCysMA brushes. This is reflected in their diverse behaviour which can be attributed to weak acid or weak base brushes. The carboxylic acid group enters a neutral state while the amine groups continue to be protonated at pH values below their pKa. There are four primary outcomes of the brush layer stretching away from the surface with the intense electrostatic repulsion between neighbouring cationic chains:

a) The amine groups become deprotonated when pH > pKa.

b) The carboxylic acid groups remain in an ionised state.

c) The brushes become anionic and extremely enlarged at basic pH.

d) Interaction between brushes may cause the overlap.

5.2.4 Photopatterning

To verify the kinetic data obtained by spectroscopic ellipsometry, a series of complementary measurements were taken from photopatterned samples. A 2000 mesh copper electron microscope grid was placed on the samples to function as a mask and the sample was exposed to UV light (244 nm, frequency-doubled argon ion laser). In the exposed regions, photolysis of C-Br bonds caused the removal of the Br initiator; however, in masked areas the initiator remained intact. PCysMA was grown from the masked regions of the samples via ATRP, but in the exposed areas, no polymerisation occurred because the Br initiator had been removed. The samples were characterized by tapping mode AFM, and the height difference between the masked and exposed regions was measured for a range of polymerisation.

Figure 5.5 shows AFM height images of a series of samples. In square regions, the initiator has been removed by UV photolysis of C-Br bonds; consequently, polymer brushes will not grow from these regions. However, in the bars, the initiator has been masked during UV exposure; therefore, the Br remains at the surface and ATRP takes place in these regions. The height difference between the square regions (no polymer) and the bars should be equal to the thickness of the surface-grafted polymer film.

For the samples shown in Figure 5.5, the UV dose was varied and maintained a constant polymerisation time of 64 min. The height difference between the masked and exposed regions at doses of 8 and 16 Jcm^{-2} was between 2 and 4 nm. At these doses, the initiator is not fully removed from the exposed regions; therefore, some polymer is observed across the entire sample, albeit with lower grafting density in the square regions. However, if the dose is increased further, the square exposed regions become increasingly depleted in the initiator. At a dose of 32 Jcm^{-2}, the limiting height difference between the masked and exposed regions of 12 nm is achieved; however, the height difference does not increase further at higher doses (such as 64 Jcm^{-2}). The thickness of the polymer film grown from the masked areas is 12 nm which should be equal to the thickness of a brush layer grown from a fully dense layer of initiators. The maximum values between these line sections arise from interference between reflected beams, which slightly reduces the dose in the centers of the square regions.

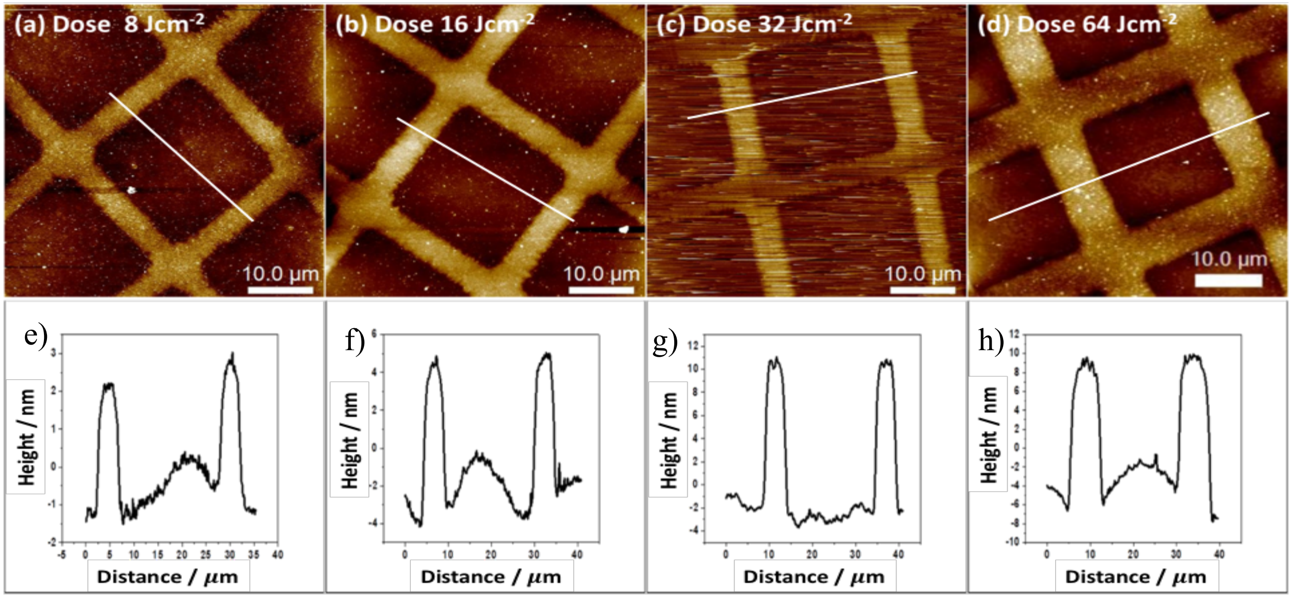

Figure 5.5 The AFM images recorded for micro-patterned initiators in different exposure times (Dose) (a) 8 J cm^{-2} (b) 16 J cm^{-2} (c) 32 J cm^{-2}, and (d) 64 J cm^{-2},then growth PCysMA, and the cross-section for each image (e) 8 J cm^{-2} (f) 16 J cm^{-2} (g) 32 J cm^{-2}, and (h) 64 J cm^{-2}.

The height differences were measured as a function of the polymerisation time. Figure 5.6 shows the variations in height difference between the exposed and masked areas, following the growth of PCysMA as a function of time. The brush height increased by approximately 10 nm after 128 min. The dry samples were imaged by AFM and the height difference was measured between the masked and exposed regions (as shown in Figure. 5.6). The difference between the masked and exposed areas increased rapidly in a brief time and reached a limiting value of 9 nm after 64 min.

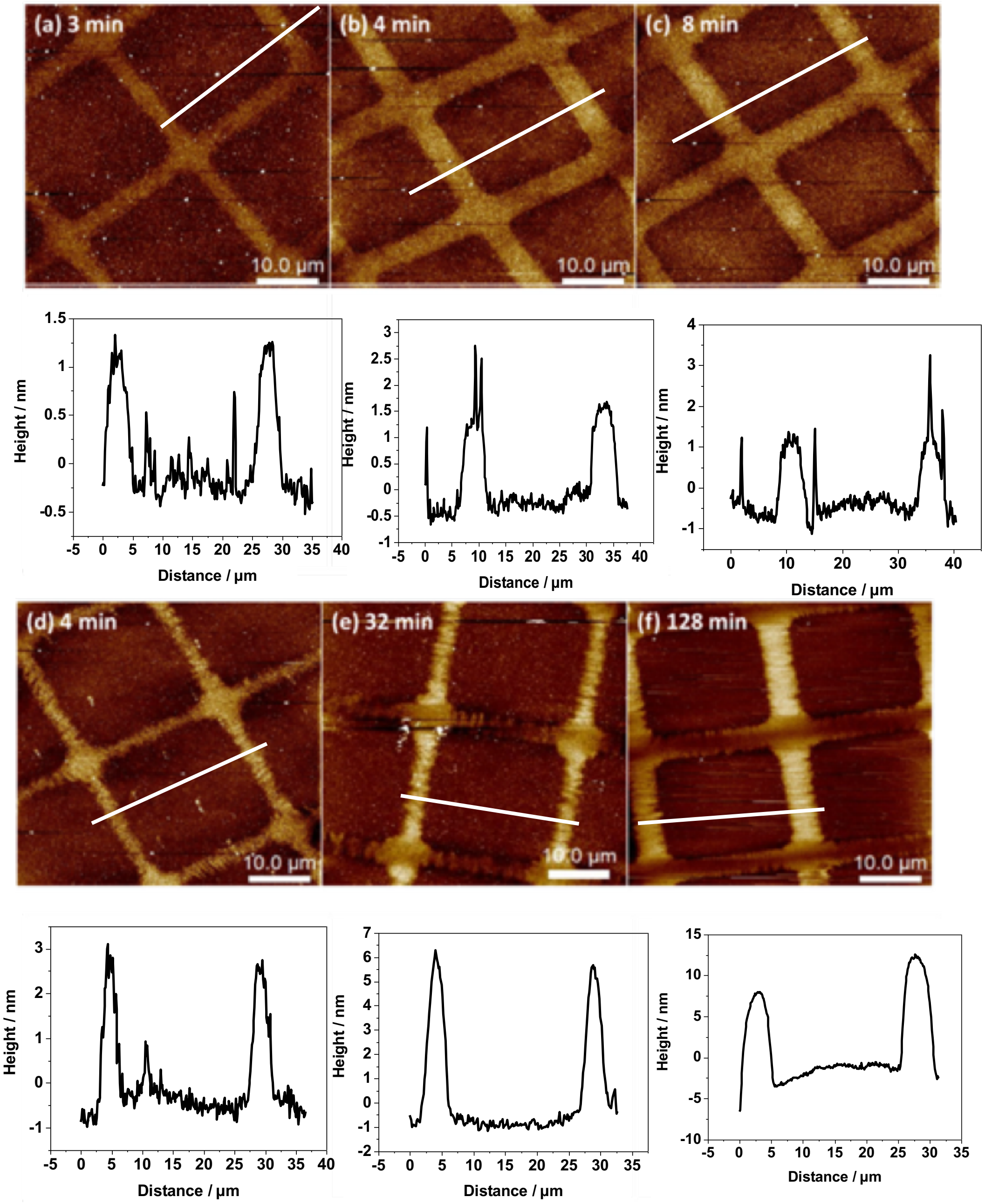

Figure 5.6 A comparison of the AFM produced by the masked and exposed areas when grown PCysMA for different times: (a) 3 min,(b) 4 min,(c) 8 min, (d) 16 min, (e) 32 min, and(f) 128 min.

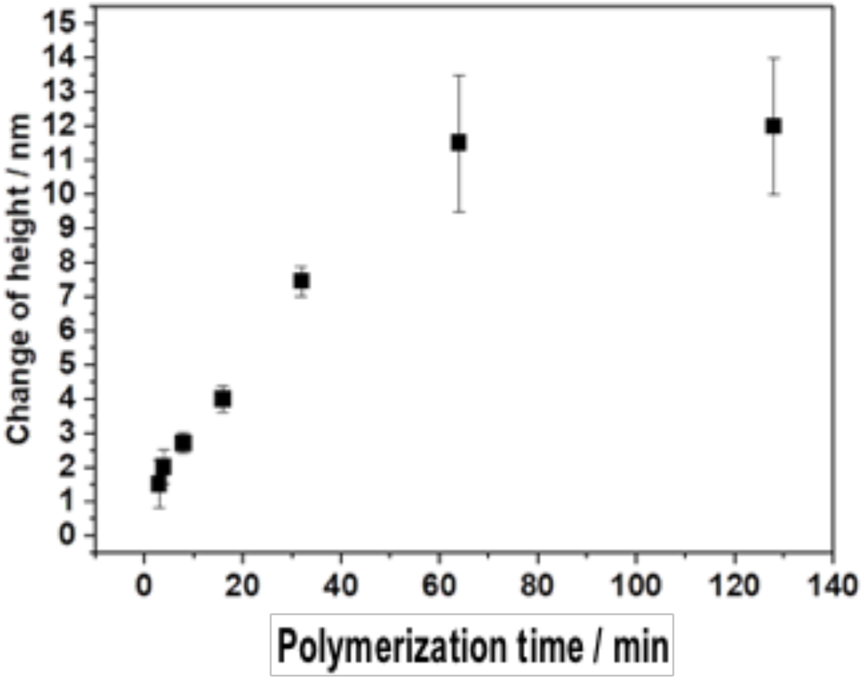

Figure 5.7 The variation of polymer brush height in dry condition as a function of the polymerization time. Three measurements were recorded for each sample and data are reported as the mean ± standard error.

The AFM data (Figure 5.7) indicates that after 32 min the height of the PCysMA brushes reaches a limiting value. Measurements by spectroscopic ellipsometry were broadly in agreement with this, although film thicknesses measured by AFM were slightly smaller than those determined by SE because the films tend to be slightly compressed during imaging even in tapping mode AFM.

5.2.5 Plasmonic analysis of stimulus-responsive swelling of PCysMA brushes

PCysMA displays stimulus-responsive behaviour. In particular, its swelling state fluctuates in response to the pH of the medium (see Fig 5.4). To establish whether plasmonic methods could be used to measure stimulus-responsive behaviour, gold nanostructure arrays were functionalised with PCysMA brushes grown by ATRP and extinction measurements were determined for both dry samples and arrays immersed in different media. Figure 5.8a shows the extinction spectra of clean gold nanostructure arrays in dry conditions and following their immersion in different media (H_2O, HCl, NaOH, and mixture of H_2O: DMF (3:1)). The surface plasmon peak of clean nanoarrays shifts to longer wavelengths when immersed in different media, as was expected given the larger refractive indices for these liquids ($n_{\mathrm{water}} = 1.33$, $n_{\mathrm{DMF}} = 1.43$). Figure 5.8b shows the extinction spectra of arrays after the growth of PCysMA brushes and immersion in the identical media. Notably, there is a shift in the position of the plasmon band after immersion in liquid, relative to the λ_{LSPR} in air.

The shift in the position of the plasmon band relative to λ_{max} for the clean arrays was determined both in air and in liquid as a function of the polymerisation time (Figure 5.8(c)). In agreement with the data presented in Figure 5.4, the magnitude of the shift in the surface plasmon peak increases as a function of the polymerisation time (for all of the liquids studied); additionally, for all of the studied liquids, the size of the shift in λ_{max} is larger than in air. However, while the data in Figure 5.4 indicates a large significant change in the swelling state of the polymer as a function of the liquid medium, the data in Figure 5.8 indicates that this is not accompanied by any corresponding change in the position of the plasmon band.

This is best understood in terms of the changes in the refractive index of the region adjacent to the gold surface. For gold nanostructures, the plasmon mode extends at most a few tens of nm from the surface. The refractive index of air is 1.00, and the refractive index of the polymer is ~1.43. For thin polymer layers, the plasmon mode penetrates through the polymer layer and into the air above it; however, as the polymer film thickness increases, the composition of the material within the plasmon mode volume changes to become pure polymer for the thickest layers (~40 nm thick). As the effective refractive index of the medium increases in correlation with the polymerisation time, there is a progressive red shift in the position of the plasmon band. The shift in the plasmon band of the dry polymer film increases from 5 nm (following a polymerization time of 1 min) to 23 nm (after 64 min polymerization).

For small film thicknesses, the medium above the gold is largely water (n = 1.33); consequently, the plasmon band is red-shifted in liquid relative to the measurement made in air. As the polymer thickness increases, the contribution made by the dielectric properties of the polymer to the refractive index in the region near the metal surface becomes larger. This change in the refractive index leads to an increase in the red shift of the position of the plasmon band and the red shift increases in size as the polymerisation time increases from 5 nm (at 1 min) to 33 nm (at 64 min).

The data in Figure 5.8c shows that for all of the liquids studied, the red shift in the position of the plasmon band is larger for a given polymerisation time than is the case for samples measured in air. However, despite the significant differences in swelling behaviour observed for different liquids in Figure 5.4, the differences in the accompanying red shifts in the position of the plasmon band in Fig 5.8c are modest (compared to the experimental error). This is explained by the fact that although the swelling state of the polymer is very diverse among the different liquids, it is accompanied by only a small change in the refractive index within the plasmon mode volume, because the surface-grafted polymer and the medium have refractive indices that are comparative in size (1.43 and 1.33 respectively). Therefore, the changes in the swelling state are not accompanied by statistically significant changes in the shift of the plasmon band. The red shift in the plasmon band $\Delta\lambda_{LSPR}$ for gold nanostructure arrays after the growth of PCysMA agrees with those previously studied by Lishchuk et al.[331]

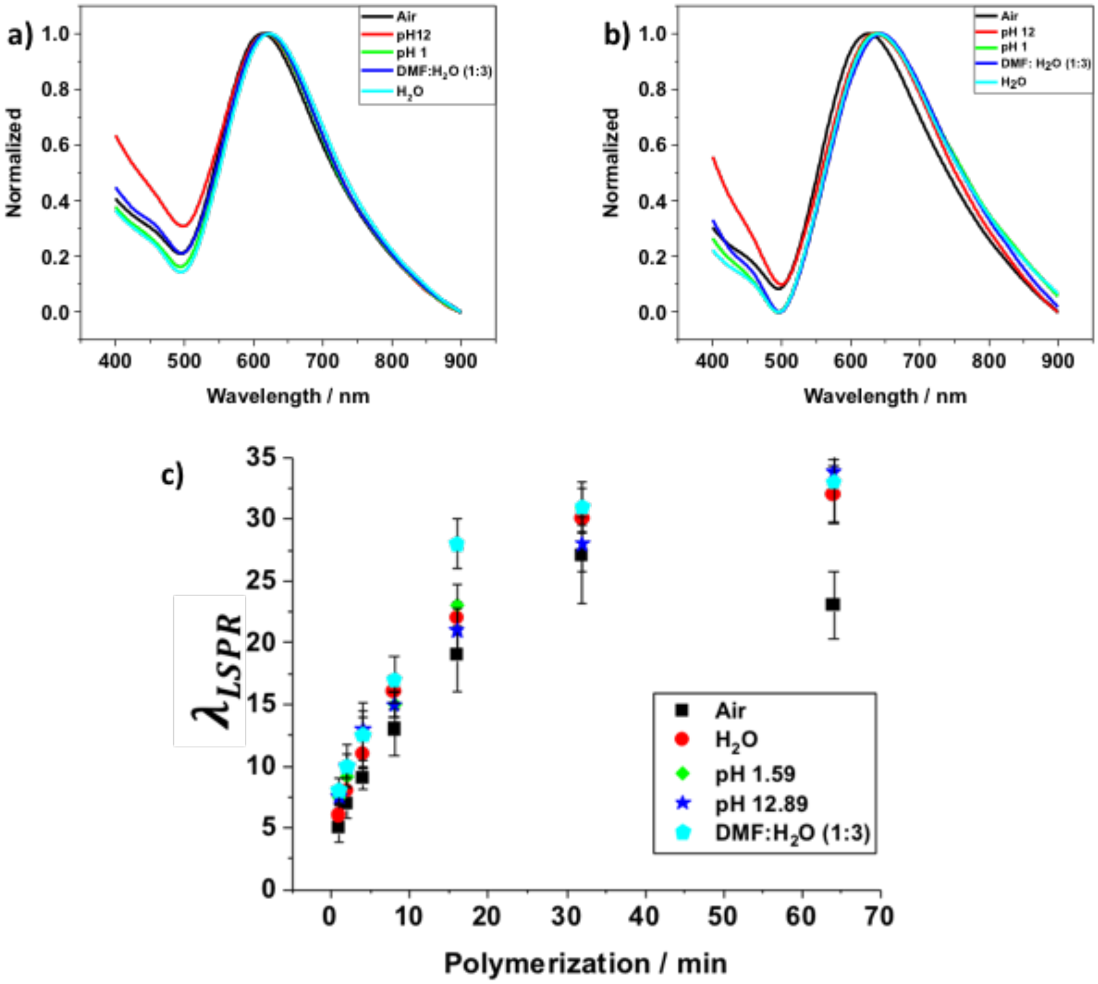

Figure 5.8 (a) Absorption spectra of clean gold nanoarrays in different conditions (dry conditions and following immersion in different media (H_2O, HCl, NaOH, and mixture of H_2O: DMF (3:1))). (b) Absorption spectra of PCysMA on gold nanoarrays in different conditions (dry conditions and following immersion in different media (H_2O, HCl, NaOH, and mixture of H_2O: DMF (3:1))). (c) Lambda shift relative to uncoated sample as a function of the polymerization time of PCysMA brushes.

5.2.6 The effect of free volume brush morphology.

Existing literature, such as the work of Zauscher,[332] indicates that when polymer brushes are grown from nanopatterned initiators, their heights are typically less than those of continuous brush films prepared under identical conditions. It was hypothesized that when surface-grafted polymers are grown from nanopatterned initiators, the free volume of the polymer will be increased. Thus, steric repulsion between neighbouring chains will be reduced, leading to a reduction in swelling perpendicular to the surface when compared to what is observed for a polymer grown from an unpatterned surface with the same grafting density. AFM measurements were made before and after the growth of PCysMA brushes from gold nanostructure arrays and the dimensions of the nanostructures were determined. Subsequently, the impact of the changed free volume on brush morphology was examined in the nanostructures. The mean width of the particle increases as the period is increased, and this was found to be correlated with an increase in brush height because the grafted chains become progressively more extended and fully packed. In a previous study, al Jaf et al[333] reported that the thickness of surface-grafted PCysMA approached that of a continuous brush layer (for nanolines wider than 300 nm); however, for lines narrower than 300 nm, the heights were also reduced and declined with decreasing line width. Structures with a width of 100 nm were only 2 nm high. This study conducted a similar analysis for arrays of particles formed by IL.

Figure 5.9 (a) shows AFM images of clean gold nanoarrays alongside images acquired following growth PCysMA. The height changes can be determined via an analysis of the cross sections contained in these images.

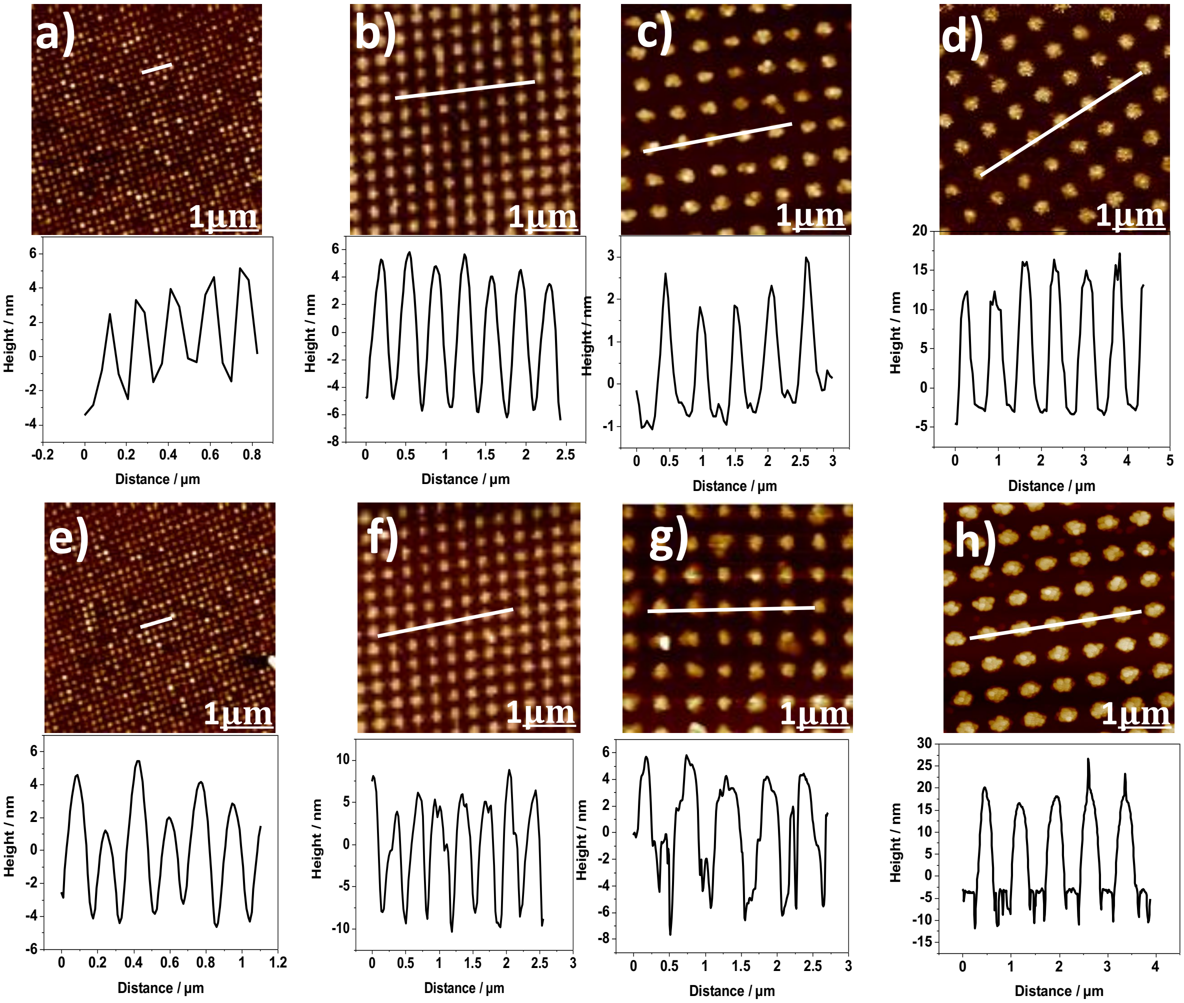

Figure 5.9 Height profiles of gold nano arrays before (a-d) and after (e-h) growth of PCysMA brushes.

Figure 5.10 shows the variation in the heights of the nanostructures after brush growth as a function of the FWHM of the clean gold nanostructures. The heights of the brush-functionalised particles increase as a function of particle size. The largest gold nanostructures had a FWHM of 500 nm and the height after brush growth was four times greater than that of the sample with a FWHM of 100 nm. The polymerisation time was identical for all the arrays characterised in Figure 5.10; therefore, the differences in height can be attributed to differences in the conformations of the polymer chains. The most probable explanation for this is that for the smallest nanostructures, the free volume for the surface grafted polymers is high; however, as the particle size increases, the free volume is reduced because the changing geometry of the nanostructures reduces the free volume of the surface grafted polymers. This causes a progressive increase in swelling as the particle size increases, and results in an increase in height.

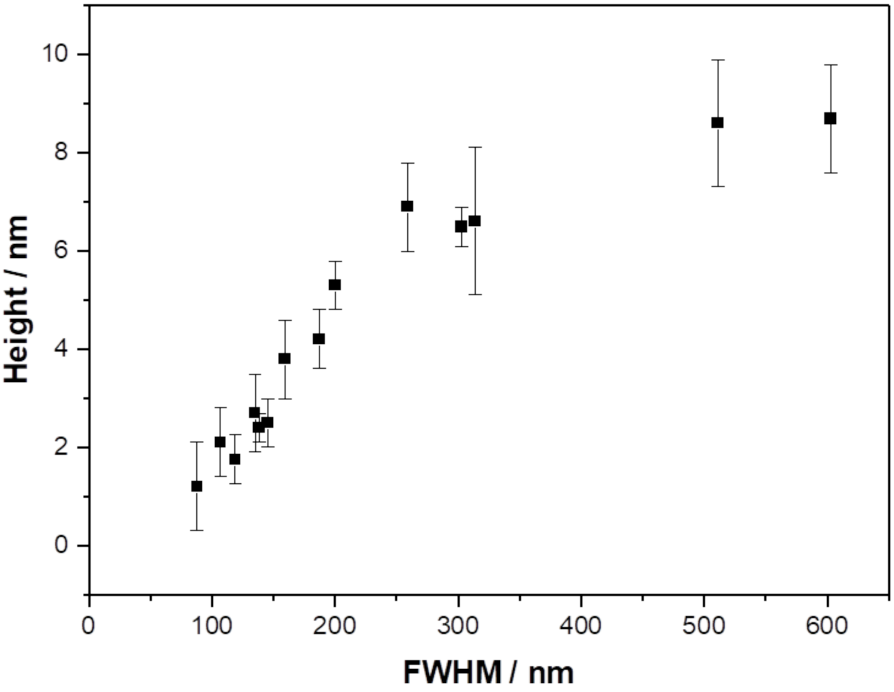

Figure 5.10 Heights of PCysMA brush films grown from gold nanostructures of varying sizes. The samples were measured at various locations on different days and the average was taken.

5.2.7 Temperature-responsiveness of PCysMA brushes in nanostructure arrays

In thermo-responsive polymers, a stretch-to-collapse transition occurs at a transition temperature because of a change in the solvation state. Polymers that are soluble upon heating have an upper critical solution temperature (UCST) which is defined as the critical temperature above which the components of a mixture are miscible in all proportions. A typical UCST system is a zwitterionic polymer, in which electrostatic interactions that stabilize the collapsed state at temperatures below the transition temperature become unsuitable above that temperature. Polymers with dispersive interactions with a solvent can also exhibit a UCST behavior. A more extensive explanation of the nature of these contributions in the context of UCST polymers may be found elsewhere;[334] however, it is widely accepted that a UCST results from strong polymer-polymer and solvent-solvent interactions rather than weak polymer-solvent interactions. The hydrophobic (entropic) impact is less dominant; consequently, UCST behavior is referred to as enthalpy driven.[334,335]

To determine whether PCysMA brushes exhibit temperature-dependent conformational changes, the ellipsometric thickness was measured as a function of temperature (in the range 8 – 40 ºC). Figure 5.11 shows the thickness of a PCysMA brush sample in water as a function of temperature. For reference, the thickness of the dry sample (in which the polymer chains are in a collapsed state) was 32 nm. The maximum thickness was measured at 8ºC. When the temperature of the water was increased, a gradual decline in the polymer film thickness was measured, and the thickness was reduced by 20 nm at 40°C. This is attributed to a reduction in the degree of solvation of the polymer as the temperature increases, leading to a reduction in steric repulsion between solvated chains and a subsequent reduction in the amount of swelling. Three measurements were recorded for each brush sample on different days and reported as the mean ± standard error.

In the range of temperature covered in Figure 5.11, the refractive index changes very slightly, (from 1.344 to 1.341).[336] Because of the sensitivity of spectroscopic ellipsometry to the optical properties of the sample, it cannot be ruled out that some of the changes displayed in Figure 1.11 are attributable to temperature-dependent changes in the refractive index. However, the magnitude of the change (from a thickness of 117 nm at 8ºC to a thickness of 105 nm at 40ºC) is too significant to be attributed solely to changes in the refractive index.

However, while there appear to be evidence regarding a temperature-dependent conformational change in PCysMA, the behaviour in Figure 5.11 does not exhibit the sharp transition that would be associated with a UCST. While there is evidence for temperature-dependent change in swelling, there is no evidence to support the stimulus-responsive behaviour that accompanies the observation of a UCST; therefore, future research should explore the use of a larger range of temperatures.

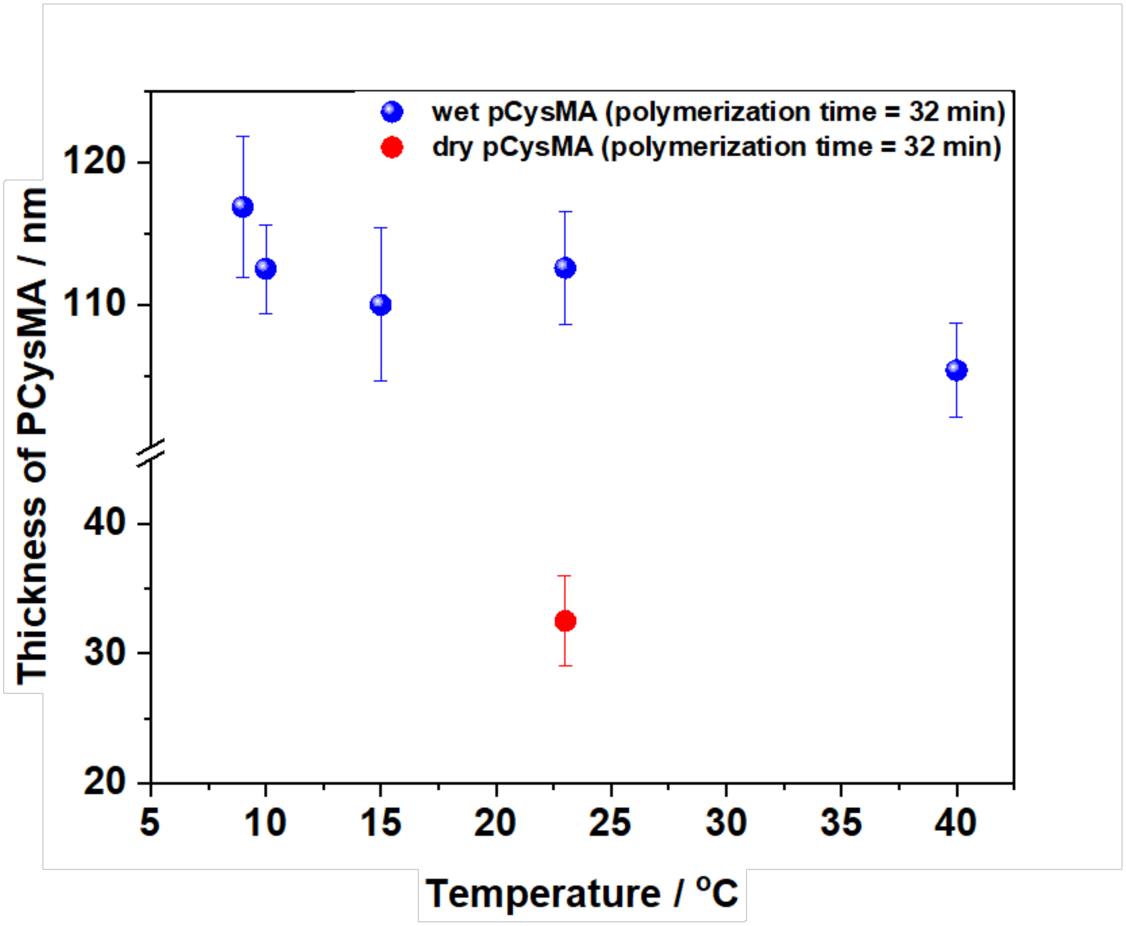

Figure 5.11 The change in the ellipsometric thickness of PCysMA brushes in water as a function of temperature. (For reference, the thickness of a dry brush is also shown).

5.2.8 Conclusions

This research investigated the growth of stimulus-responsive polymers from gold nanostructure arrays. In an aqueous solution, a cysteine methacrylate (CysMA) monomer was prepared at 97% yield by employing a selective thia-Michael addition reaction. This monomer was utilised to prepare PCysMA brushes using ATRP. The mean dry brush thicknesses were between 4 and 27 nm after polymerisation times of between 1 and 64 min. In H_2O, pH 1.57 (HCl), pH12.89 (NaOH) and 1:3 DMF:H_2O mixtures produced thicknesses of between 9 nm and 118 nm. Spectroscopic ellipsometry revealed that PCysMA brushes demonstrate pH-responsive behaviour between pH 1.6 and 12.9. The swelling state of the surface-grafted polymer layer was strongly dependent upon the composition of the medium. In water and DMF:water mixtures, the ellipsometric thickness was found to be ~1.5 times that of the dry brush, while in pH 1.57 and 12.89, the thickness was more than twice that of the dry brush. Extinction spectra of brush-functionalised gold nanoparticle arrays displayed red shifts in the position of the plasmon band that increased as a function of polymerisation time in both air and liquid. Additionally, the increases in the size of the red shift correlated with the increase in the ellipsometric thickness. This change is attributed to the increase in the mean refractive index within the plasmon mode as the polymer layer thickness increases. However, there was no statistically significant difference between the size of the red shift measured in different liquid media, because of the similarities in the refractive indices of the surface-grafted polymer and the liquid medium. AFM was used to measure the growth of PCysMA from gold nanostructure arrays and the nanostructure size of the FWHM particle. In small particles the free volume of the polymers is large, and the polymer height is small; however, as the particle size increases, the curvature decreases and results in a reduction in the free volume which is accompanied by an increase in the swelling of the surface-grafted polymer.

6. Conclusions and Future Work

6.1 Conclusions

In this research, a Lloyds' mirror interferometer was used to conduct interferometric lithography. Exposure to a dose of 34 J cm^{-2} enabled the photo-oxidation of self-assembled monolayers of octadecanethiol. By conducting exposure with an interferometer, it was possible to fabricate nanometer-scale patterns. Exposed samples were etched using a cysteamine solution to create gold nanostructures. The shape and size of these gold nanostructures were managed by altering the angle 2θ between the two beams that interfere with the surfaces of the samples. Line structures (wires) were produced using a single exposure, while double-exposure processes, in which the sample was rotated between exposures, were used to create gold nanodots and other structures. Absorption spectroscopy was employed to determine the gold nanostructures' localised surface plasmon resonance as a function of the sample morphology. It was found that nanodot arrays provide the optimum λ_{LSPR}. Gold nanostructures can function as label-free LSPR biosensors. In protein adsorption, LSPR sensors outperform traditional plasmonic devices due to their enhanced sensitivity and quicker response time. The plasmon wavelength shifts during streptavidin monolayer adsorption were comparable to, or smaller than, those reported for other sensors. This was demonstrated by measuring the extinction spectra of streptavidin and IgG immobilised on gold surfaces. Spectroscopic ellipsometry was employed to measure the fractional coverage of the protein at the gold surface as a function of the protein concentration in the solution. At monolayer coverage, the streptavidin thickness was found to be 5 nm. The formation of a protein monolayer on gold nanostructure surfaces produced a red-shift in the position of the LSPR of 17 nm and 15 nm, respectively. For biotin, streptavidin has four binding sites. Additionally, a range of biotinylated molecules are accessible, such as biotinylated DNA; therefore, other biomolecules can be strategically introduced when a surface is coated with streptavidin. This research revealed that samples of gold nanostructure can be reused many times for the immobilization of proteins by exposing them to UV to cause photocatalytic removal of the biomolecule coating; therefore, it was possible to re-use them on multiple occasions to conduct UV-vis spectroscopic analysis.

Stimulus-responsive PCysMA was grown from gold nanostructure arrays. Cysteine methacrylate (CysMA) monomer was prepared using a selective thia-Michael addition reaction. This monomer was utilised to prepare PCysMA brushes via ATRP, by incubating samples in an aqueous solution of the monomer and the ATRP catalyst. The dry brush thickness ranged from 4 to 27 nm after polymerization for 1 to 64 min. In different environments (H_2O, pH 1.57, pH 12.89, and DMF:H_2O mixtures), the thickness varied between 9 and 118 nm. The brushes exhibited pH-responsive behavior between pH 1.6 and 12.9, with swelling dependent on the medium composition. Ellipsometry revealed that in water and DMF:water mixtures, the thickness was approximately 1.5 times that of the dry brush, while at pH extremes, it was more than double the dry brush thickness. In basic (pH 12.89) and acidic (pH 1.57) conditions the mean brush thickness increases substantially because the chains acquire, respectively, net negative and positive charges. The charges on the surface-grafted polymers repel each other, causing enhanced swelling, as confirmed by spectroscopic ellipsometry. UV-vis spectra of polymer brushes under conditions of varying pH displayed varying red shifts in the plasmon band that could be correlated with changes in the swelling of the polymer: as the polymer becomes increasingly swollen, the local refractive index near the gold surface increases, leading to a red shift in the position of the plasmon band. AFM was used to measure the growth of PCysMA from gold nanostructure arrays and determine the nanostructure size of the FWHM particle. The results showed that the increased free volume impacts brush morphology by boosting the brush thickness. Additionally, PCysMA was responsive to temperature: at lower temperatures (5 ^{o}C) it increased by 20 nm and at higher temperatures (40 ^{o}C) it increased by 20 nm.

6.2 Future Research

This research focussed on the development of fabrication methods for the creation of arrays of gold nanostructures for use in biosensor applications and nanoscience. Therefore, it was essential to fully comprehend the process for creating extended gold nanoarrays via interference lithography and their optical characteristics. Additionally, a strong understanding of their use as refractive index sensors, biosensors for identifying molecules, and pH-responsive sensor applications is critical. This research was highly attentive to the crucial details, no matter how seemingly insignificant they may have appeared. Moreover, operating with diverse chemical moieties with a recognised robust binding interaction with protein allows the specific identification of that protein via a shift of LSPR. Likewise, the structures can potentially be utilised as antennae for creating nanoarrays with substantial plasmonic energy (circa 760-820nm) and to prepare the surface with molecules for applications concerning single-molecule spectroscopy. For example, the gold nanostructures could be used to drive excitation into pigment molecules in light-harvesting complexes. Light-harvesting complex 2 (LH2) from purple bacterial possesses essential absorption bands at 800 nm (the B800 band) and 850 nm (the B850 band) and there have been previous attempts to use gold nanostructures to enhance fluorescence in single-molecule studies of LH2 by achieving resonant coupling to the B800 and B850 bands.[337] Using IL, it is possible to quickly pattern very large areas, unlike the work of Wientjes et al who were only able to pattern a small area using electron beam lithography. These nanostructures display enormous potential for investigating and improving the coupling of light-absorbing proteins and their energy.

There has been significant interest regarding the use of plasmonic materials, particular the use of LSPRs for label-free medical diagnostics. However, one obstruction to the widespread use of LSPR-based diagnostic is the absence of rapid, inexpensive, programmable methods for nanostructure fabrication which facilitate control of the plasmon energy, to match requirements for specific applications, and nanofabrication over macroscopic areas which will eliminate the requirement for expensive apparatus to interrogate arrays.

7. References

1. Zia R, Schuller JA, Chandran A, Brongersma ML. Plasmonics: the next chip-scale technology. *Mater today*. 2006;9(7-8):20-27.
2. Ritchie RH, Marusak AL. The surface plasmon dispersion relation for an electron gas. *Surf Sci*. 1966;4(3):234-240.
3. Eizner E, Ellenbogen T. Local excitation of strongly coupled exciton-surface plasmons polaritons by a single nanoantenna. *Appl Phys Lett*. 2014;104(22).
4. Jiang N, Zhuo X, Wang J. Active plasmonics: principles, structures, and applications. *Chem Rev*. 2017;118(6):3054-3099.
5. Kravets VG, Kabashin A V, Barnes WL, Grigorenko AN. Plasmonic surface lattice resonances: a review of properties and applications. *Chem Rev*. 2018;118(12):5912-5951.
6. Schuller JA, Barnard ES, Cai W, Jun YC, White JS, Brongersma ML. Plasmonics for extreme light concentration and manipulation. *Nat Mater*. 2010;9(3):193-204.
7. Wuttig M, Bhaskaran H, Taubner T. Phase-change materials for non-volatile photonic applications. *Nat Photonics*. 2017;11(8):465-476.
8. Lee KS, El-Sayed MA. Gold and silver nanoparticles in sensing and imaging: sensitivity of plasmon response to size, shape, and metal composition. *J Phys Chem B*. 2006;110(39):19220-19225.
9. Jensen TR, Duval ML, Kelly KL, Lazarides AA, Schatz GC, Van Duyne RP. Nanosphere lithography: effect of the external dielectric medium on the surface plasmon resonance spectrum of a periodic array of silver nanoparticles. *J Phys Chem B*. 1999;103(45):9846-9853.
10. Urban AS, Shen X, Wang Y, et al. Three-dimensional plasmonic nanoclusters. *Nano Lett*. 2013;13(9):4399-4403.
11. Wang L, Hasanzadeh Kafshgari M, Meunier M. Optical properties and applications of plasmonic-metal nanoparticles. *Adv Funct Mater*. 2020;30(51):2005400.
12. Kang SM. Fabrication, Design, and Analytical Applications of Nanostructured Plasmonic Crystals. Published online 2014.
13. Zourob M, Elwary S, Turner APF. *Principles of Bacterial Detection: Biosensors,*

Recognition Receptors and Microsystems. Springer Science & Business Media; 2008.

14. Cunningham B, Li P, Lin B, Pepper J. Colorimetric resonant reflection as a direct biochemical assay technique. *Sensors Actuators B Chem*. 2002;81(2-3):316-328.
15. Weinstein-Webb JA. *Theranostic Multibranched Gold Nanoantennas for Cancer Diagnostics via Surface Enhanced Raman Spectroscopy and Photothermal Therapeutics*. Vanderbilt University; 2017.
16. Zheng C, Wang K, Zheng W, et al. Rapid developments in lateral flow immunoassay for nucleic acid detection. *Analyst*. 2021;146(5):1514-1528.
17. Park J. Lateral flow immunoassay reader technologies for quantitative point-of-care testing. *Sensors*. 2022;22(19):7398.
18. Sajid M, Kawde AN, Daud M. Designs, formats and applications of lateral flow assay: A literature review. *J Saudi Chem Soc*. 2015;19(6):689-705.
19. Sarkar TK, Abdallah MN, Salazar-Palma M, Dyab WM. Surface Plasmons-Polaritons, Surface Waves, and Zenneck Waves: Clarification of the terms and a description of the concepts and their evolution. *IEEE Antennas Propag Mag*. 2017;59(3):77-93.
20. Shahbazyan T V, Stockman MI. *Plasmonics: Theory and Applications*. Vol 15. Springer; 2013.
21. Xia Y, Halas NJ. Shape-controlled synthesis and surface plasmonic properties of metallic nanostructures. *MRS Bull*. 2005;30(5):338-348.
22. Garifullina A, Shen AQ. Optimized immobilization of biomolecules on nonspherical gold nanostructures for efficient localized surface plasmon resonance biosensing. *Anal Chem*. 2019;91(23):15090-15098.
23. Ferry VE, Munday JN, Atwater HA. Design considerations for plasmonic photovoltaics. *Adv Mater*. 2010;22(43):4794-4808.
24. Hägglund C, Apell SP. Plasmonic near-field absorbers for ultrathin solar cells. *J Phys Chem Lett*. 2012;3(10):1275-1285.
25. Sotiriou GA. Biomedical applications of multifunctional plasmonic nanoparticles. *Wiley Interdiscip Rev Nanomedicine Nanobiotechnology*. 2013;5(1):19-30.
26. Tan P, Li H, Wang J, Gopinath SCB. Silver nanoparticle in biosensor and bioimaging: Clinical perspectives. *Biotechnol Appl Biochem*. 2021;68(6):1236-1242.
27. Celasco E, Chaika AN, Stauber T, et al. Handbook of graphene. Published online 2019.

28. Doria G, Conde J, Veigas B, et al. Noble metal nanoparticles for biosensing applications. *Sensors*. 2012;12(2):1657-1687.

29. Yu AYH, Fu RH, Hsu S hui, et al. Epidermal growth factor receptors siRNA-conjugated collagen modified gold nanoparticles for targeted imaging and therapy of lung cancer. *Mater Today Adv*. 2021;12:100191.

30. Sokolov K, Follen M, Aaron J, et al. Real-time vital optical imaging of precancer using anti-epidermal growth factor receptor antibodies conjugated to gold nanoparticles. *Cancer Res*. 2003;63(9):1999-2004.

31. Santra S, Dutta D, Walter GA, Moudgil BM. Fluorescent nanoparticle probes for cancer imaging. *Technol Cancer Res Treat*. 2005;4(6):593-602.

32. Huang X, Mahmudul HM, Li Z, et al. Noble metal nanomaterials for the diagnosis and treatment of hematological malignancies. *Front Biosci*. 2022;27(2):40.

33. Nguyen TM, Cho Y, Huh JH, et al. Ultralow-Loss Substrate for Nanophotonic Dark-Field Microscopy. *Nano Lett*. 2023;23(4):1546-1554.

34. Oliveira RD, Mouquinho A, Centeno P, et al. Colloidal lithography for photovoltaics: An attractive route for light management. *Nanomaterials*. 2021;11(7):1665.

35. Maier SA. *Plasmonics: Fundamentals and Applications*. Vol 1. Springer; 2007.

36. Enoch S, Bonod N. *Plasmonics: From Basics to Advanced Topics*. Vol 167. Springer; 2012.

37. Raether H. Surface Plasmons on Smooth and Rough Surfaces and on Gratings, Vol. 111 of Springer Tracks in Modern Physics Springer. *New York*. Published online 1988.

38. Tong J, Suo F, Ma J, Tobing LYM, Qian L, Zhang DH. Surface plasmon enhanced infrared photodetection. *Opto-Electronic Adv*. 2019;2(1):180021-180026.

39. Jestädt R, Ruggenthaler M, Oliveira MJT, Rubio A, Appel H. Light-matter interactions within the Ehrenfest–Maxwell–Pauli–Kohn–Sham framework: fundamentals, implementation, and nano-optical applications. *Adv Phys*. 2019;68(4):225-333.

40. Wolski A. Theory of electromagnetic fields. *arXiv Prepr arXiv11114354*. Published online 2011.

41. Silaeva E, Saddier L, Colombier JP. Drude-Lorentz Model for Optical Properties of Photoexcited Transition Metals under Electron-Phonon Nonequilibrium. *Appl Sci*. 2021;11(21):9902.

42. Zhang J, Zhang L, Xu W. Surface plasmon polaritons: physics and applications. *J Phys D Appl Phys*. 2012;45(11):113001.

43. Raether H. Surface plasmons on smooth surfaces. *Surf plasmons smooth rough surfaces gratings*. Published online 2006:4-39.

44. Grote R. Design and application of plasmonic devices. Published online 2008.

45. Doevenspeck J. Plasmonics: Circuit and system-level evaluation for beyond-CMOS applications. Published online 2016.

46. Wood RW. XLII. On a remarkable case of uneven distribution of light in a diffraction grating spectrum. *London, Edinburgh, Dublin Philos Mag J Sci*. 1902;4(21):396-402.

47. Jia P. *Plasmonic Optical Sensors: Performance Analysis and Engineering Towards Biosensing*. The University of Western Ontario (Canada); 2014.

48. Schasfoort RBM, Lokate AM, Beusink JB, Pruijn GJ, Engbers GH. Measurement of the analysis cycle: Scanning spr microarray imaging of autoimmune diseases. *Handb Surf Plasmon Reson pags*. Published online 2008:221-245.

49. Khansili N, Rattu G, Krishna PM. Label-free optical biosensors for food and biological sensor applications. *Sensors Actuators B Chem*. 2018;265:35-49.

50. Sabban S, Ye H, Helm B. Development of an in vitro model system for studying the interaction of Equus caballus IgE with its high-affinity receptor FceRI. *Vet Immunol Immunopathol*. 2013;153(1-2):10-16. doi:10.1016/j.vetimm.2013.01.008

51. Hao D. Hybridisation of plasmonic and acoustic biosensing devices. Published online 2018.

52. Greene JE. Tracing the 5000-year recorded history of inorganic thin films from~ 3000 BC to the early 1900s AD. *Appl Phys Rev*. 2014;1(4):41302.

53. Kelly KL, Coronado E, Zhao LL, Schatz GC. The optical properties of metal nanoparticles: the influence of size, shape, and dielectric environment. *J Phys Chem B*. 2003;107(3):668-677.

54. Sherry LJ, Chang SH, Schatz GC, Van Duyne RP, Wiley BJ, Xia Y. Localized surface plasmon resonance spectroscopy of single silver nanocubes. *Nano Lett*. 2005;5(10):2034-2038.

55. Wriedt T. A review of elastic light scattering theories. *Part Part Syst Charact Meas Descr Part Prop Behav Powders Other Disperse Syst*. 1998;15(2):67-74.

56. Mishchenko MI, Travis LD. Gustav Mie and the evolving discipline of electromagnetic scattering by particles. *Bull Am Meteorol Soc*. 2008;89(12):1853-1862.
57. Mie G. Beiträge zur Optik trüber Medien, speziell kolloidaler Metallösungen. *Ann Phys*. 1908;330(3):377-445.
58. Horvath H. Gustav Mie and the scattering and absorption of light by particles: Historic developments and basics. *J Quant Spectrosc Radiat Transf*. 2009;110(11):787-799.
59. Kreibig U, Zacharias P. Surface plasma resonances in small spherical silver and gold particles. *Zeitschrift für Phys A Hadron Nucl*. 1970;231:128-143.
60. Morpurgo A, Pedersini F, Reina A. A low-cost instrument for environmental particulate analysis based on optical scattering. *2012 IEEE I2MTC - Int Instrum Meas Technol Conf Proc*. Published online 2012:2646-2650. doi:10.1109/I2MTC.2012.6229220
61. Lachaine R, Boulais E, Rioux D, Boutopoulos C, Meunier M. Computational design of durable spherical nanoparticles with optimal material, shape, and size for ultrafast plasmon-enhanced nanocavitation. *ACS Photonics*. 2016;3(11):2158-2169.
62. Heath S. Methods, products, and systems relating to making, providing, and using nanocrystalline cellulose superlattice solar cells to produce electricity. Published online August 8, 2019.
63. Auner GW, Koya SK, Huang C, et al. Applications of Raman spectroscopy in cancer diagnosis. *Cancer Metastasis Rev*. 2018;37:691-717.
64. Mantri Y, Jokerst J V. Engineering plasmonic nanoparticles for enhanced photoacoustic imaging. *ACS Nano*. 2020;14(8):9408-9422.
65. de Aberasturi DJ, Serrano-Montes AB, Liz-Marzán LM. Modern applications of plasmonic nanoparticles: from energy to health. *Adv Opt Mater*. 2015;3(5):602-617.
66. Li Z. Mesoscopic and microscopic strategies for engineering plasmon-enhanced raman scattering. *Adv Opt Mater*. 2018;6(16):1701097.
67. Do PQT, Huong VT, Phuong NTT, et al. The highly sensitive determination of serotonin by using gold nanoparticles (Au NPs) with a localized surface plasmon resonance (LSPR) absorption wavelength in the visible region. *RSC Adv*. 2020;10(51):30858-30869.
68. Szunerits S, Spadavecchia J, Boukherroub R. Surface plasmon resonance: Signal amplification using colloidal gold nanoparticles for enhanced sensitivity. *Rev Anal Chem*. 2014;33(3):153-164.

69. Lyon LA, Peña DJ, Natan MJ. Surface plasmon resonance of Au colloid-modified Au films: particle size dependence. *J Phys Chem B*. 1999;103(28):5826-5831.

70. Hutter E, Cha S, Liu JF, et al. Role of substrate metal in gold nanoparticle enhanced surface plasmon resonance imaging. *J Phys Chem B*. 2001;105(1):8-12.

71. Zhou ZK, Peng XN, Yang ZJ, et al. Tuning gold nanorod-nanoparticle hybrids into plasmonic Fano resonance for dramatically enhanced light emission and transmission. *Nano Lett*. 2011;11(1):49-55.

72. Peng G, Hakim M, Broza YY, et al. Detection of lung, breast, colorectal, and prostate cancers from exhaled breath using a single array of nanosensors. *Br J Cancer*. 2010;103(4):542-551.

73. Barizuddin S, Bok S, Gangopadhyay S. Plasmonic sensors for disease detection-a review. *J Nanomed Nanotechnol*. 2016;7(3):1000373.

74. Valev VK, Baumberg JJ, Sibilia C, Verbiest T. Chirality and chiroptical effects in plasmonic nanostructures: fundamentals, recent progress, and outlook. *Adv Mater*. 2013;25(18):2517-2534.

75. Agarwal D, Aspetti CO, Cargnello M, et al. Engineering localized surface plasmon interactions in gold by silicon nanowire for enhanced heating and photocatalysis. *Nano Lett*. 2017;17(3):1839-1845.

76. Chen J, Cong H, Loo FC, et al. Thermal gradient induced tweezers for the manipulation of particles and cells. *Sci Rep*. 2016;6(1):35814.

77. Stilgoe AB, Nieminen TA, Knöner G, Heckenberg NR, Rubinsztein-Dunlop H. The effect of Mie resonances on trapping in optical tweezers. *Opt Express*. 2008;16(19):15039-15051.

78. Bustamante CJ, Chemla YR, Liu S, Wang MD. Optical tweezers in single-molecule biophysics. *Nat Rev Methods Prim*. 2021;1(1):25.

79. Dhakal KR, Lakshminarayanan V. Optical tweezers: fundamentals and some biophysical applications. In: *Progress in Optics*. Vol 63. Elsevier; 2018:1-31.

80. Jackson JB, Halas NJ. Surface-enhanced Raman scattering on tunable plasmonic nanoparticle substrates. *Proc Natl Acad Sci*. 2004;101(52):17930-17935.

81. Kubik T, Bogunia-Kubik K, Sugisaka M. Nanotechnology on duty in medical applications. *Curr Pharm Biotechnol*. 2005;6(1):17-33.

82. Ozbay E. Plasmonics: merging photonics and electronics at nanoscale dimensions. *Science (80-)*. 2006;311(5758):189-193.

83. Adato R, Yanik AA, Altug H. On chip plasmonic monopole nano-antennas and circuits. *Nano Lett*. 2011;11(12):5219-5226.

84. Yue Z, Cai B, Wang L, Wang X, Gu M. Intrinsically core-shell plasmonic dielectric nanostructures with ultrahigh refractive index. *Sci Adv*. 2016;2(3):e1501536.

85. Yu P, Yao Y, Wu J, Niu X, Rogach AL, Wang Z. Effects of plasmonic metal core-dielectric shell nanoparticles on the broadband light absorption enhancement in thin film solar cells. *Sci Rep*. 2017;7(1):7696.

86. Fleischmann M, Hendra PJ, McQuillan AJ. Raman spectra of pyridine adsorbed at a silver electrode. *Chem Phys Lett*. 1974;26(2):163-166.

87. Campion A, Kambhampati P. Surface-enhanced Raman scattering. *Chem Soc Rev*. 1998;27(4):241-250.

88. Yeh DM, Huang CF, Chen CY, Lu YC, Yang CC. Localized surface plasmon-induced emission enhancement of a green light-emitting diode. *Nanotechnology*. 2008;19(34):345201.

89. Govorov AO, Bryant GW, Zhang W, et al. Exciton− plasmon interaction and hybrid excitons in semiconductor− metal nanoparticle assemblies. *Nano Lett*. 2006;6(5):984-994.

90. Drexhage KH. IV interaction of light with monomolecular dye layers. In: *Progress in Optics*. Vol 12. Elsevier; 1974:163-232.

91. Berman PR. Analysis of dynamical suppression of spontaneous emission. *Phys Rev A*. 1998;58(6):4886.

92. Yang KY, Choi KC, Ahn CW. Surface plasmon-enhanced spontaneous emission rate in an organic light-emitting device structure: Cathode structure for plasmonic application. *Appl Phys Lett*. 2009;94(17):121.

93. Liu X, Galfsky T, Sun Z, et al. Strong light–matter coupling in two-dimensional atomic crystals. *Nat Photonics*. 2015;9(1):30-34.

94. Liu W, Lee B, Naylor CH, et al. Strong exciton–plasmon coupling in MoS2 coupled with plasmonic lattice. *Nano Lett*. 2016;16(2):1262-1269.

95. Porras D, Ciuti C, Baumberg JJ, Tejedor C. Polariton dynamics and Bose-Einstein condensation in semiconductor microcavities. *Phys Rev B*. 2002;66(8):85304.

96. Hennessy K, Badolato A, Winger M, et al. Quantum nature of a strongly coupled single quantum dot–cavity system. *Nature*. 2007;445(7130):896-899.

97. Wei H, Ratchford D, Li X, Xu H, Shih CK. Propagating surface plasmon induced photon emission from quantum dots. *Nano Lett*. 2009;9(12):4168-4171.

98. Xia K, Twamley J. All-optical switching and router via the direct quantum control of coupling between cavity modes. *Phys Rev X*. 2013;3(3):31013.

99. McKeever J, Boca A, Boozer AD, Buck JR, Kimble HJ. Experimental realization of a one-atom laser in the regime of strong coupling. *Nature*. 2003;425(6955):268-271.

100. Chang DE, Sørensen AS, Demler EA, Lukin MD. A single-photon transistor using nanoscale surface plasmons. *Nat Phys*. 2007;3(11):807-812.

101. Bennett DIG, Amarnath K, Fleming GR. A structure-based model of energy transfer reveals the principles of light harvesting in photosystem II supercomplexes. *J Am Chem Soc*. 2013;135(24):9164-9173.

102. Andreussi O, Biancardi A, Corni S, Mennucci B. Plasmon-controlled light-harvesting: Design rules for biohybrid devices via multiscale modeling. *Nano Lett*. 2013;13(9):4475-4484.

103. Yao K, Jiao H, Xu YX, He Q, Li F, Wang X. Nano-bio hybrids of plasmonic metals/photosynthetic proteins for broad-band light absorption enhancement in organic solar cells. *J Mater Chem A*. 2016;4(35):13400-13406.

104. Lishchuk A, Vasilev C, Johnson MP, Hunter CN, Törmä P, Leggett GJ. Turning the challenge of quantum biology on its head: biological control of quantum optical systems. *Faraday Discuss*. 2019;216:57-71.

105. Wijaya E, Lenaerts C, Maricot S, et al. Surface plasmon resonance-based biosensors: From the development of different SPR structures to novel surface functionalization strategies. *Curr Opin Solid State Mater Sci*. 2011;15(5):208-224.

106. Homola J. Electromagnetic theory of surface plasmons. *Surf plasmon Reson based sensors*. Published online 2006:3-44.

107. Escobedo C, Brolo AG, Gordon R, Sinton D. Optofluidic concentration: plasmonic nanostructure as concentrator and sensor. *Nano Lett*. 2012;12(3):1592-1596.

108. Jageler-Hoheisel T, Cordeiro J, Lecarme O, et al. Plasmonic shaping in gold nanoparticle three-dimensional assemblies. *J Phys Chem C*. 2013;117(44):23126-23132.

109. Aziz MA, Patra S, Yang H. A facile method of achieving low surface coverage of Au nanoparticles on an indium tin oxide electrode and its application to protein detection. *Chem Commun*. 2008;(38):4607-4609.

110. Valsecchi C, Brolo AG. Periodic metallic nanostructures as plasmonic chemical sensors. *Langmuir*. 2013;29(19):5638-5649.

111. Tsargorodska A, El Zubir O, Darroch B, et al. Fast, simple, combinatorial routes to the fabrication of reusable, plasmonically active gold nanostructures by interferometric lithography of self-assembled monolayers. *ACS Nano*. 2014;8(8):7858-7869.

112. Nylander C, Liedberg B, Lind T. Gas detection by means of surface plasmon resonance. *Sensors and Actuators*. 1982;3:79-88.

113. Anker JN, Hall WP, Lyandres O, Shah NC, Zhao J, Van Duyne RP. Biosensing with plasmonic nanosensors. *Nat Mater*. 2008;7(6):442-453.

114. Yu Y, Zappe H. Effect of lens size on the focusing performance of plasmonic lenses and suggestions for the design. *Opt Express*. 2011;19(10):9434-9444.

115. Temple TL, Mahanama GDK, Reehal HS, Bagnall DM. Influence of localized surface plasmon excitation in silver nanoparticles on the performance of silicon solar cells. *Sol Energy Mater Sol Cells*. 2009;93(11):1978-1985.

116. Wang C, Gao P, Zhao Z, et al. Deep sub-wavelength imaging lithography by a reflective plasmonic slab. *Opt Express*. 2013;21(18):20683-20691.

117. McClements J, Bar L, Singla P, et al. Molecularly imprinted polymer nanoparticles enable rapid, reliable, and robust point-of-care thermal detection of SARS-CoV-2. *ACS sensors*. 2022;7(4):1122-1131.

118. McMahon RJ. *Avidin-Biotin Interactions: Methods and Applications*. Vol 418. Springer Science & Business Media; 2008.

119. Mayer KM, Hafner JH. Localized surface plasmon resonance sensors. *Chem Rev*. 2011;111(6):3828-3857.

120. Bhattarai JK, Maruf MHU, Stine KJ. Plasmonic-active nanostructured thin films. *Processes*. 2020;8(1):115.

121. Haes AJ, Van Duyne RP. A unified view of propagating and localized surface plasmon resonance biosensors. *Anal Bioanal Chem*. 2004;379:920-930.

122. Arai T, Kumar PKR, Rockstuhl C, Awazu K, Tominaga J. An optical biosensor based on

localized surface plasmon resonance of silver nanostructured films. *J Opt A Pure Appl Opt*. 2007;9(7):699.

123. Barbillon G, Bijeon JL, Plain J, Royer P. Sensitive detection of biological species through localized surface-plasmon resonance on gold nanodisks. *Thin Solid Films*. 2009;517(9):2997-3000.

124. Tu MH. Investigation of metal nanomaterials as a sensing element in LSPR-based optical fibre sensor development. Published online 2014.

125. Marinakos SM, Chen S, Chilkoti A. Plasmonic detection of a model analyte in serum by a gold nanorod sensor. *Anal Chem*. 2007;79(14):5278-5283.

126. Wang Y, Qian W, Tan Y, Ding S. A label-free biosensor based on gold nanoshell monolayers for monitoring biomolecular interactions in diluted whole blood. *Biosens Bioelectron*. 2008;23(7):1166-1170.

127. Banica FG. *Chemical Sensors and Biosensors: Fundamentals and Applications*. John Wiley & Sons; 2012.

128. Mayer KM, Lee S, Liao H, et al. A label-free immunoassay based upon localized surface plasmon resonance of gold nanorods. *ACS Nano*. 2008;2(4):687-692.

129. Fu J, Park B, Zhao Y. Limitation of a localized surface plasmon resonance sensor for Salmonella detection. *Sensors Actuators B Chem*. 2009;141(1):276-283.

130. Haes AJ, Chang L, Klein WL, Van Duyne RP. Detection of a biomarker for Alzheimer's disease from synthetic and clinical samples using a nanoscale optical biosensor. *J Am Chem Soc*. 2005;127(7):2264-2271.

131. Zheng S, Kim DK, Park TJ, Lee SJ, Lee SY. Label-free optical diagnosis of hepatitis B virus with genetically engineered fusion proteins. *Talanta*. 2010;82(2):803-809.

132. Park TJ, Lee SJ, Kim DK, Heo NS, Park JY, Lee SY. Development of label-free optical diagnosis for sensitive detection of influenza virus with genetically engineered fusion protein. *Talanta*. 2012;89:246-252.

133. Beeram SR, Zamborini FP. Selective attachment of antibodies to the edges of gold nanostructures for enhanced localized surface plasmon resonance biosensing. *J Am Chem Soc*. 2009;131(33):11689-11691.

134. Huang H, Tang C, Zeng Y, et al. Label-free optical biosensor based on localized surface plasmon resonance of immobilized gold nanorods. *Colloids surfaces B Biointerfaces*.

2009;71(1):96-101.

135. Torun Ö, Boyacı İH, Temür E, Tamer U. Comparison of sensing strategies in SPR biosensor for rapid and sensitive enumeration of bacteria. *Biosens Bioelectron*. 2012;37(1):53-60.

136. Nuopponen M, Tenhu H. Gold nanoparticles protected with pH and temperature-sensitive diblock copolymers. *Langmuir*. 2007;23(10):5352-5357.

137. Mack NH, Wackerly JW, Malyarchuk V, Rogers JA, Moore JS, Nuzzo RG. Optical transduction of chemical forces. *Nano Lett*. 2007;7(3):733-737.

138. Jiang H, Markowski J, Sabarinathan J. Near-infrared optical response of thin film pH-sensitive hydrogel coated on a gold nanocrescent array. *Opt Express*. 2009;17(24):21802-21807.

139. Giannini V, Fernández-Domínguez AI, Heck SC, Maier SA. Plasmonic nanoantennas: fundamentals and their use in controlling the radiative properties of nanoemitters. *Chem Rev*. 2011;111(6):3888-3912.

140. Lakowicz JR. Radiative decay engineering 3. Surface plasmon-coupled directional emission. *Anal Biochem*. 2004;324(2):153-169.

141. Hrelescu C, Sau TK, Rogach AL, Jäckel F, Feldmann J. Single gold nanostars enhance Raman scattering. *Appl Phys Lett*. 2009;94(15):153113.

142. Atwater HA, Polman A. Plasmonics for improved photovoltaic devices. *Nat Mater*. 2010;9(3):205-213.

143. Jain PK, Huang X, El-Sayed IH, El-Sayed MA. Review of some interesting surface plasmon resonance-enhanced properties of noble metal nanoparticles and their applications to biosystems. *Plasmonics*. 2007;2:107-118.

144. Bardhan R, Chen W, Perez-Torres C, et al. Nanoshells with targeted simultaneous enhancement of magnetic and optical imaging and photothermal therapeutic response. *Adv Funct Mater*. 2009;19(24):3901-3909.

145. Zhang JZ, Noguez C. Plasmonic optical properties and applications of metal nanostructures. *Plasmonics*. 2008;3:127-150.

146. Li JF, Huang YF, Ding Y, et al. Shell-isolated nanoparticle-enhanced Raman spectroscopy. *Nature*. 2010;464(7287):392-395.

147. Cuesta IF, West MM, Montinaro E, Schwartzberg A, Cabrini S. A nanochannel through a

plasmonic antenna gap: an integrated device for single particle counting. *Lab Chip*. 2019;19(14):2394-2403.

148. Homola J. Present and future of surface plasmon resonance biosensors. *Anal Bioanal Chem*. 2003;377:528-539.

149. Draine BT, Flatau PJ. Discrete-dipole approximation for scattering calculations. *Josa a*. 1994;11(4):1491-1499.

150. Willets KA, Van Duyne RP. Localized surface plasmon resonance spectroscopy and sensing. *Annu Rev Phys Chem*. 2007;58:267-297.

151. Dutta J, Hofmann H. Self-organization of colloidal nanoparticles. In: *Encyclopedia of Nanoscience and Nanotechnology*. Vol 9. American Scientific Publishers California; 2004:617-640.

152. Lotito V, Zambelli T. Playing with sizes and shapes of colloidal particles via dry etching methods. *Adv Colloid Interface Sci*. 2022;299:102538.

153. Katsikis N, Zahradnik F, Helmschrott A, Münstedt H, Vital A. Thermal stability of poly (methyl methacrylate)/silica nano-and microcomposites as investigated by dynamic-mechanical experiments. *Polym Degrad Stab*. 2007;92(11):1966-1976.

154. Peng B. Control over Colloidal Particle Morphology by Dispersion Polymerization. *Ph D Thesis*. Published online 2013.

155. Wang N, Zhou H, Ren J, et al. Polymer@ SiO2 Core–Shell Composite Particles: Preparation and Application. *Coatings*. 2023;13(2):334.

156. Thangamuthu M, Santschi C, Martin OJF. Reliable Langmuir Blodgett colloidal masks for large area nanostructure realization. *Thin Solid Films*. 2020;709:138195.

157. Ingert D, Pileni M. Nano Lithography. *Nanocrystals Form Mesoscopic Struct*. Published online 2005:295-305.

158. Wang H, Chen W, Chen B, et al. Interfacial Capillary-Force-Driven Self-Assembly of Monolayer Colloidal Crystals for Supersensitive Plasmonic Sensors. *Small*. 2020;16(8):1905480.

159. Ohno T, Wadell C, Inagaki S, et al. Hole-size tuning and sensing performance of hexagonal plasmonic nanohole arrays. *Opt Mater Express*. 2016;6(5):1594-1603.

160. Tseng AA, Chen K, Chen CD, Ma KJ. Electron beam lithography in nanoscale fabrication: recent development. *IEEE Trans Electron Packag Manuf*. 2003;26(2):141-

149.

161. Stepanova M, Fito T, Szabó Z, et al. Simulation of electron beam lithography of nanostructures. *J Vac Sci Technol B, Nanotechnol Microelectron Mater Process Meas Phenom*. 2010;28(6):C6C48-C6C57.

162. Mohammad MA, Dew SK, Westra K, et al. Nanoscale resist morphologies of dense gratings using electron-beam lithography. *J Vac Sci Technol B Microelectron Nanom Struct Process Meas Phenom*. 2007;25(3):745-753.

163. Abbas A. Nanofabrication using electron beam lithography: novel resist and applications. Published online 2013.

164. Sun S, Leggett GJ. Matching the resolution of electron beam lithography by scanning near-field photolithography. *Nano Lett*. 2004;4(8):1381-1384.

165. Lérondel G, Kostcheev S, Plain J. Nanofabrication for plasmonics. *Plasmon From Basics to Adv Top*. Published online 2012:269-316.

166. Florence JM, Boysel RM. Multiple phase light modulation using binary addressing. Published online February 25, 1997.

167. Aassime A, Hamouda F. Conventional and un-conventional lithography for fabricating thin film functional devices. In: *Modern Technologies for Creating the Thin-Film Systems and Coatings*. IntechOpen; 2017.

168. Brueck SRJ. Optical and interferometric lithography-nanotechnology enablers. *Proc IEEE*. 2005;93(10):1704-1721.

169. Gates BD, Xu Q, Stewart M, Ryan D, Willson CG, Whitesides GM. New approaches to nanofabrication: molding, printing, and other techniques. *Chem Rev*. 2005;105(4):1171-1196.

170. Berggren K, Menon R, Mondol MK, et al. Nanostructures Technology, Research and Applications.

171. Jhaveri T, Strojwas A, Pileggi L, Rovner V. Economic assessment of lithography strategies for the 22nm technology node. In: *Photomask Technology 2009*. Vol 7488. SPIE; 2009:873-882.

172. Juodkazis S, Mizeikis V, Misawa H. Three-dimensional microfabrication of materials by femtosecond lasers for photonics applications. *J Appl Phys*. 2009;106(5):8.

173. Sreekanth KV, Chua JK, Murukeshan VM. Interferometric lithography for nanoscale

feature patterning: a comparative analysis between laser interference, evanescent wave interference, and surface plasmon interference. *Appl Opt*. 2010;49(35):6710-6717.

174. Smith HI. Low cost nanolithography with nanoaccuracy. *Phys E Low-dimensional Syst Nanostructures*. 2001;11(2-3):104-109.
175. Dakss ML, Kuhn L, Heidrich PF, Scott BA. Grating coupler for efficient excitation of optical guided waves in thin films. *Appl Phys Lett*. 1970;16(12):523-525.
176. Gronheid R, Leeson MJ. Extreme ultraviolet interference lithography as applied to photoresist studies. *J Micro/Nanolithography, MEMS MOEMS*. 2009;8(2):21205.
177. Zaidi SH, Brueck SRJ. Multiple-exposure interferometric lithography. *J Vac Sci Technol B Microelectron Nanom Struct Process Meas Phenom*. 1993;11(3):658-666.
178. Pang L, Nakagawa W, Fainman Y. Fabrication of two-dimensional photonic crystals with controlled defects by use of multiple exposures and direct write. *Appl Opt*. 2003;42(27):5450-5456.
179. Moon JH, Ford J, Yang S. Fabricating three-dimensional polymeric photonic structures by multi-beam interference lithography. *Polym Adv Technol*. 2006;17(2):83-93.
180. Wernérus H, Samuelson P, Ståhl S. Fluorescence-activated cell sorting of specific affibody-displaying staphylococci. *Appl Environ Microbiol*. 2003;69(9):5328-5335.
181. Lai ND, Liang WP, Lin JH, Hsu CC, Lin CH. Fabrication of two-and three-dimensional periodic structures by multi-exposure of two-beam interference technique. *Opt Express*. 2005;13(23):9605-9611.
182. Xia D, Ku Z, Lee SC, Brueck SRJ. Nanostructures and functional materials fabricated by interferometric lithography. *Adv Mater*. 2011;23(2):147-179.
183. Solak HH, He D, Li W, et al. Exposure of 38 nm period grating patterns with extreme ultraviolet interferometric lithography. *Appl Phys Lett*. 1999;75(15):2328-2330.
184. Wei Y, Back D. 193nm immersion lithography: Status and challenges. *SPIE Newsroom*. Published online 2007.
185. Feldmann H, Gruner T, Epple A. Method of manufacturing a projection objective and projection objective. Published online June 7, 2016.
186. Wei Y, Brainard RL. *Advanced Processes for 193-Nm Immersion Lithography*. Vol 189. SPIE press; 2009.
187. Ritucci A, Reale A, Zuppella P, et al. Interference lithography by a soft x-ray laser beam:

Nanopatterning on photoresists. *J Appl Phys*. 2007;102(3):34313.

188. Flagello D, Doering J. Gradient immersion lithography. Published online October 11, 2005.

189. Bloomstein TM, Marchant MF, Deneault S, Hardy DE, Rothschild M. 22-nm immersion interference lithography. *Opt Express*. 2006;14(14):6434-6443.

190. de Boor J, Kim DS, Schmidt V. Sub-50 nm patterning by immersion interference lithography using a Littrow prism as a Lloyd's interferometer. *Opt Lett*. 2010;35(20):3450-3452.

191. van Rijn CJM, Nijdam W, Kuiper S, Veldhuis GJ, van Wolferen H, Elwenspoek M. Microsieves made with laser interference lithography for micro-filtration applications. *J micromechanics microengineering*. 1999;9(2):170.

192. Bozler CO, Harris CT, Rabe S, Rathman DD, Hollis MA, Smith HI. Arrays of gated field-emitter cones having 0.32 µm tip-to-tip spacing. *J Vac Sci Technol B Microelectron Nanom Struct Process Meas Phenom*. 1994;12(2):629-632.

193. Spallas JP, Hawryluk AM, Kania DR. Field emitter array mask patterning using laser interference lithography. *J Vac Sci Technol B Microelectron Nanom Struct Process Meas Phenom*. 1995;13(5):1973-1978.

194. Fernandez A, Bedrossian PJ, Baker SL, Vernon SP, Kania DR. Magnetic force microscopy of single-domain cobalt dots patterned using interference lithography. *IEEE Trans Magn*. 1996;32(5):4472-4474.

195. Adams J, Tizazu G, Janusz S, Brueck SRJ, Lopez GP, Leggett GJ. Large-area nanopatterning of self-assembled monolayers of alkanethiolates by interferometric lithography. *Langmuir*. 2010;26(16):13600-13606.

196. Tizazu G, El-Zubir O, Brueck SRJ, Lidzey DG, Leggett GJ, Lopez GP. Large area nanopatterning of alkylphosphonate self-assembled monolayers on titanium oxide surfaces by interferometric lithography. *Nanoscale*. 2011;3(6):2511-2516.

197. Lu C, Lipson RH. Interference lithography: a powerful tool for fabricating periodic structures. *Laser Photon Rev*. 2010;4(4):568-580.

198. Christensen JF, Olesen MH, Kjær JS. The industrial dynamics of Open Innovation—Evidence from the transformation of consumer electronics. *Res Policy*. 2005;34(10):1533-1549.

199. Benson O. Assembly of hybrid photonic architectures from nanophotonic constituents. *Nature*. 2011;480(7376):193-199.

200. Sinibaldi A, Danz N, Descrovi E, et al. Direct comparison of the performance of Bloch surface wave and surface plasmon polariton sensors. *Sensors Actuators B Chem*. 2012;174:292-298.

201. Sekhon JS, Verma SS. Plasmonics: the future wave of communication. *Curr Sci*. 2011;101(4):484-488.

202. Singh M, Kaur N, Comini E. The role of self-assembled monolayers in electronic devices. *J Mater Chem C*. 2020;8(12):3938-3955.

203. Ferretti S, Paynter S, Russell DA, Sapsford KE, Richardson DJ. Self-assembled monolayers: a versatile tool for the formulation of bio-surfaces. *TrAC Trends Anal Chem*. 2000;19(9):530-540.

204. Chaki NK, Aslam M, Sharma J, Vijayamohanan K. Applications of self-assembled monolayers in materials chemistry. *J Chem Sci*. 2001;113:659-670.

205. Brust M, Kiely CJ. Some recent advances in nanostructure preparation from gold and silver particles: a short topical review. *Colloids Surfaces A Physicochem Eng Asp*. 2002;202(2-3):175-186.

206. Guix M, Mayorga-Martinez CC, Merkoçi A. Nano/micromotors in (bio) chemical science applications. *Chem Rev*. 2014;114(12):6285-6322.

207. Love JC, Estroff LA, Kriebel JK, Nuzzo RG, Whitesides GM. Self-assembled monolayers of thiolates on metals as a form of nanotechnology. *Chem Rev*. 2005;105(4):1103-1170.

208. Arima Y, Iwata H. Effect of wettability and surface functional groups on protein adsorption and cell adhesion using well-defined mixed self-assembled monolayers. *Biomaterials*. 2007;28(20):3074-3082.

209. Ulman A. Formation and structure of self-assembled monolayers. *Chem Rev*. 1996;96(4):1533-1554.

210. Casalini S, Bortolotti CA, Leonardi F, Biscarini F. Self-assembled monolayers in organic electronics. *Chem Soc Rev*. 2017;46(1):40-71.

211. Mandler D, Kraus-Ophir S. Self-assembled monolayers (SAMs) for electrochemical sensing. *J Solid State Electrochem*. 2011;15:1535-1558.

212. Allara DL, Nuzzo RG. Spontaneously organized molecular assemblies. 2. Quantitative

infrared spectroscopic determination of equilibrium structures of solution-adsorbed n-alkanoic acids on an oxidized aluminum surface. *Langmuir*. 1985;1(1):52-66.

213. Bain CD, Evall J, Whitesides GM. Formation of monolayers by the coadsorption of thiols on gold: variation in the head group, tail group, and solvent. *J Am Chem Soc*. 1989;111(18):7155-7164.

214. Ulman A. Ultrathin organic films: from Langmuir-Blodgett to self-assembly. *J Mat Ed*. 1989;11:207.

215. Prevo BG, Kuncicky DM, Velev OD. Engineered deposition of coatings from nano-and micro-particles: A brief review of convective assembly at high volume fraction. *Colloids Surfaces A Physicochem Eng Asp*. 2007;311(1-3):2-10.

216. Ranella A, Barberoglou M, Bakogianni S, Fotakis C, Stratakis E. Tuning cell adhesion by controlling the roughness and wettability of 3D micro/nano silicon structures. *Acta Biomater*. 2010;6(7):2711-2720.

217. Kell AJ, Alizadeh A, Yang L, Workentin MS. Monolayer-protected gold nanoparticle coalescence induced by photogenerated radicals. *Langmuir*. 2005;21(21):9741-9746.

218. Fields S. Proteomics in genomeland. *Science (80-)*. 2001;291(5507):1221-1224.

219. MacBeath G. Proteomics comes to the surface. *Nat Biotechnol*. 2001;19(9):828-829.

220. Zhu H, Snyder M. Protein arrays and microarrays. *Curr Opin Chem Biol*. 2001;5(1):40-45.

221. Rusmini F, Zhong Z, Feijen J. Protein immobilization strategies for protein biochips. *Biomacromolecules*. 2007;8(6):1775-1789.

222. Brena B, González-Pombo P, Batista-Viera F. Immobilization of enzymes: a literature survey. *Immobil Enzym Cells Third Ed*. Published online 2013:15-31.

223. Hirsh SL, Bilek MMM, Nosworthy NJ, Kondyurin A, Dos Remedios CG, McKenzie DR. A comparison of covalent immobilization and physical adsorption of a cellulase enzyme mixture. *Langmuir*. 2010;26(17):14380-14388.

224. Kim D, Herr AE. Protein immobilization techniques for microfluidic assays. *Biomicrofluidics*. 2013;7(4):41501.

225. Gibbs J, Kennebunk M. Immobilization principles–Selecting the surface. *ELISA Tech Bull*. 2001;1:1-8.

226. Kamra T, Chaudhary S, Xu C, Montelius L, Schnadt J, Ye L. Covalent immobilization of

molecularly imprinted polymer nanoparticles on a gold surface using carbodiimide coupling for chemical sensing. *J Colloid Interface Sci*. 2016;461:1-8.

227. Blawas AS, Reichert WM. Protein patterning. *Biomaterials*. 1998;19(7-9):595-609.
228. Benešová E, Králová B. Affinity interactions as a tool for protein immobilization. *Affin Chromatogr InTech*. Published online 2012:29-46.
229. Hodneland CD, Lee YS, Min DH, Mrksich M. Selective immobilization of proteins to self-assembled monolayers presenting active site-directed capture ligands. *Proc Natl Acad Sci*. 2002;99(8):5048-5052.
230. Arenkov P, Kukhtin A, Gemmell A, Voloshchuk S, Chupeeva V, Mirzabekov A. Protein microchips: use for immunoassay and enzymatic reactions. *Anal Biochem*. 2000;278(2):123-131.
231. MacBeath G, Schreiber SL. Printing proteins as microarrays for high-throughput function determination. *Science (80-)*. 2000;289(5485):1760-1763.
232. Turkova J. Oriented immobilization of biologically active proteins as a tool for revealing protein interactions and function. *J Chromatogr B Biomed Sci Appl*. 1999;722(1-2):11-31.
233. Saleemuddin M. Bioaffinity based immobilization of enzymes. *Therm Biosensors, Bioactivity, Bioaffinitty*. Published online 1999:203-226.
234. Holt LJ, Enever C, de Wildt RMT, Tomlinson IM. The use of recombinant antibodies in proteomics. *Curr Opin Biotechnol*. 2000;11(5):445-449.
235. Edmondson S, Osborne VL, Huck WTS. Polymer brushes via surface-initiated polymerizations. *Chem Soc Rev*. 2004;33(1):14-22.
236. Barbey R, Lavanant L, Paripovic D, et al. Polymer brushes via surface-initiated controlled radical polymerization: synthesis, characterization, properties, and applications. *Chem Rev*. 2009;109(11):5437-5527.
237. Alexander S. Adsorption of chain molecules with a polar head a scaling description. *J Phys*. 1977;38(8):983-987.
238. de Gennes P. Conformations of polymers attached to an interface. *Macromolecules*. 1980;13(5):1069-1075.
239. Brittain WJ, Minko S. A structural definition of polymer brushes. *J Polym Sci Part A Polym Chem*. 2007;45(16):3505-3512.
240. Hildebrandt M, Shin E young, Yang S, Ali W, Altinpinar S, Gutmann JS. Investigation of

roughness correlation in polymer brushes via X-ray scattering. *Polymers (Basel)*. 2020;12(9):2101.

241. Ayres N. Polymer brushes: Applications in biomaterials and nanotechnology. *Polym Chem*. 2010;1(6):769-777.
242. Zhou X, Liu X, Xie Z, Zheng Z. 3D-patterned polymer brush surfaces. *Nanoscale*. 2011;3(12):4929-4939.
243. Huang H, Ruckenstein E. Steric and bridging interactions between two plates induced by grafted polyelectrolytes. *Langmuir*. 2006;22(7):3174-3179.
244. Zhao B, Brittain WJ. Polymer brushes: surface-immobilized macromolecules. *Prog Polym Sci*. 2000;25(5):677-710.
245. Taniike A, Nakamura R, Kusaka S, Hirooka Y, Nakanishi N, Furuyama Y. Application of the ion beam graft polymerization method to the thin film diagnosis. *Phys Procedia*. 2015;80:151-154.
246. Blacha A, Krukiewicz K, Zak J. The covalent grafting of polymers to the solid surface. *Chemik*. 2011;65(1):11-19.
247. Lee H il, Pietrasik J, Sheiko SS, Matyjaszewski K. Stimuli-responsive molecular brushes. *Prog Polym Sci*. 2010;35(1-2):24-44.
248. Bünsow J, Kelby TS, Huck WTS. Polymer brushes: Routes toward mechanosensitive surfaces. *Acc Chem Res*. 2010;43(3):466-474.
249. Brushes P. by Advincula RC, Brittain WJ, Caster KC, Rühe J. Published online 2004.
250. Sumerlin BS, Lowe AB, Stroud PA, Zhang P, Urban MW, McCormick CL. Modification of gold surfaces with water-soluble (co) polymers prepared via aqueous reversible addition− fragmentation chain transfer (RAFT) polymerization. *Langmuir*. 2003;19(14):5559-5562.
251. Meiron TS, Marmur A, Saguy IS. Contact angle measurement on rough surfaces. *J Colloid Interface Sci*. 2004;274(2):637-644.
252. Coessens V, Pintauer T, Matyjaszewski K. Functional polymers by atom transfer radical polymerization. *Prog Polym Sci*. 2001;26(3):337-377.
253. Wang JS, Matyjaszewski K. Controlled/" living" radical polymerization. atom transfer radical polymerization in the presence of transition-metal complexes. *J Am Chem Soc*. 1995;117(20):5614-5615.

254. Patten TE, Matyjaszewski K. Atom transfer radical polymerization and the synthesis of polymeric materials. *Adv Mater*. 1998;10(12):901-915.

255. SINGH SB. Iridium Chemistry and Its Catalytic Applications: a Brief. *Green Chem Technol Lett*. 2016;2(206):456-518.

256. Boyer C, Corrigan NA, Jung K, et al. Copper-mediated living radical polymerization (atom transfer radical polymerization and copper (0) mediated polymerization): from fundamentals to bioapplications. *Chem Rev*. 2016;116(4):1803-1949.

257. Matyjaszewski K, Xia J. Atom transfer radical polymerization. *Chem Rev*. 2001;101(9):2921-2990.

258. Singh VK, Yu C, Badgujar S, et al. Highly efficient organic photocatalysts discovered via a computer-aided-design strategy for visible-light-driven atom transfer radical polymerization. *Nat Catal*. 2018;1(10):794-804.

259. Xiao D, Wirth MJ. Kinetics of surface-initiated atom transfer radical polymerization of acrylamide on silica. *Macromolecules*. 2002;35(8):2919-2925.

260. Lorandi F, Matyjaszewski K. Why do we need more active ATRP catalysts? *Isr J Chem*. 2020;60(1-2):108-123.

261. Frazer L. Radical departure: polymerization does more with less. Published online 2007.

262. Matyjaszewski K. ll Сит. 0pin. *Solid State Mater Sci*. 1996;1(6):769.

263. Braunecker WA, Matyjaszewski K. Recent mechanistic developments in atom transfer radical polymerization. *J Mol Catal A Chem*. 2006;254(1-2):155-164.

264. Matyjaszewski K, Miller PJ, Shukla N, et al. Polymers at interfaces: using atom transfer radical polymerization in the controlled growth of homopolymers and block copolymers from silicon surfaces in the absence of untethered sacrificial initiator. *Macromolecules*. 1999;32(26):8716-8724.

265. Edmondson S, Nguyen NT, Lewis AL, Armes SP. Co-nonsolvency effects for surface-initiated poly (2-(methacryloyloxy) ethyl phosphorylcholine) brushes in alcohol/water mixtures. *Langmuir*. 2010;26(10):7216-7226.

266. Li J, Chen H, Mu G, et al. Synthesis of amphiphilic block copolymers via ARGET ATRP using an inexpensive ligand of PMDETA. *React Funct Polym*. 2013;73(11):1517-1522.

267. Abbott NL, Kumar A, Whitesides GM. Using micromachining, molecular self-assembly, and wet etching to fabricate 0.1-1-. mu. m-scale structures of gold and silicon. *Chem*

Mater. 1994;6(5):596-602.

268. Zhang L, Miao J, Cheng Z, Zhu X. Iron-Mediated ICAR ATRP of Styrene and Methyl Methacrylate in the Absence of Thermal Radical Initiator. *Macromol Rapid Commun*. 2010;31(3):275-280.

269. Ramirez R, Woodcock J, Kilbey SM. ARGET-ATRP synthesis and swelling response of compositionally varied poly (methacrylic acid-co-N, N-diethylaminoethyl methacrylate) polyampholyte brushes. *Soft Matter*. 2018;14(30):6290-6302.

270. Matyjaszewski K, Jakubowski W, Min K, et al. Diminishing catalyst concentration in atom transfer radical polymerization with reducing agents. *Proc Natl Acad Sci*. 2006;103(42):15309-15314.

271. Alswieleh A. Micro-and Nano-Structure of Polymers and Molecular Materials. Published online 2014.

272. Bhat RR, Tomlinson MR, Wu T, Genzer J. Surface-grafted polymer gradients: Formation, characterization, and applications. *Surface-initiated Polym ii*. Published online 2006:51-124.

273. Calvo A, Yameen B, Williams FJ, Soler-Illia GJAA, Azzaroni O. Mesoporous films and polymer brushes helping each other to modulate ionic transport in nanoconfined environments. An interesting example of synergism in functional hybrid assemblies. *J Am Chem Soc*. 2009;131(31):10866-10868.

274. Dai S, Ravi P, Tam KC. pH-Responsive polymers: synthesis, properties and applications. *Soft Matter*. 2008;4(3):435-449.

275. Klinghammer S, Rauch S, Pregl S, Uhlmann P, Baraban L, Cuniberti G. Surface modification of silicon nanowire based field effect transistors with stimuli responsive polymer brushes for biosensing applications. *Micromachines*. 2020;11(3):274.

276. Mitsuishi M, Ishifuji M, Endo H, Tanaka H, Miyashita T. Hybrid polymer nanoassemblies: Polymer nanosheets organized with metal nanoparticle arrays for surface plasmon photonics. *Polym J*. 2007;39(5):411-422.

277. Savas TA, Farhoud M, Smith HI, Hwang M, Ross CA. Properties of large-area nanomagnet arrays with 100 nm period made by interferometric lithography. *J Appl Phys*. 1999;85(8):6160-6162.

278. Savas TA, Schattenburg ML, Carter JM, Smith HI. Large-area achromatic interferometric

lithography for 100 nm period gratings and grids. *J Vac Sci Technol B Microelectron Nanom Struct Process Meas Phenom*. 1996;14(6):4167-4170.

279. Zheng D. *Medical Applications of a Tunable Monochromatic X-Ray Source in Cancer Detection, Diagnosis and Therapy*. University of California, Davis; 2007.

280. Decker EL, Frank B, Suo Y, Garoff S. Physics of contact angle measurement. *Colloids Surfaces A Physicochem Eng Asp*. 1999;156(1-3):177-189.

281. Kwok DY, Neumann AW. Contact angle measurement and contact angle interpretation. *Adv Colloid Interface Sci*. 1999;81(3):167-249.

282. Hoque E, DeRose JA, Kulik G, Hoffmann P, Mathieu HJ, Bhushan B. Alkylphosphonate modified aluminum oxide surfaces. *J Phys Chem B*. 2006;110(22):10855-10861.

283. Fukushima H, Seki S, Nishikawa T, et al. Microstructure, wettability, and thermal stability of semifluorinated self-assembled monolayers (SAMs) on gold. *J Phys Chem B*. 2000;104(31):7417-7423.

284. Ostrovskaya L, Podesta A, Milani P, Ralchenko V. Influence of surface morphology on the wettability of cluster-assembled carbon films. *Europhys Lett*. 2003;63(3):401.

285. Kaholek M, Lee WK, Ahn SJ, et al. Stimulus-responsive poly (N-isopropylacrylamide) brushes and nanopatterns prepared by surface-initiated polymerization. *Chem Mater*. 2004;16(19):3688-3696.

286. Lee W, Sheehan PE. Scanning probe lithography of polymers: tailoring morphology and functionality at the nanometer scale. *Scanning J Scanning Microsc*. 2008;30(2):172-183.

287. Brower TL, Garno JC, Ulman A, et al. Self-Assembled Multilayers of 4, 4 ‘-Dimercaptobiphenyl Formed by Cu (II)-Catalyzed Oxidation. *Langmuir*. 2002;18(16):6207-6216.

288. Bazzan G, Smith W, Francesconi LC, Drain CM. Electrostatic self-organization of robust porphyrin− polyoxometalate films. *Langmuir*. 2008;24(7):3244-3249.

289. McLean RS, Sauer BB. Tapping-mode AFM studies using phase detection for resolution of nanophases in segmented polyurethanes and other block copolymers. *Macromolecules*. 1997;30(26):8314-8317.

290. Camesano TA, Natan MJ, Logan BE. Observation of changes in bacterial cell morphology using tapping mode atomic force microscopy. *Langmuir*. 2000;16(10):4563-4572.

291. Moore Jr L, LeJeune ZM, Luces CA, et al. Lysine-based zwitterionic molecular micelle

for simultaneous separation of acidic and basic proteins using open tubular capillary electrochromatography. *Anal Chem*. 2010;82(10):3997-4005.

292. Vedam K. Spectroscopic ellipsometry: a historical overview. *Thin Solid Films*. 1998;313:1-9.

293. Tompkins H, Irene EA. *Handbook of Ellipsometry*. William Andrew; 2005.

294. Synowicki RA. Spectroscopic ellipsometry characterization of indium tin oxide film microstructure and optical constants. *Thin Solid Films*. 1998;313:394-397.

295. Tsargorodska A, Cartron ML, Vasilev C, et al. Strong coupling of localized surface plasmons to excitons in light-harvesting complexes. *Nano Lett*. 2016;16(11):6850-6856.

296. Alswieleh AM, Cheng N, Canton I, et al. Zwitterionic Poly (amino acid methacrylate) Brushes. *J Am Chem Soc*. 2014;136(26):9404-9413.

297. Islam K, Alnuaimi A, Battal E, Okyay AK, Nayfeh A. Effect of gold nanoparticles size on light scattering for thin film amorphous-silicon solar cells. *Sol Energy*. 2014;103:263-268.

298. Sun S, Chong KSL, Leggett GJ. Nanoscale molecular patterns fabricated by using scanning near-field optical lithography. *J Am Chem Soc*. 2002;124(11):2414-2415.

299. Lee JH, Kang SJ, Lee PC, Han TH, Nam JD, Lee YK. Negative-type photolithography of functionalized gold nanoparticles. *Macromol Res*. 2009;17(2):137-139.

300. Ducker RE, Leggett GJ. A mild etch for the fabrication of three-dimensional nanostructures in gold. *J Am Chem Soc*. 2006;128(2):392-393.

301. Hutt DA, Leggett GJ. Influence of adsorbate ordering on rates of UV photooxidation of self-assembled monolayers. *J Phys Chem*. 1996;100(16):6657-6662.

302. Vazquez-Mena O, Sannomiya T, Villanueva LG, Voros J, Brugger J. Metallic nanodot arrays by stencil lithography for plasmonic biosensing applications. *ACS Nano*. 2011;5(2):844-853.

303. Tuersun P, Yusufu T, Yimiti A, Sidike A. Refractive index sensitivity analysis of gold nanoparticles. *Optik (Stuttg)*. 2017;149:384-390.

304. Lo KKW, Lau JSY. Design of transition metal biotin complexes as non-covalent probes for avidin. *Coord Chem Res Prog*. Published online 2008:175-200.

305. Välimaa L. Streptavidin-a versatile binding protein for solid-phase immunoassays. Published online 2008.

306. Williams EH, Davydov A V, Motayed A, et al. Immobilization of streptavidin on 4H–SiC

for biosensor development. *Appl Surf Sci*. 2012;258(16):6056-6063.

307. Tsargorodska A, Cartron ML, Vasilev C, et al. Strong Coupling of Localized Surface Plasmons to Excitons in Light-Harvesting Complexes. *Nano Lett*. 2016;16(11):6850-6856. doi:10.1021/acs.nanolett.6b02661
308. Avvakumova S, Colombo M, Galbiati E, Mazzucchelli S, Rotem R, Prosperi D. Bioengineered approaches for site orientation of peptide-based ligands of nanomaterials. In: *Biomedical Applications of Functionalized Nanomaterials*. Elsevier; 2018:139-169.
309. Lishchuk A, Kodali G, Mancini JA, et al. A synthetic biological quantum optical system. *Nanoscale*. 2018;10(27):13064-13073.
310. Kodali G, Mancini JA, Solomon LA, et al. Design and engineering of water-soluble light-harvesting protein maquettes. *Chem Sci*. 2017;8(1):316-324.
311. Ennist NM, Stayrook SE, Dutton PL, Moser CC. Rational design of photosynthetic reaction center protein maquettes. *Front Mol Biosci*. 2022;9:997295.
312. Ennist NM, Zhao Z, Stayrook SE, Discher BM, Dutton PL, Moser CC. De novo protein design of photochemical reaction centers. *Nat Commun*. 2022;13(1):4937.
313. Lichtenstein BR, Farid TA, Kodali G, et al. Engineering oxidoreductases: Maquette proteins designed from scratch. *Biochem Soc Trans*. 2012;40(3):561-566. doi:10.1042/BST20120067
314. Xia S, Cartron M, Morby J, Bryant DA, Hunter CN, Leggett GJ. Fabrication of nanometer-and micrometer-scale protein structures by site-specific immobilization of histidine-tagged proteins to aminosiloxane films with photoremovable protein-resistant protecting groups. *Langmuir*. 2016;32(7):1818-1827.
315. Agranovich VM, Litinskaia M, Lidzey DG. Cavity polaritons in microcavities containing disordered organic semiconductors. *Phys Rev B*. 2003;67(8):85311.
316. Shi L, Hakala TK, Rekola HT, Martikainen JP, Moerland RJ, Törmä P. Spatial coherence properties of organic molecules coupled to plasmonic surface lattice resonances in the weak and strong coupling regimes. *Phys Rev Lett*. 2014;112(15):153002.
317. Cory MG, Zerner MC, Hu X, Schulten K. Electronic excitations in aggregates of bacteriochlorophylls. *J Phys Chem B*. 1998;102(39):7640-7650.
318. Cogdell RJ, Isaacs NW, Freer AA, et al. The structural basis of light-harvesting in purple bacteria. *FEBS Lett*. 2003;555(1):35-39.

319. Rosen JE, Gu FX. Surface functionalization of silica nanoparticles with cysteine: a low-fouling zwitterionic surface. *Langmuir*. 2011;27(17):10507-10513.

320. Jiang L, Messing ME, Ye L. Temperature and pH dual-responsive core-brush nanocomposite for enrichment of glycoproteins. *ACS Appl Mater Interfaces*. 2017;9(10):8985-8995.

321. Sezer AD. *Application of Nanotechnology in Drug Delivery*. BoD–Books on Demand; 2014.

322. Pérez-Herrero E, Fernández-Medarde A. The reversed intra-and extracellular pH in tumors as a unified strategy to chemotherapeutic delivery using targeted nanocarriers. *Acta Pharm Sin B*. 2021;11(8):2243-2264.

323. Erwin WR, Zarick HF, Talbert EM, Bardhan R. Light trapping in mesoporous solar cells with plasmonic nanostructures. *Energy Environ Sci*. 2016;9(5):1577-1601.

324. Brennan LJ, Purcell-Milton F, Salmeron AS, et al. Hot plasmonic electrons for generation of enhanced photocurrent in gold-TiO2 nanocomposites. *Nanoscale Res Lett*. 2015;10(1):1-12.

325. Topham PD, Howse JR, Crook CJ, et al. Controlled growth of poly (2-(diethylamino) ethyl methacrylate) brushes via atom transfer radical polymerisation on planar silicon surfaces. *Polym Int*. 2006;55(7):808-815.

326. Fielding LA, Edmondson S, Armes SP. Synthesis of pH-responsive tertiary amine methacrylate polymer brushes and their response to acidic vapour. *J Mater Chem*. 2011;21(32):11773-11780.

327. Edmondson S, Vo CD, Armes SP, Unali GF. Surface polymerization from planar surfaces by atom transfer radical polymerization using polyelectrolytic macroinitiators. *Macromolecules*. 2007;40(15):5271-5278.

328. Zhang Z, Chao T, Chen S, Jiang S. Superlow fouling sulfobetaine and carboxybetaine polymers on glass slides. *Langmuir*. 2006;22(24):10072-10077.

329. Azzaroni O, Moya SE, Brown AA, Zheng Z, Donath E, Huck WTS. Polyelectrolyte brushes as ink nanoreservoirs for microcontact printing of ionic species with poly (dimethyl siloxane) stamps. *Adv Funct Mater*. 2006;16(8):1037-1042.

330. Feng W, Zhu S, Ishihara K, Brash JL. Adsorption of fibrinogen and lysozyme on silicon grafted with poly (2-methacryloyloxyethyl phosphorylcholine) via surface-initiated atom

transfer radical polymerization. *Langmuir*. 2005;21(13):5980-5987.

331. Lishchuk A, Csányi E, Darroch B, Wilson C, Nabok A, Leggett GJ. Active control of strong plasmon–exciton coupling in biomimetic pigment–polymer antenna complexes grown by surface-initiated polymerisation from gold nanostructures. *Chem Sci*. 2022;13(8):2405-2417.
332. Yu Q, Ista LK, Gu R, Zauscher S, López GP. Nanopatterned polymer brushes: conformation, fabrication and applications. *Nanoscale*. 2016;8(2):680-700.
333. Al-Jaf O, Alswieleh A, Armes SP, Leggett GJ. Nanotribological properties of nanostructured poly (cysteine methacrylate) brushes. *Soft Matter*. 2017;13(10):2075-2084.
334. Seuring J, Agarwal S. Polymers with upper critical solution temperature in aqueous solution: Unexpected properties from known building blocks. Published online 2013.
335. Zhang Q, Hoogenboom R. Polymers with upper critical solution temperature behavior in alcohol/water solvent mixtures. *Prog Polym Sci*. 2015;48:122-142.
336. Bashkatov AN, Genina EA. Water refractive index in dependence on temperature and wavelength: a simple approximation. In: *Saratov Fall Meeting 2002: Optical Technologies in Biophysics and Medicine IV*. Vol 5068. SPIE; 2003:393-395.
337. Wientjes E, Renger J, Curto AG, Cogdell R, Van Hulst NF. Strong antenna-enhanced fluorescence of a single light-harvesting complex shows photon antibunching. *Nat Commun*. 2014;5(1):4236.